INFLUENCE OF FREQUENCY AND ENVIRONMENT ON THE FATIGUE BEHAVIOR OF MONOCRYSTALLINE SILICON THIN FILMS

A Thesis
Presented to
The Academic Faculty

by

Pierre-Olivier Theillet

In Partial Fulfillment
of the Requirements for the Degree
Master of Science in the
George W. Woodruff School of Mechanical Engineering

Georgia Institute of Technology
May 2009

INFLUENCE OF FREQUENCY AND ENVIRONMENT ON THE FATIGUE BEHAVIOR OF MONOCRYSTALLINE SILICON THIN FILMS

Approved by:

Dr. Olivier N. Pierron, Advisor
George W. Woodruff School of Mechanical Engineering
Georgia Institute of Technology

Dr. Ting Zhu
George W. Woodruff School of Mechanical Engineering
Georgia Institute of Technology

Dr. Richard W. Neu
George W. Woodruff School of Mechanical Engineering
Georgia Institute of Technology

Date Approved: March 23rd 2009

ACKNOWLEDGEMENTS

I wish to express my gratitude to my academic advisor Olivier Pierron for his outstanding availability, continuous support and encouragement as well as for the precious discussions and guidance that led to this work.

I would like to thank the École Centrale de Lyon, the Région Rhône-Alpes, the George W. Woodruff School of Mechanical Engineering, and the College of Engineering at Georgia Institute of Technology for providing the financial and material assistance as well as a scientific formation of great quality.

I will finally thank my family and friends, especially Mélanie Raine, Michael Budnitzki and my parents for their own way of supporting me without fail.

TABLE OF CONTENTS

LIST OF TABLES

LIST OF FIGURES

SUMMARY

Understanding the mechanisms for fatigue crack initiation and propagation in micron-scale silicon (Si) is of great importance to assess and improve the reliability of Si-based microelectromechanical systems (MEMS) in harsh environments. Accordingly, this investigation studies the fatigue properties of 10-micron-thick single-crystal Si (SCSi) films using kHz-frequency resonating structures under fully-reversed loading. Overall, the stress plays a major role on the fatigue properties: decreasing the stress amplitude from ~3-3.5 GPa to ~1.5-2 GPa results in an increase in lifetime from 10^2 to 10^{10} cycles, and a decrease in degradation rate by 4-5 orders of magnitude. In addition to stress, the influences of resonant frequency (4 vs. 40 kHz) and environment (30°C, 50%RH vs. 80°C, 30%RH and 80°C, 90%RH) on the resulting S-N curves and resonant frequency evolution are thoroughly investigated.

In the high- to very high-cycle fatigue (HCF/VHCF) regime, both the frequency and environment strongly affect the fatigue properties. Damage accumulation rates are significantly higher in harsh environments. In 80°C, 90%RH the rates exceed by one to two orders of magnitude the values at 30°C, 50%RH for similar stress amplitudes. The separate influence of humidity, affecting the adsorbed water layer thickness, is also highlighted at 80°C: the decrease rates are measured up to one order of magnitude lower at 30%RH than at 90%RH. Moreover, a strong influence of frequency is detected. These observations bring further evidence supporting reaction-layer fatigue as a viable description of the HCF/VHCF behavior of micron-scale Si.

Regarding the low-cycle fatigue (LCF) properties, continuous, monotonic damage accumulation, beginning after the first burst (as low as ~500 cycles), is observed. The decrease rates in resonant frequency are not as much influenced by the environment as in the HCF/VHCF regime, although they are higher in harsh environments. Scanning electron microscopy of the fracture surface reveals smooth, semi-elliptical mirror-like regions, suggesting highly localized fatigue damage accumulation. An investigation on time-dependent subcritical cracking for the LCF regime is implemented, but does not appear to fully account for the experimental results. The details of the underlying mechanism for the LCF behavior of SCSi films remain unclear.

CHAPTER 1

INTRODUCTION

1.1. *Reliability of Micro Electro Mechanical Systems (MEMS) in Harsh Environments*

1.1.1. MEMS Technology for Harsh Environment Applications

Most microelectromechanical systems (MEMS), also known as micromachines, integrate micron-scale mechanical elements with electronics on a silicon (thereafter Si) substrate. A number of MEMS fabrication techniques have emerged since the 1980s, largely compatible with standard integrated circuit (IC) manufacturing techniques. The main advantages of MEMS technology are as follows [1]. First, MEMS technology allows functions that are not possible otherwise (for instance the all-optical switching technique). Using IC standard manufacturing techniques also gives the opportunity of benefiting from batch fabrication, the basis for large-scale commercialization. Moreover, integrating mechanical and electrical devices on a single chip reduces the number of interconnections, therefore increasing the reliability of complex components.

For all these reasons, MEMS technology has been developed and has had numerous successes in domains such as automotive and consumer products. Accelerometers and gyroscopes are largely used for airbag, vehicle stability systems and electronic suspensions. Active stabilization of cameras, head-mounted displays, ink-jet print head, microphones and new display systems such as Texas Instruments' Digital Micromirror Device are appreciated for their low cost, high quality and speed properties. Telecommunication and radio-frequency systems can benefit from MEMS tuning and switching components like variable capacitors and inductors, RF and mirror switches or optical routers (see for instance www.sitime.com for MEMS-based timing solutions).

In addition to these well established applications, MEMS technology has the potential to enable new applications in "harsh" environments, in the domains of defense, energy, aerospace as well as biomedical and medical care. As described by Stauffer [2], "harsh environment" is as an acronym including all applications that behave under extreme conditions in terms of temperature, shock, vibration, pressure, magnetic field, radiation or chemistry. For instance impact and void detection or safing and arming missiles need high-sensitivity accelerometers, magnetic and pressure sensors capable of withstanding shock levels up to 20,000g in a wide range of temperatures (typically -120°C to 180°C) [2, 3]. Such accelerometers and gyroscopes are also used for guidance systems, seismometry for oil exploration and earthquake prediction, down-hole drilling and platform stabilization on space. In addition, for numerous applications, MEMS devices must be exposed to, and interact with the environment; examples include microfluidic devices such as biomedical devices, chemical sensors, pumps and fuel cells. Furthermore an increasing role in biomedical engineering is predicted for drug microdelivery systems and diagnostic equipment miniaturization using chemical sensors and microfluidic pumps [4]. In these applications, harsh environments are likely to affect the system reliability and their influence must be thoroughly investigated for successful integration in the field.

In order to design reliable MEMS devices in harsh environments, the mechanical properties of the structural materials in relevant environments must be well characterized [1, 5, 6]. Particularly, the fatigue degradation properties in harsh environments must be known, for applications such as liquid-phase microresonator (very high-cycle fatigue (VHCF)), and inertial measurement units (IMUs) under shocks (low-cycle fatigue (LCF) [7]).

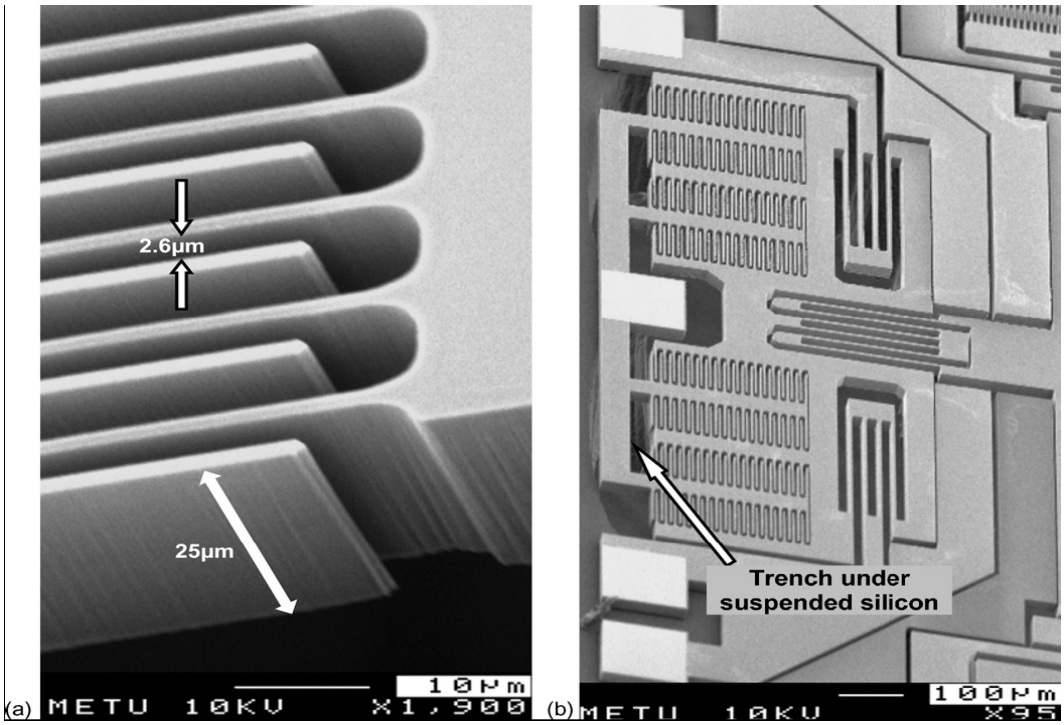

Figure 1: SEM pictures of high-performance gyroscope, showing (a) 25 µm-thick comb fingers with 2.6 µm capacitive gap, and (b) suspended sense-electrode of the fabricated gyroscope. (S.Alper *et al*. [8]).

1.1.2. Monocrystalline Silicon Thin Films as Structural Material

Surface micromachined MEMS are fabricated based on standard lithographic processes creating mechanical elements on the surface of Si wafers by sequentially depositing, photopatterning and etching thin films. To date, most commercially available MEMS products use polycrystalline Si (Polysilicon) as structural material. Nonetheless, monocrystalline or single-crystal Si (SCSi) is also widely used as high quality electronic material, through bulk micromachining. This fabrication process creates elements by etching down a Si wafer, notably to build pressure sensors (first sales volume among MEMS) [9]. An example of bulk micromachined devices is presented in

Figure 1 illustrating the use of high-aspect-ratio silicon-on-insulator (SOI) micromachining process. This particular device generates high mechanical quality factors to create high-performance gyroscope in atmospheric pressure.

Depending on the application, the structural material in use for MEMS devices can be subjected to various sorts of loading (bending, tension, torque or shear, and cyclic, transient or monotonic), different environment (mild or harsh, see 1.1.1) and a wide range of time scale. As a consequence reliability and performance of these devices greatly depend on the mechanical properties of the structural material. Micron-scale SCSi presents interesting mechanical properties for MEMS applications. It exhibits high mechanical strength [5, 10-12] and Young's Modulus [5, 13, 14], and can withstand extreme environmental conditions such as temperatures between -120°C and +180°C [2]. However, it is very brittle due to the absence of toughening mechanisms (measured fracture toughness values are around 1 $MPa.m^{1/2}$ [12, 15-19]).

Bulk Si has long been considered to be immune to fatigue failure [20]. Experimental and computational studies have showed that Si does not undergo stress corrosion cracking in air or water [21, 22]. In addition Si does not exhibit any extrinsic toughening mechanism that could degrade during cyclic loading and lead to fatigue failure [20]. Nevertheless, fatigue for bulk Si under cyclic Hertzian contact loading with hard spheres has recently been observed [23-25]. Zarudi *et al.* [26, 27] reported a mechanism involving a phase transformation under large hydrostatic stresses, which is unlikely to occur under bending mode for micron-scale Si. Moreover, the surface-to-volume ratio of the structural Si in micron-scale applications is very large and contributions from the surfaces become significant. Consequently, the fatigue mechanism at the bulk scale cannot be applied to describe accurately the observed fatigue behavior of Si thin films under various deformation modes [10, 15, 16, 22, 28-36], which is summarized in the next section.

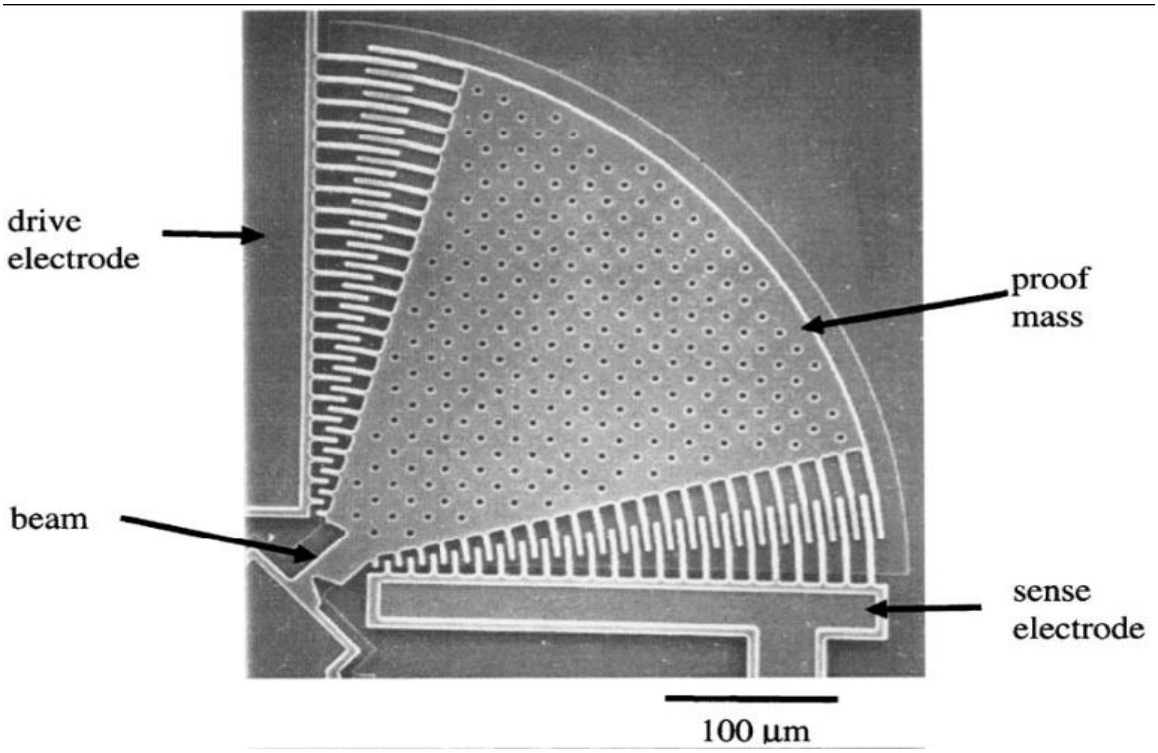

Figure 2: MEMS fatigue specimen designed by Van Arsdell and Brown to study the fatigue behavior of polysilicon films. It features a large proof mass, the tested beam as well as on-chip actuation and sensing comb-drives [37].

1.2. *Literature Review on Fatigue of Monocrystalline Silicon Thin Films*

1.2.1. Fatigue Testing Structures

Since there is no standard for fatigue testing of thin films, investigators have used several testing methods for characterization of the fatigue properties of Si thin films [6, 28, 29, 38-40]. This section summarizes the various actuation and sensing techniques employed to accurately measure these properties.

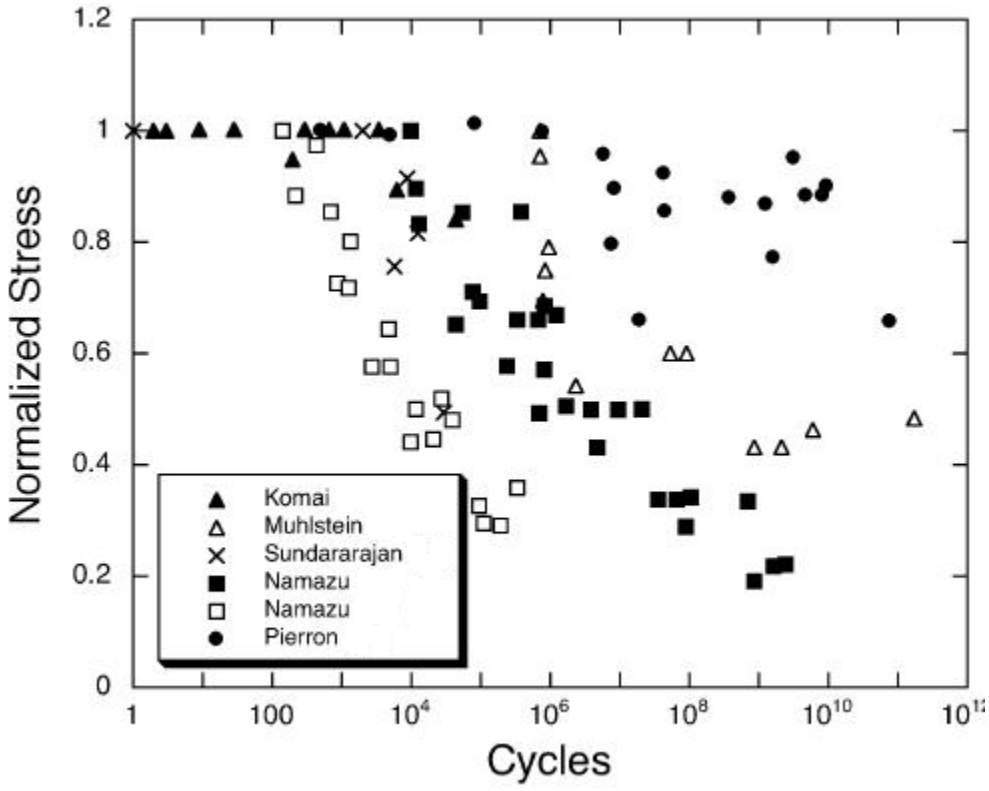

Figure 3: Normalized applied maximum stress vs. number of cycles to failure (*S*-*N*) curve for the cyclic fatigue of single-crystal silicon in ambient air taken from the available literature. For each reference, the stress values are normalized with respect to the maximum applied stress (Alsem *et al.* [28], [30, 32-34, 41, 42]).

First, actuation can be external. In that case, a nanoindenter can be used to apply a controlled mode of displacement to cantilever beams [10, 32, 36, 40, 43, 44], clamped-clamped beams [30, 42] or simple surfaces [23, 24]. Piezoelectric actuators, voice coil and loud speaker [45, 46] can also generate external actuation. The sensing can also be external. In that case, displacements can be measured with optical deflection systems, strain gauges or AFM [33, 36, 41, 42, 45, 46]. However, alignments between the specimen and the actuator as well as actuation calibrations are necessary.

Internal actuation and sensing is therefore a preferred technique to avoid the aforementioned issues. Such devices achieving integrated actuation and sensing are known as on-chip testing devices. Electrostatic forces are often used to actuate cantilevers or membranes [47, 48]. The most widely used testing system employs electrostatically driven resonant structures that are actuated by application of an AC voltage across interdigitated combs [31, 34, 49-51]. The same comb-drive technique can also be used for sensing purpose. Such autonomous testing device, capable of applying loads and sensing displacements, can be fabricated with standard MEMS processes such as bulk or surface micromachining. Van Arsdell and Brown [37] reported the fatigue behavior of Si thin films using the on-chip structures presented in Figure 2. These electrostatically driven structures present a notched cantilever beam tested in cyclic bending. The resonant frequency is continuously monitored to characterize the fatigue damage. Very high lifetime can possibly be reached in a fairly short amount of time. Nevertheless, the loading ratio, R, defined as the ratio minimal over maximal applied stress, is limited to -1.

Thermal actuation is another high-force, on-chip actuation method, providing advantages over electrostatic actuation, such as a notable increase in displacement range [52, 53]. By application of a bias over two anchor sites, displacement is generated due to thermal strains obtained by Joule effect in the system. Whereas the comb drive actuator is force-controlled, the thermal actuator is displacement-controlled and can deliver a large force and a moderate displacement. The main drawbacks of this method are complex calibration, high inertia and therefore limitations in testing frequency.

1.2.2. Fatigue Data

Alsem [28] and Kahn [29] extensively reviewed the literature on fatigue testing of SCSi thin films. This section summarizes the large body of experimental work that investigated this fatigue phenomenon, starting in the early 1990s, with particular focus on the *S-N* curves, the influence of environment, and the influence of frequency.

Connally and Brown [49] first observed delayed failure for micron-scale SCSi and polysilicon thin films in bending and tension/compression loading. The stress-life *(S-N)* data gathered by Muhlstein [32], Sundurarajan [42], Pierron [34] and Namazu [41] (see Figure 3) as well as in observations of Ando *et al.* [46], clearly show that lower cyclic stresses result in larger fatigue lives. Besides, Namazu *et al.* [41, 54] reported strong effects of the specimen size and the deformation mode. Micro-scale specimens showed lower fatigue lives than the nano-scale ones for similar stress levels. This seems to be related to the increased number of defects with increasing the length scale. They also observed that the tensile mode was significantly decreasing fatigue lives. Fatigue was observed for stresses as low as 10% of the averaged fracture stress, which is significantly lower than other investigations.

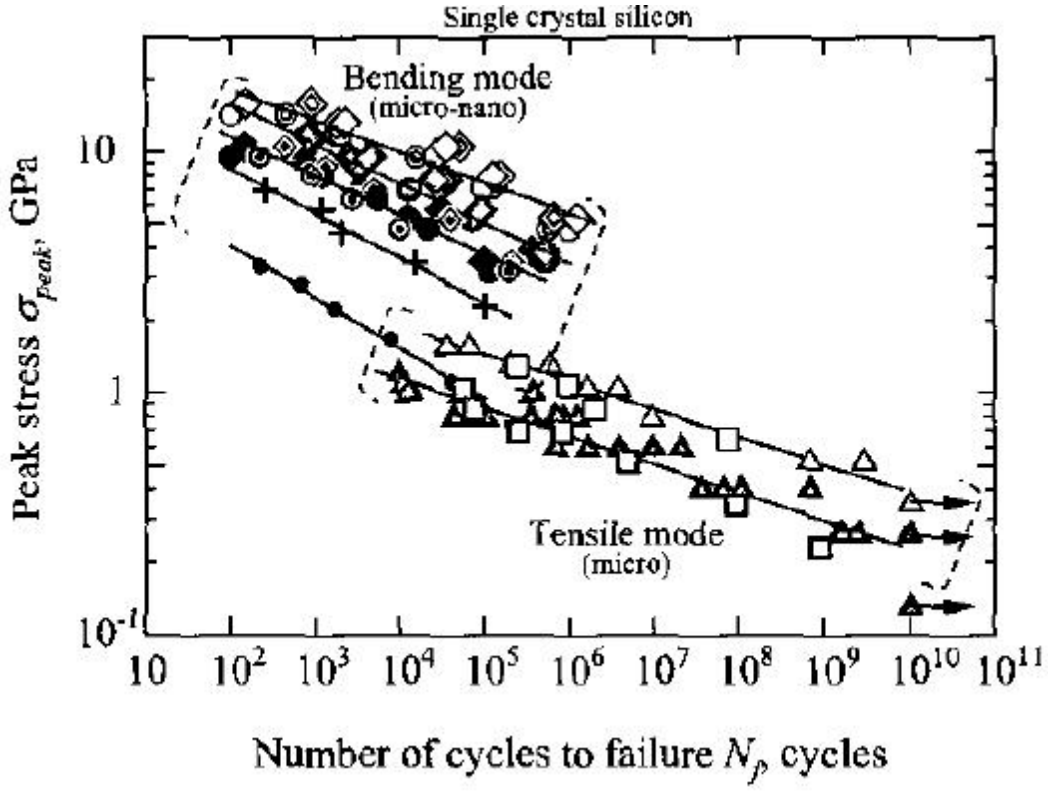

Figure 4: Bending/Tensile fatigue lives correlated with peak stress. Diamond- and square shape indicators stand for tests at 295K, while round- and triangle-shape indicators stand for tests at 573K. Dot and cross were 10-Hz micron-scale tests. Fully empty and full diamond- and square shape indicators were 50-Hz micron-scale tests. The others were 50-Hz micron-scale tests (Namazu *et al.* [41])

Connally and Brown [49] as well as Li and Bhushan [55] found a decrease in stiffness with cycling in wet air, accompanied with decreasing rates of change. Tsuchiya *et al.* [45] and Muhlstein *et al.* [32] also observed the following: the lower the cyclic stress, the longer the fatigue life and the larger the total decrease in resonant frequency (for resonant specimens) and therefore the larger the damage accumulation.

A number of studies investigated the environmental effects on the fatigue properties. Particularly the increase in relative humidity accelerates the cyclic damage accumulation (Minoshima [10], Connally and Brown [49], Koskenvuori [31], Pierron

[34]) whereas no fatigue effect has been reported in high vacuum by Koskenvuori [31] and Pierron [34] (medium vacuum environments cause fatigue behavior intermediate between high vacuum and air). Tsuchiya *et al.* [45] observed also a detrimental influence of humidity on the fracture strength of SCSi thin films. In contrast, Namazu *et al.* [41] did not notice any relative influence of the temperature (see Figure 4).

A few studies [33, 41, 54] investigated the influence of frequency. The studies did not notice any relative influence of the driving frequency on the fatigue lives (10 - 450 Hz, bending and tension/compression). Muhlstein *et al.* [32] did not observe either any frequency effect on the fatigue life between 40 and 50 kHz .

It is worthwhile to mention the results of a recent study by Kenny, Dauskardt and coworkers [15, 22]. They used static crack growth tests to develop crack velocity vs. applied stress intensity factor (K_I) curves that can be fitted with the following equation:

$$\frac{da}{dt} = A.K^n \tag{1}$$

The results suggest that subcritical cracking occurs for $0.9\ K_{Ic} < K_I < 0.98\ K_{Ic}$, with a crack-growth rate exponent, n, higher than 100. Based on this evidence, they concluded that stress corrosion cracking in SCSi does not occur.

It is also important to underline that, under the light of similar evidences gathered by Muhlstein [32, 56] and Bagdahn [57] for both SCSi and polysilicon, it is likely that the origin of fatigue in these materials is similar. The following experimental evidence on fatigue of polysilicon films is therefore added to the previous summary:

- thick oxides and increased surface roughness in the highly stressed region were observed after cycling [56, 58-62],
- no fatigue under monotonic loading was observed [50].

1.2.3. Fatigue Mechanisms for Silicon Thin Films

Three predominant mechanisms are proposed in the literature to explain the aforementioned fatigue phenomenon: stress-assisted surface oxide dissolution (Allameh *et al.* [60, 61]), mechanically induced subcritical cracking (Kahn *et al.* [50]), and reaction-layer fatigue (Muhlstein *et al.* [56]).

Based on the observation of Komai, Minoshima *et al.* [10] and Allameh *et al.* [60, 61], the stress-assisted dissolution of surface silica involves cyclic stress enhanced oxidation, followed by dissolution of the surface oxide. This phenomenon leads to evolution of perturbations and deepening of grooves with a rate proportional to the state of local stresses. These flaws are the preferable sites for crack nucleation. Kahn *et al.* pointed out three issues with this mechanism [29]:

- such mechanism has never been observed for any kind of material,
- the model is based on a stress-dependent surface reaction model applied only to monotonic stresses,
- finally the time dependence of such mechanism is opposed to experimental observations.

The mechanically induced subcritical cracking model assumes that subcritical cracking occurs in Si itself. Kahn *et al.* [50] proposed a wedging effect due to debris or oxidized surfaces inside the crack that create additional cracking under compression loading ("cantilever effect"). This model explains well the dependence on stress levels, loading ratio and cyclic loading. The observed influence of environment is accounted as follows: in air, surface oxide formation at the crack tip can enhance the cantilever effect under compression loading [29]. However, this phenomenon does not explain either the

surface roughness increase [60] or the increased thickness of surface oxide in highly stressed zones [56, 59, 62, 63]. Furthermore Pierron *et al.* [64] showed that the maximal driving force for crack advance is reached during the tensile part of the cycle even for wedged cracks. In addition, fatigue of Si thin films is observed under tension-tension loading conditions ($R > 0$) [22, 65]. Thus, mechanically-induced subcritical cracking appears unlikely to account for the observed fatigue behavior for Si thin films.

On the other hand the reaction-layer fatigue mechanism attributes fatigue to a surface effect caused by subcritical cracking in the silicon-oxide layer therefore referred to as reaction-layer. The mechanism postulates cyclic-stress-assisted oxidation at the Si surface, followed by initiation and growth of cracks within the layer via environmentally- and cyclically-assisted cracking processes (see Figure 5). This mechanism explains the apparent size effect associated with the fatigue behavior of Si under tension-compression and bending loading, which is related to the comparison between the critical crack size and the oxide thickness. Only at the micron scale and lower are the two quantities commensurate. It is consistent with most of existing experimental results [28, 66]. Particularly, subcritical cracks in thickened surface oxide layers have been observed [56]. Also, the reaction-layer mechanism accounts for the absence of fatigue for Si thin films in high vacuum, the influence of humidity and stress. It is also consistent with fatigue under tensile-tensile loading, unlike the mechanically induced fatigue.

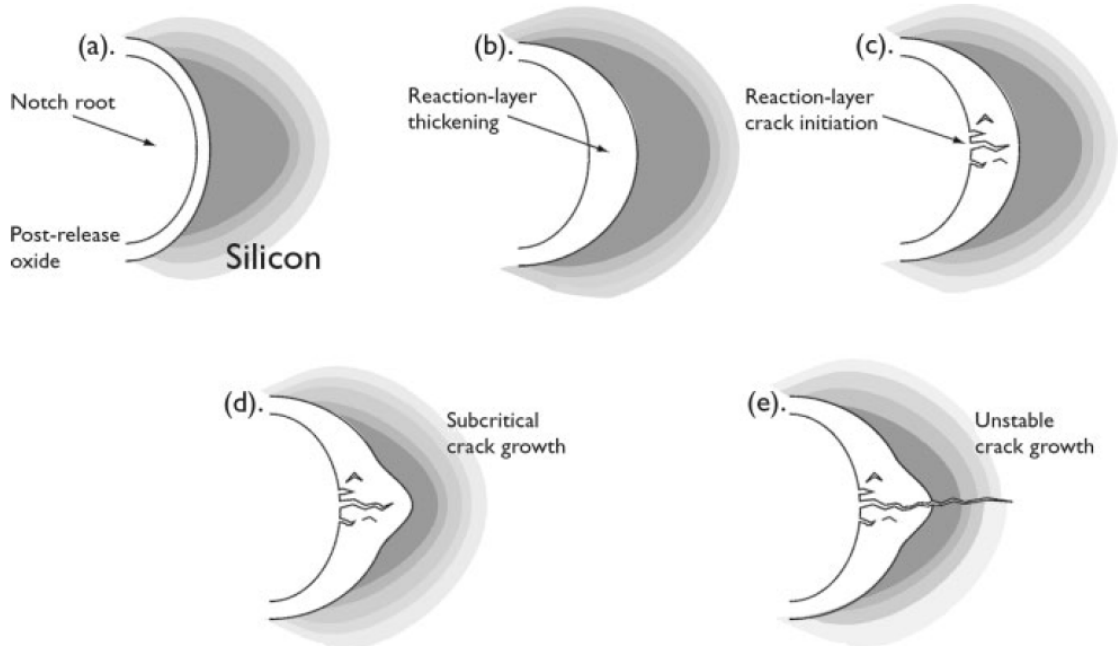

Figure 5: Schematic illustration of the reaction-layer fatigue mechanism (a) reaction layer on Si surface, (b) localized cyclic stress-assisted oxide thickening at the notch root, (c) moisture-assisted crack initiation in the surface oxide at the notch root, (d) additional thickening and cracking of reaction-layer, and (e) unstable crack growth in the Si film [56].

However, no specific physical model has been suggested to explain the observed stress assisted oxide thickening, although there are atomistic simulations that are qualitatively consistent with the experimental results. Observations that the number of cycles to failure is frequency-independent do not appear consistent with this mechanism. To account for this feature the reaction-layer mechanism must incorporate a rate-limiting step, active for cyclic loading and inactive for monotonic, that is both cyclic stress-dependent and frequency-independent. Cyclic stress-induced surface oxidation can be such a rate-limiting step, even though there is currently no theoretical model for stress assisted oxidation that incorporates a cyclic effect [67-69]. Additionally the initial oxide thickness is essential for the reaction-layer mechanism. Pierron *et al.* showed that SiO_2-

layers as thin as 15 nm are sufficient to activate the mechanism [70]. However, the typical native oxide thickness for Si is only 2-3 nm. It is thus unlikely that such an oxide thickness can develop in the low-cycle fatigue range associated with short time to failure (<1 min). Therefore the underlying mechanism remains consequently a much disputed subject.

1.3. *Motivation for Study*

The previous sections highlighted the need to characterize the fatigue behavior of micron-scale SCSi in harsh environments. To date, most of the fatigue studies of Si thin films were performed in vacuum or mild environments, which are not relevant for MEMS applications in which the systems are directly exposed to harsh environments. It is therefore one of the main goals of the present study to investigate the fatigue behavior of SCSi films in high temperature, high humidity (80C, 90%RH) air.

In addition to its technological relevance, the present study aims at further understanding the underlying fatigue mechanisms for micron-scale Si. Based on the experimental evidence summarized in 1.2, the reaction-layer fatigue mechanism appears to be the most viable mechanism. The experimental observation of thickened surface oxides [28, 56, 62] during cyclic loading and stress corrosion cracking of thin oxide films [71, 72] are strong evidence in favor of that mechanism. However, the mechanism responsible for the stress-assisted oxidation is currently not understood, leading to apparent inconsistencies between some experimental results and the RLF mechanism. Therefore, in addition to the influence of harsh environments, the present study will focus on the following aspects:

- influence of frequency: the apparent frequency independence of fatigue lives observed in the 10-450 Hz and 40-50 kHz ranges appears inconsistent with stress-assisted oxidation. The present work addresses this issue by studying the influence of the natural frequency over a larger range: from 4 to 40 kHz.

- low-cycle fatigue (LCF) behavior: it is presently unclear whether the reaction-layer fatigue can be active in the LCF regime, due to the short time scale. One of the objectives of the present work is to therefore develop a testing technique to accurately study the low-cycle fatigue of SCSi thin films with kHz-frequency resonators.

CHAPTER 2

EXPERIMENTAL / NUMERICAL PROCEDURES

2.1. *Testing Principles*

The electromechanical structure shown in Figure 6 is used to measure the fatigue characteristics of single-crystal silicon thin films. The structure consists of a notched cantilever beam, a large mass, and two comb drives. The structure behaves as a rotational oscillator. At resonance (4 or 40 kHz), the periodic motion (see Figure 7) causes periodic capacitance changes that create induced currents proportional to the amplitude of motion. These currents are amplified and measured as an output voltage. The fatigue behavior can be thoroughly characterized by achieving accurate measurements of fatigue lives and stresses at the root of the notched cantilever beam. It is designed to quantify the fatigue damage accumulation through periodic resonant frequency measurements.

2.2. *Description of Fatigue Characterization Structures*

2.2.1. Geometries

The 10-μm thick structures consist of a 40-μm long and 20-μm wide [100] oriented notched cantilever beam attached to a toroidal mass (see Figure 6).

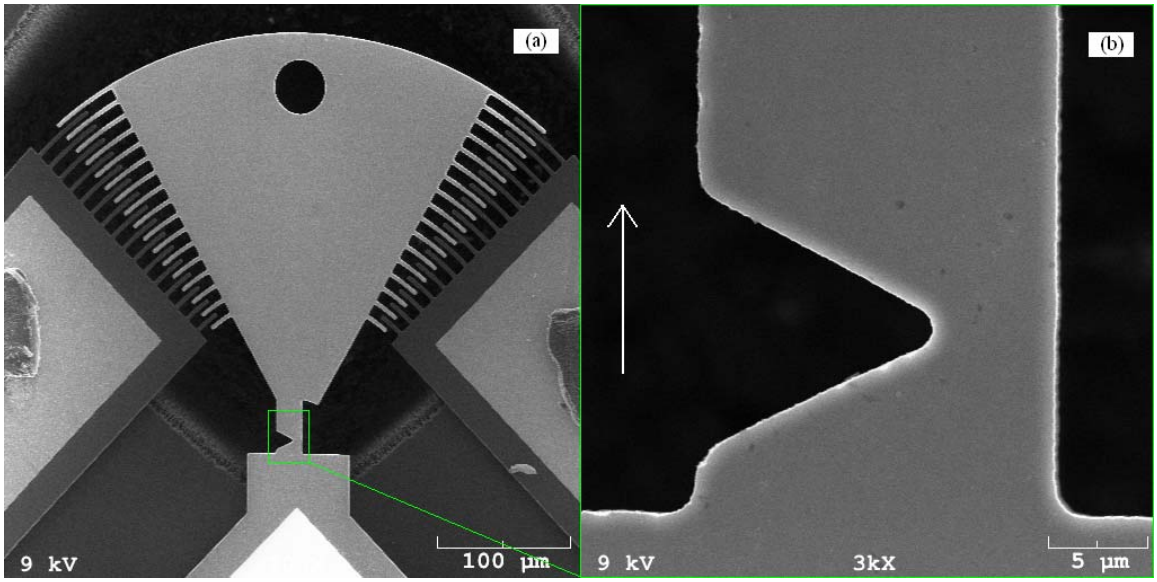

Figure 6: (a) Scanning electron micrograph of the fatigue characterization structure used in this study. (b) Zoom on the notched cantilever beam of the resonator, the arrow indicating the [100] direction in a (100) plane.

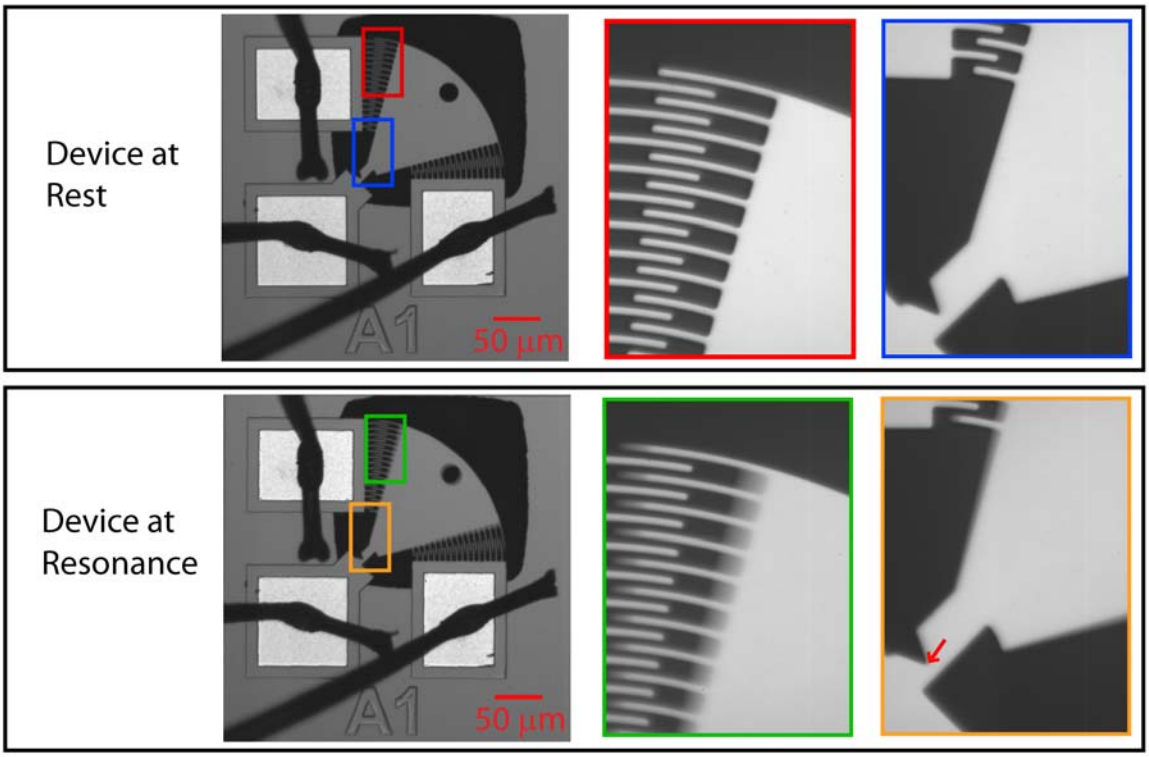

Figure 7: Optical images of the fatigue characterization structures used in this study. Top: at rest. Bottom: at resonance (~40 kHz). High magnification of the notched cantilever beam and comb drives are shown on the right for each case.

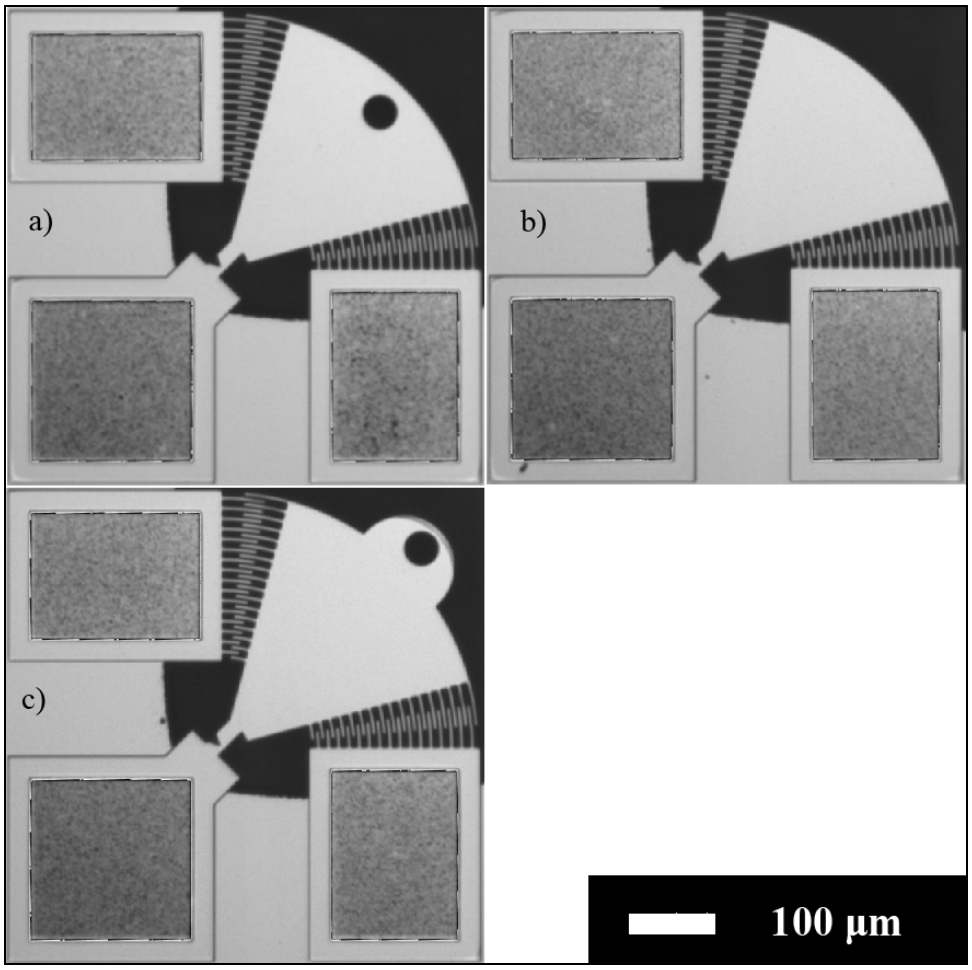

Figure 8: Optical images of resonators a) Type 1, b) Type 2 and c) Type 3.

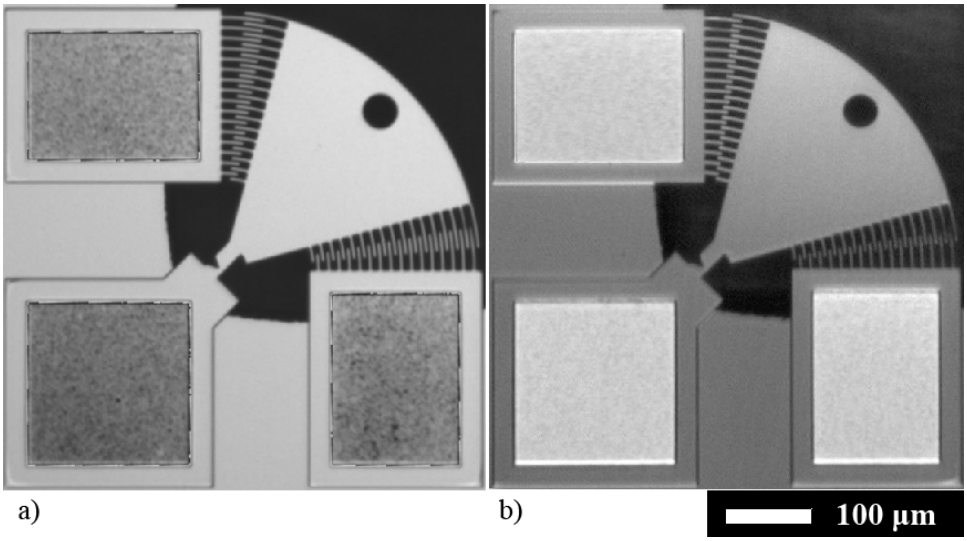

Figure 9: Optical images of: a) 5° finger overlap, b) 2.5° finger overlap, resonators.

This mass incorporates two arrays of 17 fingers interdigitated with 16 fingers on each side. This constitutes a driving and a sensing comb drive. The driving part applies electrostatic forces to the structure, while the sensing part is responsible for capacitive measurement of the displacement. The notch lies approximately at 9 μm from the base of the beam, is 13-μm deep and has a 1-μm notch root radius. Four types of resonator, named Type 1, 2, 3 and 4, were employed in this study, only differing by the geometry of the mass. In addition, two interdigitated finger overlaps were used: 5° and 2.5° (see Figure 9). The toroidal mass of Type 1, 2 and 3 (see

Figure 8) are similar, presenting a 30-μm inner radius and 300-μm outer radius. In Type 1 and Type 3 devices, the toroidal mass presents a hole at the outer edge for external actuation purposes. Type 1, 2, and 3 devices resonate in the 40 kHz range. In contrast, Type 4 devices exhibit a much larger toroidal mass (900-μm outer radius), such that the resonant frequency is 4 kHz (see Figure 10). Aluminum wirebonds provide the electrical contacts between a ceramic package and the metal pads (600 nm Au on top of 50 nm Cr). The electrostatic actuation induces the motion of the structure in the first in-plane bending mode. These devices are highly linear over a wide range of amplitudes. The generated stresses are localized to the vicinity of the notch root due to the geometry of this design. This allows applying stresses from non-damaging to catastrophic failure range at sufficiently large amplitudes.

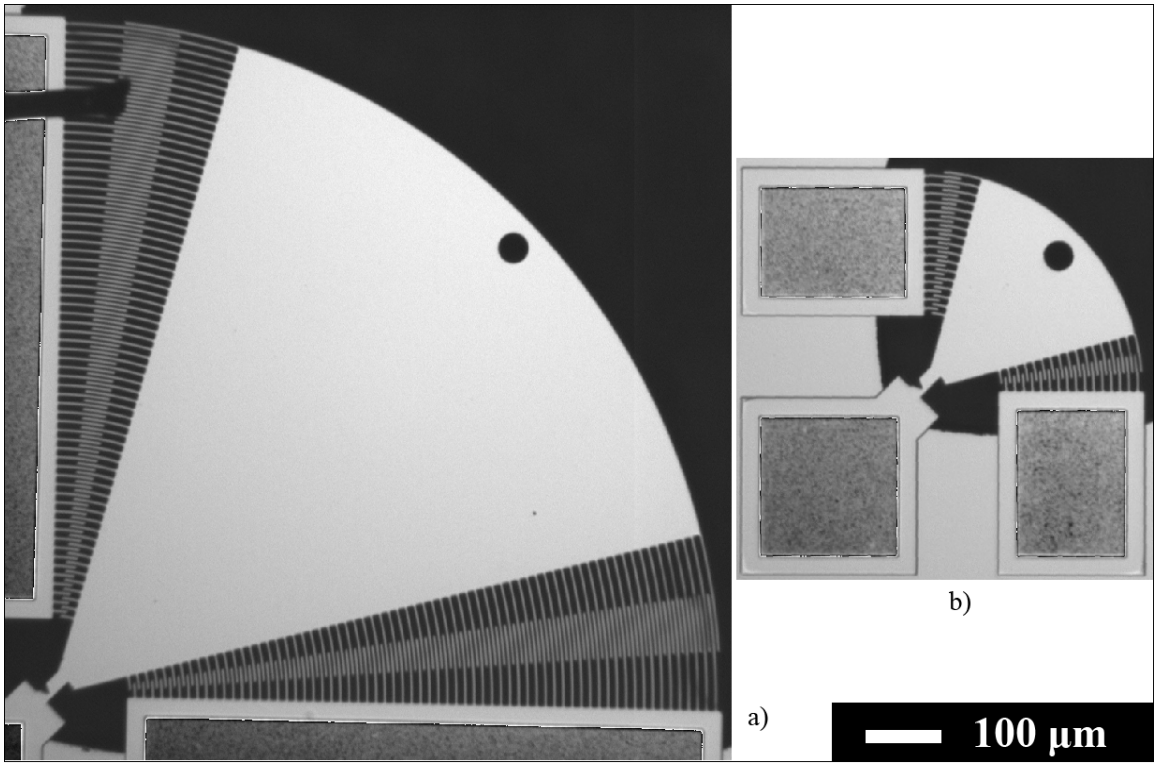

Figure 10: Optical images of resonator a) Type 4 and b) Type 1 (same scale).

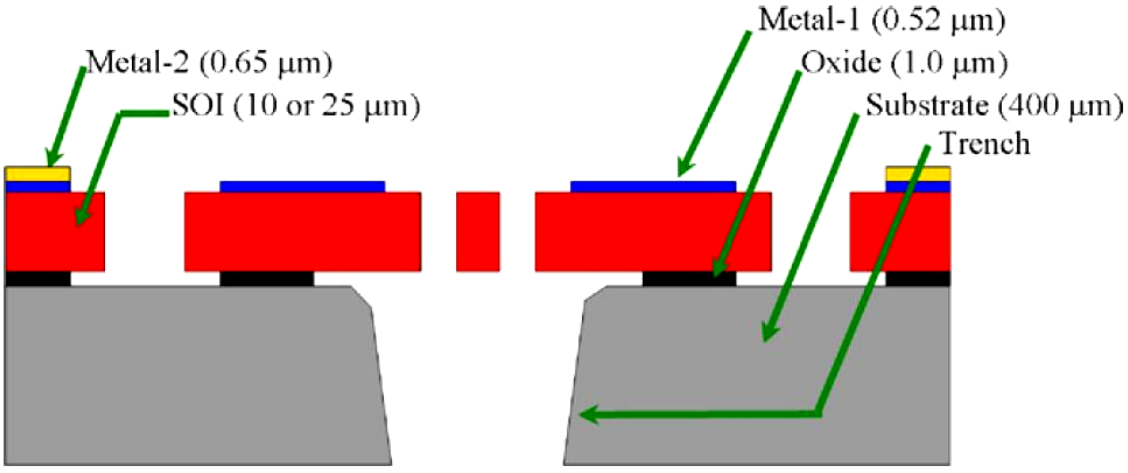

Figure 11: Schematic cross-section of an arbitrary SOIMUMPs structure. The SOI layer is composed of SCSi, and both metal layers are e-beam evaporated Au (Miller *et al.* [73]).

2.2.2. Fabrication Process

The electromechanical resonators (see Figure 6) were fabricated with the MEMScAP SOIMUMPs® process (run 20), which relies on the bulk micromachining of a silicon-on-insulator (SOI) wafer. A schematic cross-section of the SOIMUMPs technology is shown in Figure 11. This manufacturing platform uses heavily doped n-type (100) SOI wafers (described as Substrate: 400±5 μm thick), a thermally grown SiO_2 insulation layer (Oxide: 1±0.05 μm thick), a mechanically thinned SCSi layer (SOI: 10±1 μm or 25±1 μm thick), and two electron beam deposited layers of gold (as referred to as Metal-1, and Metal-2: in our case 600 nm Au on top of 50 nm Cr). The process includes a 2-μm undercut etch using vapor phase hydrofluoric acid (HF). It is used here in conjunction with the standard Bosch etch (based on Deep Reactive Ion Etching) from the backside of the underlying SCSi substrate to create through-hole structures.

Miller *et al.* [73] evaluated several SOIMUMPs fabrication characteristics (run 12 to 14) such as minimum feature size, through-thickness strain gradient, in-plane residual strain and resistivity. Table 1 underlines the main characteristics of SCSi 10-μm thick films built with these runs. The fracture strength as well as the maximum aspect ratio is sensitive to processing variations, causing varying minimum and true feature size. In-plane residual strain as well as the through-thickness strain gradients is minimal. Moreover the individual defects present on the sidewalls of the SOIMUMPs specimens constitute important features associated with the process. Miller *et al.* measured micrometer-pitched vertical striations ("curtaining") and, more important, closer pitched horizontal lines ("scalloping" see Figure 12). In their study the dimensions of these features were commensurate with the expected critical flaw size.

Table 1: Characteristics of SOIMUMPs runs 12, 13, 14 (Miller *et al.* [73])

	Value	Standard Deviation
Fracture strength (GPa)	2.27	m=12.7
Resistivity (Ω.cm)	$4.9e^{-3}$	$1.0e^{-4}$
Maximum aspect ratio	16	
Minimum feature size (μm)	~2-3	~0.1
True feature size (μm)	~0.2	~0.1
In-plane residual strain (MPa)	-3.9	1.5
Through thickness strain gradient (Maximum stress) (MPa)	14.0	0.3
Curtaining pitch (μm)	0.86	0.43
Curtaining depth (nm)	42.8	
Scalloping pitch (μm)	0.23	0.04
Scalloping depth (nm)	38.4	

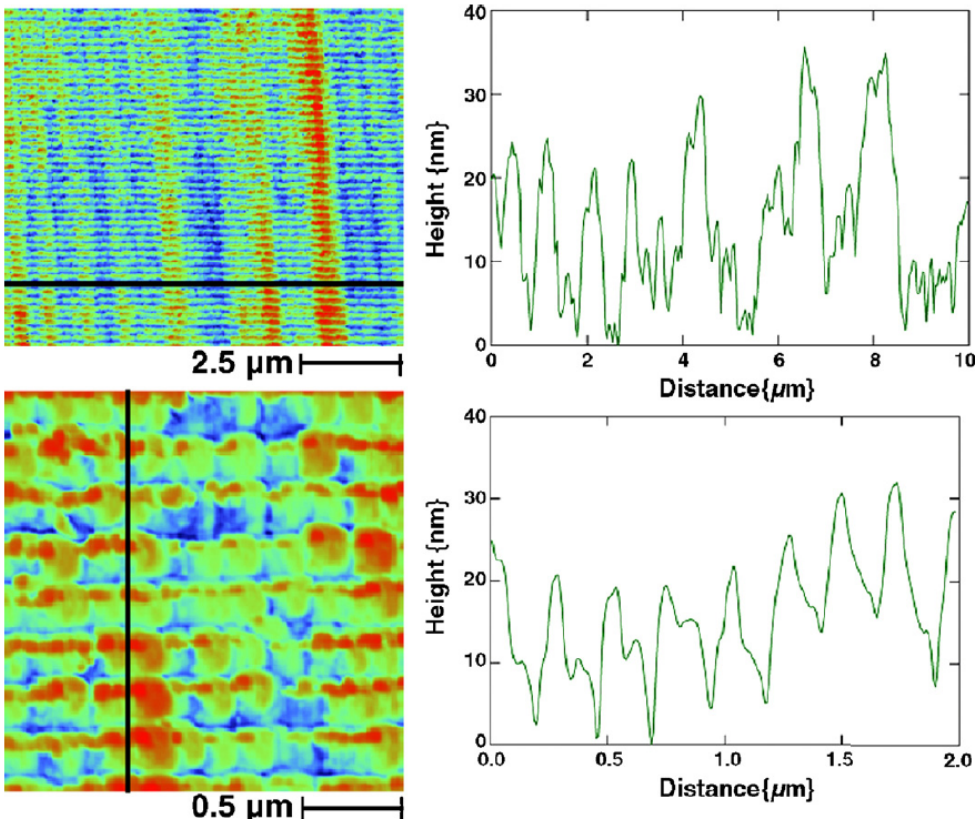

Figure 12: AFM scans of SOIMUMPs specimen sidewalls. Vertical striations are examined in the top and horizontal striations ("scallops") in the bottom. (Miller *et al.* [73])

2.3. *Dynamic Behavior of Structures*

2.3.1. Governing Equations

The fatigue characterization structure can be modeled as a one-degree-of-freedom, simple harmonic rotational oscillator, whose second-order differential governing equation is [40]:

$$J_\theta \ddot{\theta} + b\dot{\theta} + k_\theta \theta = M_0 \sin(2\pi f t) \tag{2}$$

where J_θ is the mass polar moment of inertia, b the damping coefficient (assumed constant), k_θ the torsional stiffness, $M(t)$ the amplitude of the applied moment, f is the frequency of the applied moment and $\theta(t)$ is the angle of rotation of the structure about the midpoint of the remaining ligament of the notched beam. The amplitude of the applied moment, M_0, can be expressed as:

$$M_0 = \frac{1}{4}\varepsilon h \sum_{j=1}^{32} \frac{1}{\ln(r_{0,j}/r_{i,j})} V_{in}^2 \tag{3}$$

where ε is the electric permittivity of the air, h the thickness of the structure (10 μm), $r_{0,j}$ and $r_{i,j}$ are the outer and inner radii of the j^{th} capacitor formed by two adjacent fingers, and V_{in} is the amplitude of the applied voltage. The numerical factor ¼ results from the forcing moment being a quadratic function of the applied sinusoidal waveform (the constant part of the forcing function is negligible on the overall response for lightly damped resonators, as is the case here). The solution for equation (1) is given by:

$$\theta(t) = \frac{M_0}{k_\theta} \frac{\frac{f_0}{f}}{\left[\left(\frac{f_0}{f} - \frac{f}{f_0}\right)^2 + \frac{1}{Q^2}\right]^{1/2}} \cos(2\pi f t - \delta) = \Theta \cos(2\pi f t - \delta) \tag{4}$$

where f_0 is the undamped resonant frequency, δ is a phase shift due to the damping force, Θ is the amplitude of rotation, and Q is the quality factor defined by:

$$Q = \frac{2\pi f_0}{\gamma} \tag{5}$$

where $\gamma = b/J_\theta$ is the damping ratio.

The amplitude of angular rotation at resonance, Θ_{res}, can be expressed as follows:

$$\Theta_{res} = \frac{M_0 Q}{k_\theta} \tag{6}$$

Regarding the output of this setup, the root mean square (RMS) of the AC voltage is proportional to the amplitude of the induced current signal. At resonance, the root mean square of the output AC voltage is defined as:

$$V_{RMS,res} = A\frac{f_0 Q}{k_\theta} V_{in}^2 \tag{7}$$

where A is a constant depending on the characteristics of the setup and the structure.

To summarize, these relations are used to assess the relation between stress at the notch and the input voltage V_{in} using various calibration processes. According to Eq. (2) and (5), the amplitude of rotation at resonance is directly proportional to the square of the excitation voltage, provided the damping coefficient b stays constant in the range of electrostatic forces used. This hypothesis was experimentally verified in a previous study on similar devices [32, 34, 40], and is also confirmed in the present study.

2.3.2. Transient Behavior

Low-cycle fatigue testing with the present 40 kHz structures requires measuring fatigue lives as low as few hundred of cycles while recording the accumulated damage

throughout the fatigue life. A strategy has been previously developed to accurately measure such low-cycle fatigue lives [40]: the high cyclic stress loads are applied to the specimen through bursts of finite numbers of cycles using sinusoidal voltage at f_0. Upon application of a sinusoidal excitation at the resonant frequency of the resonator, the general response $\theta(t)$ is given in this case by:

$$\theta(t) = \theta_{trans}(t) + \theta_{ss}(t)$$

$$= Ae^{-\pi f_0 t/Q}\sin(2\pi f_0 t + \phi) + \Theta_{res}\cos(2\pi f_0 t - \delta) \quad (8)$$

where $\theta_{trans}(t)$ is the transient response, $\theta_{ss}(t)$ the steady-state response, A and Φ are functions of the initial conditions and the dynamic properties of the resonator. Figure 13 illustrates the initial response of the specimen. The transient period must be neglected in order to accurately measure the number of cycles contributing to the fatigue damage. In this study, the steady state is considered obtained when the output voltage (proportional to displacement) reaches 90% of the steady-state value.

2.3.3. Influence of Environment on Quality Factor

The quality factor Q dictates the amplitude of rotation at resonance. It is necessary to measure it to accurately calculate the stress amplitude from one environment to another. However, vibratory microelectromechanical devices are influenced by viscous damping. Accordingly, it is relevant to characterize the influence of temperature and humidity on important properties such as the viscous damping coefficient b and the quality factor Q of the fatigue characterization structure.

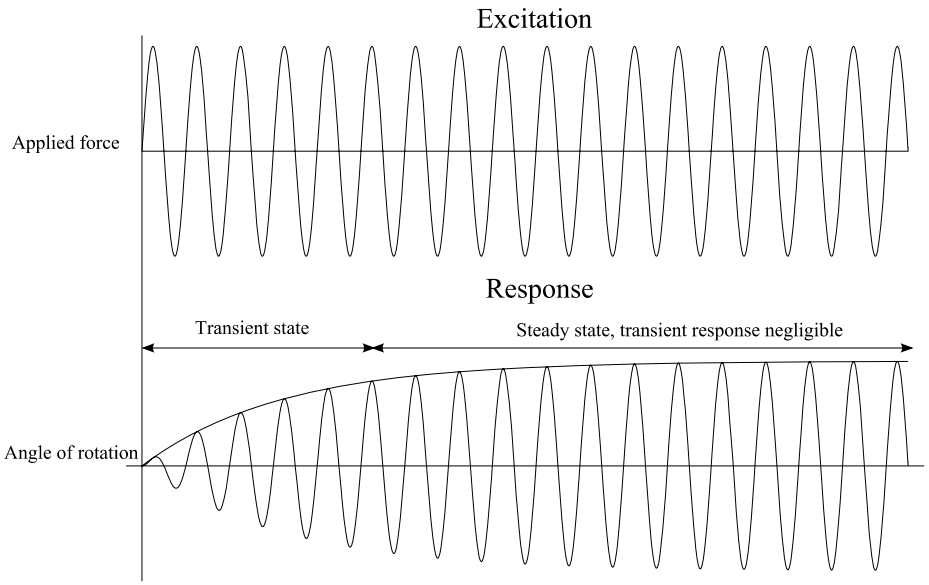

Figure 13: Schematic illustration of the initial response of a damped oscillator to a sinusoidal force applied at the resonant frequency of the structure.

Experimentally, damping is characterized via the quality factor, Q. It is defined as the ratio of the system's resonant frequency f_0 over the bandwidth f_2-f_1 where f_1 and f_2 are two frequencies for which the amplitude is equal to the square root of the peak value [74].

In the present study we consider the laterally oscillating planar structure as an infinite plate that create shear damping ($Q_{s\infty}$). The fingers attached to the plate are in motion in the vicinity of immobile driving and sensing combs (surfaces perpendicular to the plate but parallel to the motion) and also participate as shear damping, Q_{sf}. Finally the surfaces opposed to the motion contribute as squeeze-film damping (Q_{sq}). Figure 14 illustrates the location of the different types of damping associated with the fatigue resonators. The overall Q can be estimated as:

$$\frac{1}{Q} = \frac{1}{Q_{s\infty}} + \frac{1}{Q_{sf}} + \frac{1}{Q_{sq}} \tag{9}$$

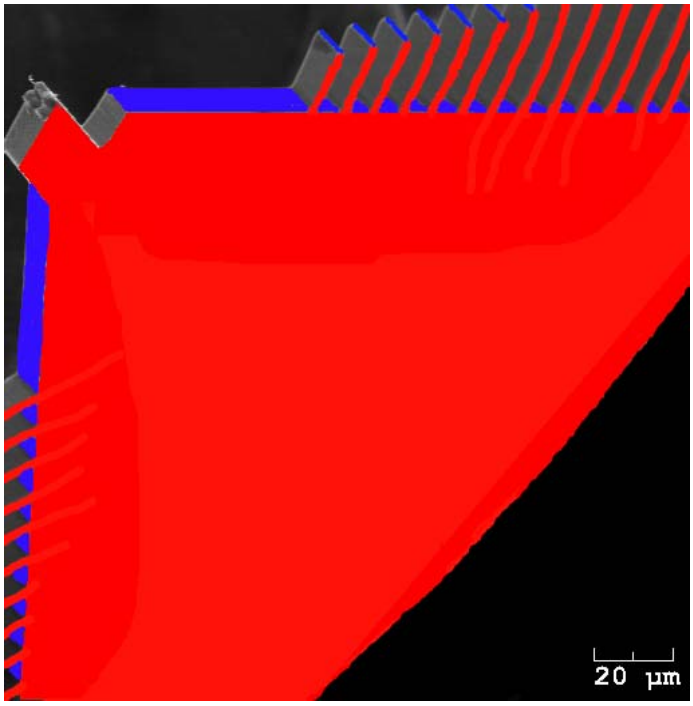

Figure 14: Schematic of a Type 2 resonator. The areas influencing $Q_{s\infty}$ are colored in red, the gray areas influence Q_{sf} and the blue areas contribute to the squeeze-film damping (Q_{sq}).

Y.H. Cho *et al*. [75] found that Stokes-type fluid motion models more accurately viscous damping than Couette-type flow field. G. Li *et al.* [74] proposed the following expression of the shear flow induced damping coefficient:

$$b_{sf} = \frac{\mu A}{h}\left[\beta h \times \left(\frac{\sin(2\beta h)+\sinh(2\beta h)}{\cosh(2\beta h)-\cos(2\beta h)}\right)\right] \tag{10}$$

where μ is the absolute viscosity, A the viscous damping area, and h the fluid thickness in inter-comb spaces. The momentum propagation velocity β is such as:

$$\beta = \sqrt{\frac{\omega}{2\nu}} = \sqrt{\frac{\pi . f_0 . \rho}{\mu}} \tag{11}$$

where ω is the circular frequency of oscillation, ρ the density of humid air, and ν the kinetic viscosity.

The dimensional modification factor within the parenthesis can be neglected for the infinite case but is of importance between the fingers. Thus the infinite shear damping coefficient and the $Q_{s\infty}$ corresponding to the damping on the main surfaces is:

$$b_{s\infty} = A\sqrt{\pi . f_0 . \rho . \mu} \tag{12}$$

$$Q_{s\infty} = \frac{\sqrt{J_\theta . k_\theta}}{b_{s\infty}} = \frac{\sqrt{J_\theta . k_\theta}}{A\sqrt{\pi . f_0 . \rho . \mu}} \tag{13}$$

In the case of shear damping between the fingers, the expression is:

$$Q_{sd} = \frac{\sqrt{J_\theta . k_\theta}}{A\sqrt{\pi . f_0 . \rho . \mu} \times \left(\frac{\sin(2\beta h) + \sinh(2\beta h)}{\cosh(2\beta h) - \cos(2\beta h)} \right)} \tag{14}$$

The above analysis reveals that the environment affects the quality factors Q_{sf} and $Q_{s\infty}$ of the resonator through two parameters: viscosity and density. The influence of the environment on the squeeze-film damping is more complex. For instance, assuming a movable plate of length *a* and width *b*, separated from a stationary one from a distance *d*, it would be expressed as follows in the case of all sides open [74]:

$$b_{sq} = \frac{768.(ab)^2.\mu}{\pi^6 d^3} \sum_{m,n\ odd} \frac{\frac{m^2}{a^2} + \frac{n^2}{b^2}}{ab(mn)^2 \left\{ \left(\frac{m^2}{a^2} + \frac{n^2}{b^2} \right)^2 + \left(\frac{\sigma}{ab.\pi^2} \right)^2 \right\}} \tag{15}$$

where $\sigma = \frac{12.(ab).\omega.\mu}{P_a . d^2}$, P_a is the atmospheric pressure and ω the pulsation.

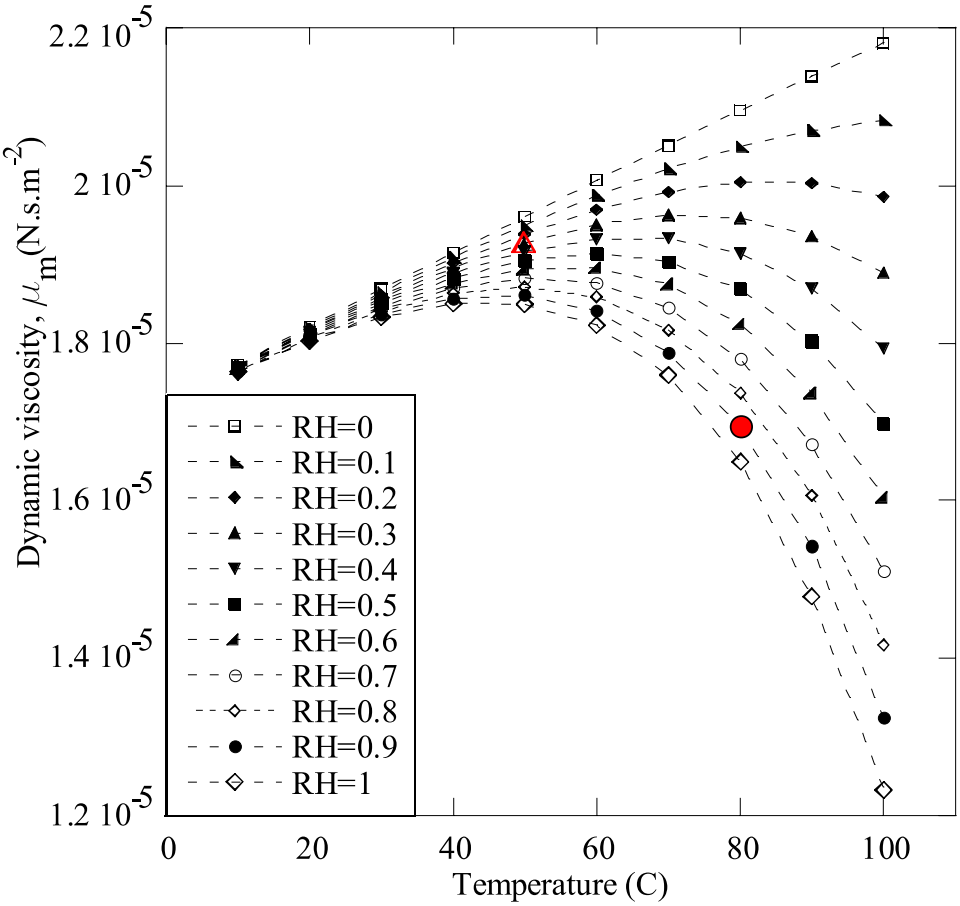

Figure 15: Dynamic viscosity, μ_m, as a function of the temperature, *T*, and relative humidity, RH. The red triangle and circle represents respectively the value at 30ºC, 50%RH (μ_m= 1.8574E-05 N.s.m^{-2}) and at 80ºC, 90%RH (μ_m= 1.5421E-05 N.s.m^{-2}).

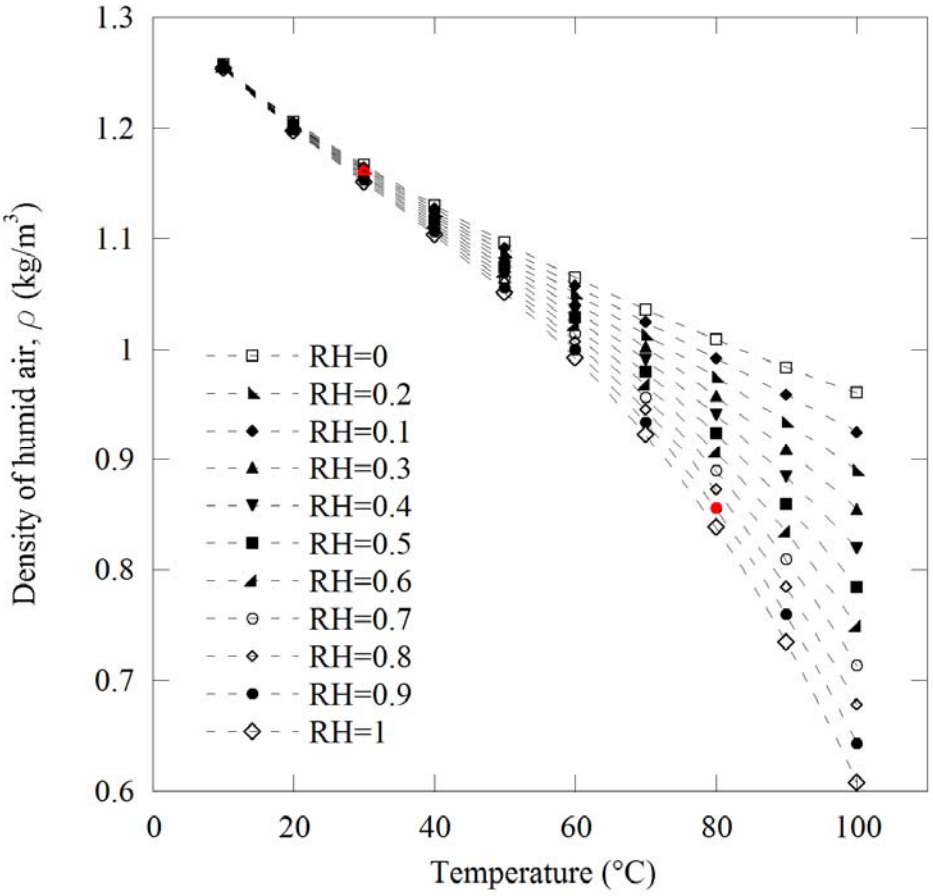

Figure 16: Density of humid air, ρ, as a function of the temperature, *T*, and relative humidity, RH. The red triangle and circle represents respectively the value at 30ºC, 50%RH (ρ= 1.1589 kg.m^{-3}) and at 80ºC, 90%RH (ρ= 0.8558 kg.m^{-3}).

As a consequence it is important to know the behavior of absolute viscosity and density as a function of temperature and humidity. P.T.Tsilingiris [76] investigated the thermophysical properties of air at temperature range between 0 and 100ºC and between dry air and saturation conditions. Based on kinetic theory considerations and on earlier investigations by Wilke [77], Reid *et al.* [78] and Hardy, absolute viscosity (for instance see Figure 15) and density of the humid air (see Figure 16) are expressed as a function of humidity and temperature. Therefore theoretical values of the different components of *Q* can be deducted.

2.3.4. Influence of Environment on Adsorbed Water Layer

In presence of humid air, multilayers of water may be adsorbed on the surface of the resonators. In order to assess the influence of water adsorption on the fatigue properties of Si, it is important to quantify the amount of adsorbed water as a function of environment. In the 1940s Brunauer *et al.* studied the adsorption isotherms of gases and the reasons underlying behind the various types [79, 80]. Two shapes of adsorption isotherm are preponderant: Type I is the well-known Langmuir adsorption isotherm, Type II is the S-shaped or sigmoid isotherm. The formation of multimolecular adsorbed layer is one of the main supposed causes. They derived the isotherm equations for multimolecular adsorption on the assumption that the same forces that produce condensation are also responsible for multimolecular adsorption. The Type II equation is given as follows [81]:

$$h = \frac{h_m . c_B . RH}{(1 - RH).[1 + (c_B - 1).RH]} \tag{16}$$

where h represents the adsorbed water layer thickness, h_m denotes the thickness of one layer of water, RH is the relative humidity and c_B is the BET coefficient, which determines the sorption curves (c_B greater than 1 indicates that the type of the Van der Waals adsorption isotherm is hydrophilic Type II). An activation energy can therefore be deduced from the BET coefficient [80]:

$$E_A = E_1 - E_L = R.T.\ln(c_B) \tag{17}$$

where E_1 represents the heat of adsorption of the first water layer, E_L is the heat of liquefaction, R the ideal gas constant and T the absolute temperature.

The high precision in the measurement of the resonant frequency for the fatigue structures enables the investigation of the resonant frequency evolution due to temperature and relative humidity changes (see 3.1). The effect of the temperature change can be quantified and decoupled from the total change in resonant frequency. Consequently the remaining relative change is considered an effect of the additional water adsorbed on the resonator. Considering $\Delta f_{total} = \Delta f_{therm} + \Delta f_{adsorp}$ where Δf_{therm} is the frequency evolution due to thermal effect on structural properties and Δf_{adsorp} is due to the absorption of water on the surface of the structure, we can derive the dependence of the resonant frequency to humidity for each temperature range. Δf_{adsorp} can be calculated as follows, assuming $\frac{J_{H_2O,i}}{J_{Si}} << 1$:

$$\frac{f_2}{f_1} = \sqrt{\frac{J_1}{J_2}} = \left[\frac{1 + 2\frac{J_{H_2O,1}}{J_{Si}}}{1 + 2\frac{J_{H_2O,2}}{J_{Si}}} \right]^{1/2} \approx \frac{1 + \frac{J_{H_2O,1}}{J_{Si}}}{1 + \frac{J_{H_2O,2}}{J_{Si}}} \approx 1 + \frac{J_{H_2O,1} - J_{H_2O,2}}{J_{Si}} \qquad (18)$$

where $J_{H_2O,i}$ and J_{Si} are respectively the moment of inertia due to the adsorbed water in the state *i* and due to the silicon fatigue characterization structure. As a consequence the relative increase of the adsorbed water thickness can be inferred from:

$$\frac{f_2 - f_1}{f_1} \approx \frac{\rho_{H_2O} . (h_{H_2O,1} - h_{H_2O,2})}{\rho_{Si} . h_{Si}} \qquad (19)$$

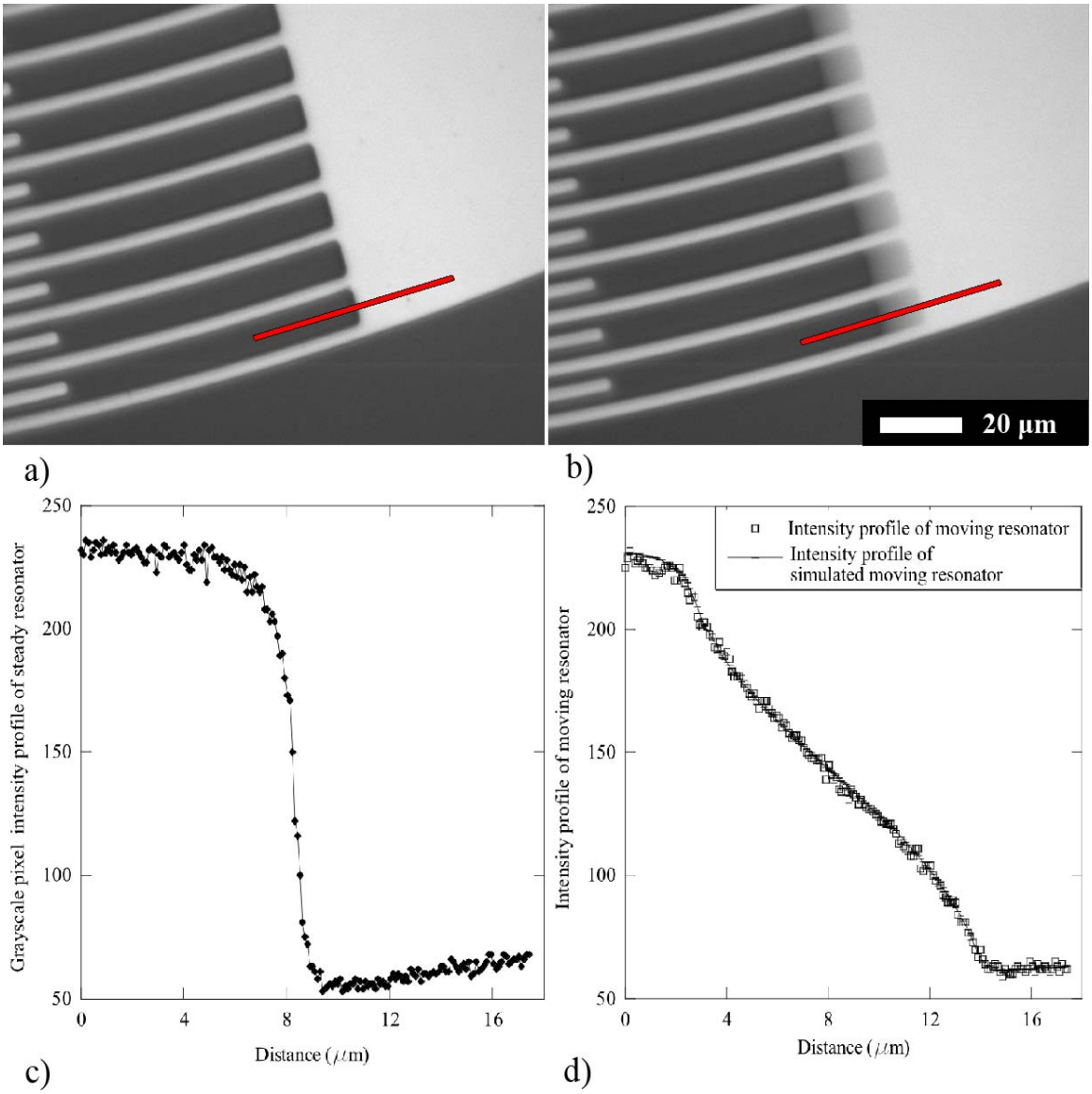

Figure 17: Optical images a) at V_{in}= 0V and b) V_{in}= 13.75V of a structure at resonance. An example of typical profile path is represented in red. c) and d) Corresponding intensity profiles. For d), both measured and simulated profiles are shown.

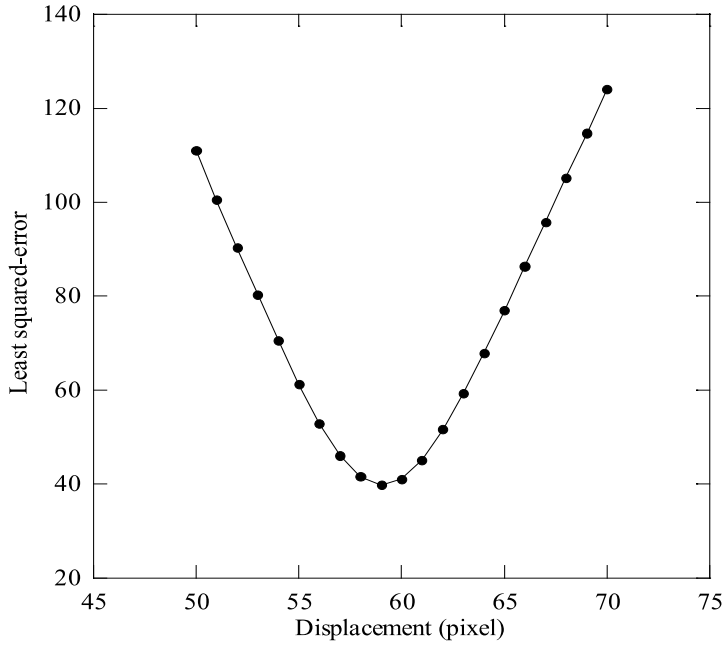

Figure 18: Least squared error between synthesized motion-image pixel intensities and the measured one. The minimum reveals the displacement in pixel.

2.3.5. Stress and Stiffness Calculation

Although the fatigue structures are nominally identical, the electrical measurements may be influenced by parasitic capacitance, which prevents the use of the output signal as an accurate metric for the generated displacements. An optical calibration technique based on the measurement of motion-blur presented by Burns *et al.* [38] is used to predict the amplitude of motion at resonance accurately. The measurement is performed using a setup of a digital camera (Jai Pulnix TM-1402CL, 1392×1040 pixels (4.65μm×4.65μm each)) equipped with a Mitutoyo 50x objective and mounted on a vibration-free platform. This simple scheme allows us to define the amplitude of rotation with a pixel size precision (for instance ±93 nm for the 50x objective).

The optical calibration step is briefly described. Basically a pixel integrates the light from a stripe of pixels accounting for the rotating motion of the resonator. For each calibration one rest image and four images at different motion amplitudes are obtained (see Figure 17). The images of the device in motion are aligned to the rest image and intensity profiles are obtained along the same given path. The rest profile (see Figure 17(c)) is used for a simulation that synthesizes a sinusoidal motion using MATHEMATICA®. It estimates pixel intensities of a simulated moving pictures based on a weighted sum of the brightness R_{i+j} of a number of rest-image pixels. A homogeneous background is assumed (the brightness of the ground is identical underneath the structure). The estimated brightness S_i of the ith synthetic image pixel can therefore be described by:

$$S_i = \sum_{j=-N+1}^{N-1} \omega_j(N).R_{i+j} \tag{20}$$

with

$$\omega_j(N) = \frac{1}{\pi}\left[\arcsin\left(\frac{j+\frac{1}{2}}{N-\frac{1}{2}}\right) - \arcsin\left(\frac{j-\frac{1}{2}}{N-\frac{1}{2}}\right)\right] \tag{21}$$

Figure 17(d) shows the measured and simulated brightness profiles. The minimum least square error between both profiles reveals the amplitude of motion in pixel (see Figure 18).

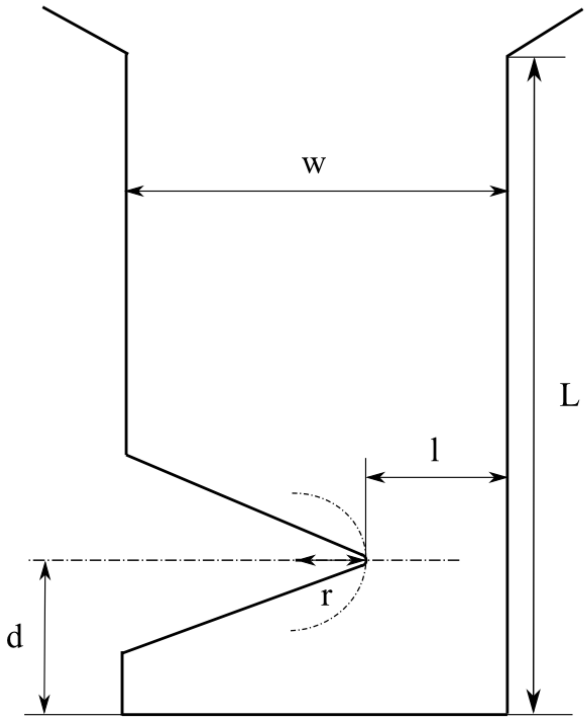

as drawn:	as measured:
L = 40 μm	L = 40.19 μm
w = 20 μm	w = 18.98 μm
d = 8.5 μm	d = 8.59 μm
l = 5 μm	l = 4.99 μm
r = 1 μm	r = 1.15 μm

Figure 19: Cantilever beam dimensions.

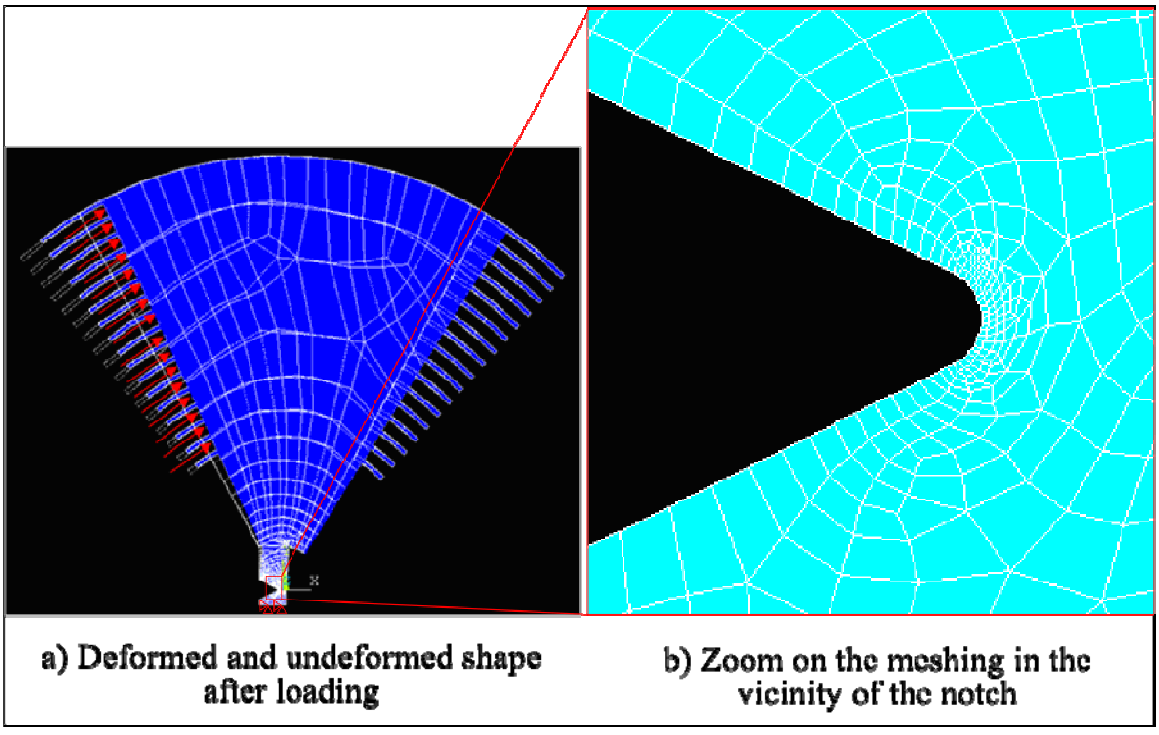

Figure 20: Finite-Element model for stiffness and stress calibration calculations.

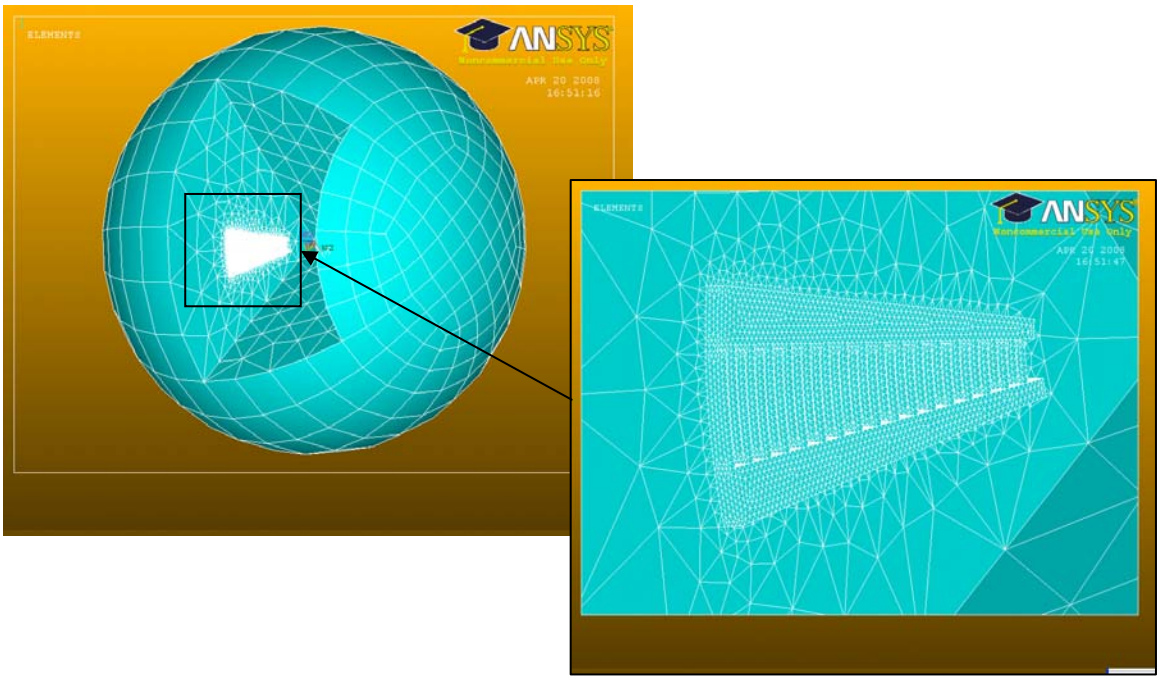

Figure 21: Finite-Element model for capacitance calculations.

The optical calibration gives a relationship between the amplitude of rotation and the applied input voltage. A 2-D-finite element modeling (ANSYS® 11.0) was employed to calculate the relationship between angle of rotation and maximum principal stress at the notch. The geometry was defined parametrically by keypoints (see Figure 19). An anisotropic elastic modulus matrix was applied corresponding to the linear orthotropic properties of SCSi in the (100) plane and [100] direction given by A. George [14]: C_{11}=165.64 GPa, C_{12}=63.94 GPa and C_{44}=79.51 GPa. The cantilever beam was clamped (zero displacement boundary condition at the bottom end) and a pressure on the left side of the mass was applied. Small displacements and plane stress state were assumed. The meshing was performed using 8-node quadratic displacement behavior elements (PLANE183) with the mesh-density locally increasing at the notch (see Figure 20). The mesh density was varied until convergence of the natural frequency of interest. The first

principal stress at the notch as well as the angle of rotation was calculated. The stiffness of the structure k_θ relates to angular rotation and applied moment M:

$$k_\theta = \frac{M}{\Theta} \tag{22}$$

A 3D electrostatic field analysis was also carried out to calculate the applied moment M_0 (see Eq. (1)) resulting from the electrostatic actuation. Eq. (2) gives a lower bound of the actual applied moment as it neglects any fringing field effects. The goal of this finite element analysis is to predict the actual value of M_0 without neglecting the fringing field effects. The model includes the 10-μm thick comb drive (fixed fingers (stator) and moving fingers (rotor)). For more symmetry the air and infinite volumes encompassing the combs were created as spheres. The relative dielectric permittivity of the two conductors was $\varepsilon_r = 11.7$, and $\varepsilon_r = 1.00054$ for the surrounding air. 20-node electrostatic elements applicable to 3-D electrostatic field analysis (SOLID122) were employed. The boundary conditions were completed with 3-D Infinite Solid far-field elements (INFIN111). These elements are used to model an open boundary of a 3-D unbounded field problem. A single layer of elements is used to represent an exterior sub-domain of semi-infinite extent. Figure 21 represents the wholly meshed FE model (size of comb elements: 3 μm, size of infinite elements: 120 μm). The mesh density was varied successively for the four meshing size variables (corresponding to the following parts: comb, air near comb drive, air away from comb drive, infinite elements) until convergence was reached. One of the most extreme cases (9.5 degrees overlap) was used to give more precision for the whole range of data. A voltage of 100V was applied to the stator part of the comb drive and the ground plate, while the rotor part was grounded. An

h-method electrostatic field analysis called CMATRIX was employed. The amplitude of applied moment was calculated as a function of rotation of the structure by computing the lump capacitance between the structure and the driving pad ("comb drive" capacitance).

2.4. *Fatigue Testing*

2.4.1. Description of Overall System

Fatigue tests are performed in a controlled environment using a temperature and humidity chamber (ESPEC SH-241 Bench-top type). The input sinusoidal voltage is applied with a waveform generator (Agilent 33220A 20MHz) and amplified with an AVTECH-110G high-voltage amplifier with the nominal gain set to 100x. The function generator verified the vendor's signal amplitude and harmonic distortion specifications. The gain of the HV-amplifier was assessed through both direct measurement and output signal. The measured gain of the amplifier used was consistently equal to 102.

For capacitive sensing, a DC bias voltage (100V) is applied with an Agilent E3612A power supply. The induced currents (~nA) generated during cyclic motion are amplified and converted to a voltage using a custom made current-voltage amplifier as depicted in Figure 22. It consists of an 'off-chip' circuit containing an operational amplifier (OPA 128). It attenuates also some of the feedthrough of the driving signal at half the resonant frequency of the structure.

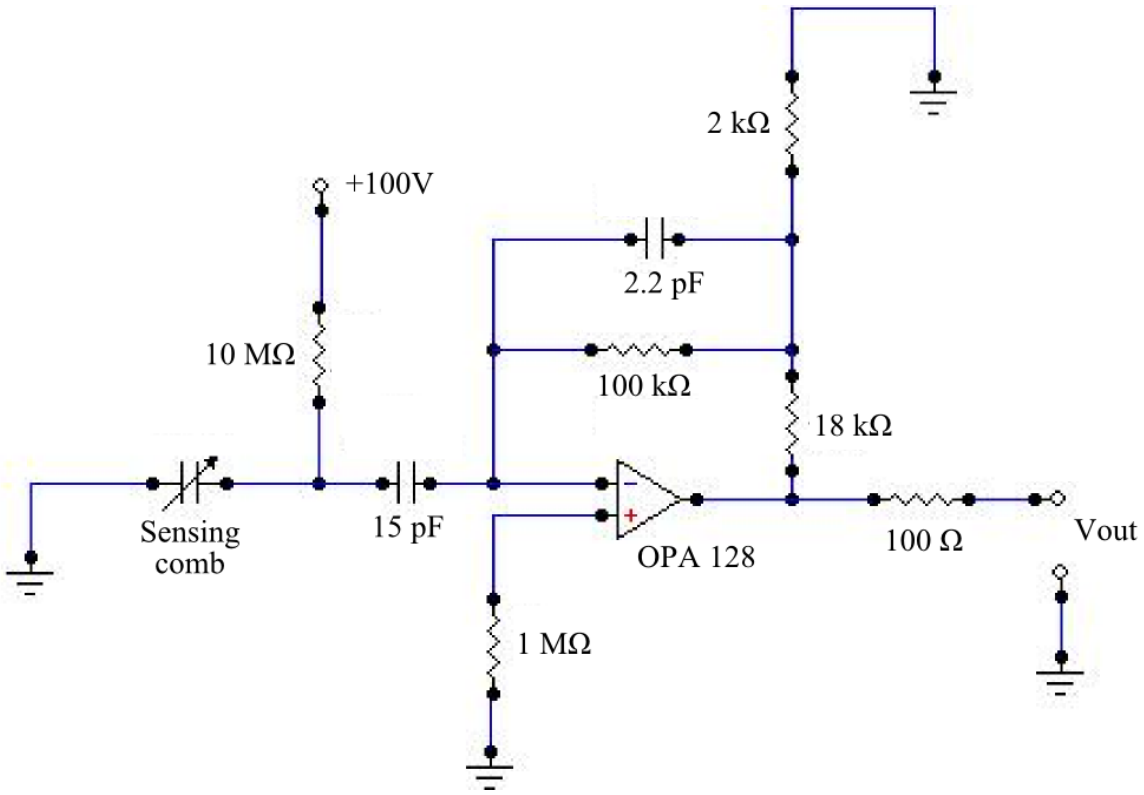

Figure 22: Schematic of the current-voltage amplifier.

The transfer function of the converter as well as its long-term stability was measured in different environments (see Figure 23). The latter signal is then measured with a lock-in amplifier (SR830-100 kHz DSP synchronized with the waveform generator) that can detect small signals very accurately even if superposed with noise sources. This signal is measured at the second harmonic of the input sinusoidal voltage. In the present study, the output voltage (proportional to the amplitude of rotation) is monitored while applying large stresses. The maximum acquisition rate of the lock-in amplifier is 512 Hz; therefore each data point represents the temporal average of the last 80 cycles.

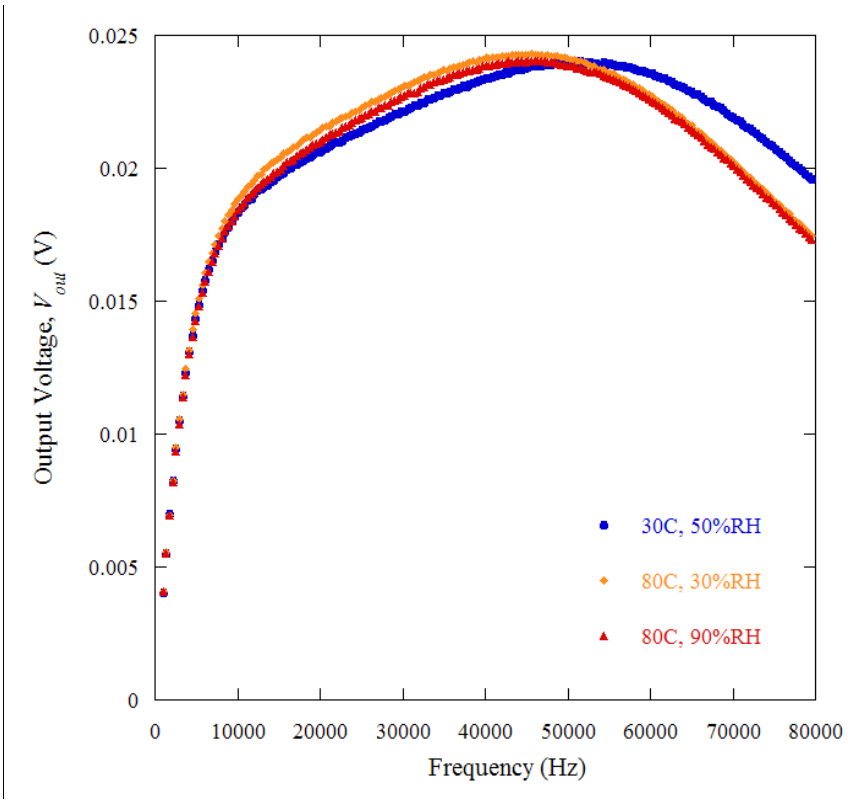

Figure 23: Transfer functions of the current-voltage amplifier measured for 50 nA of input current. This current was generated by supplying 50 mV over a 1 MΩ resistor.

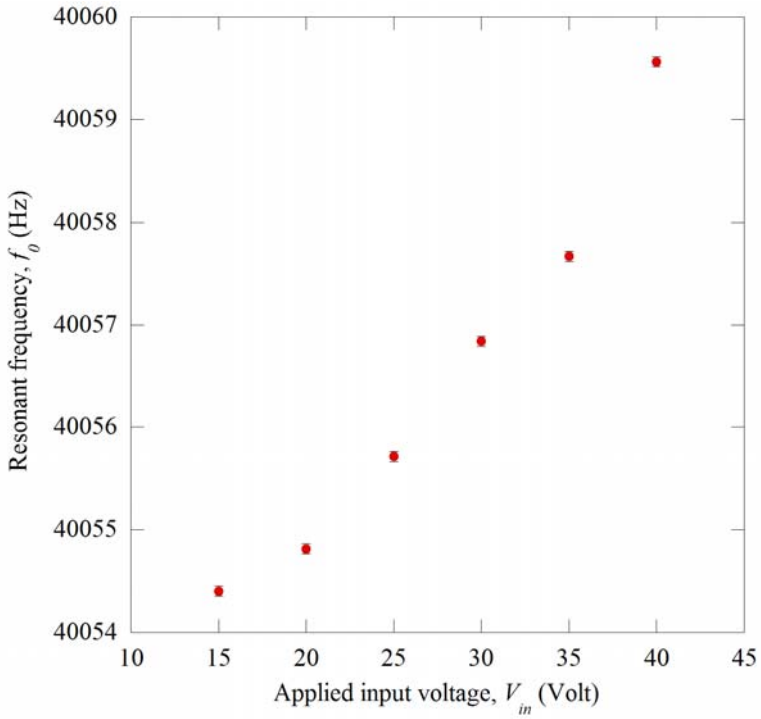

Figure 24: Dependence of f_0 on applied voltage V_{in}, indicating a weak nonlinear behavior.

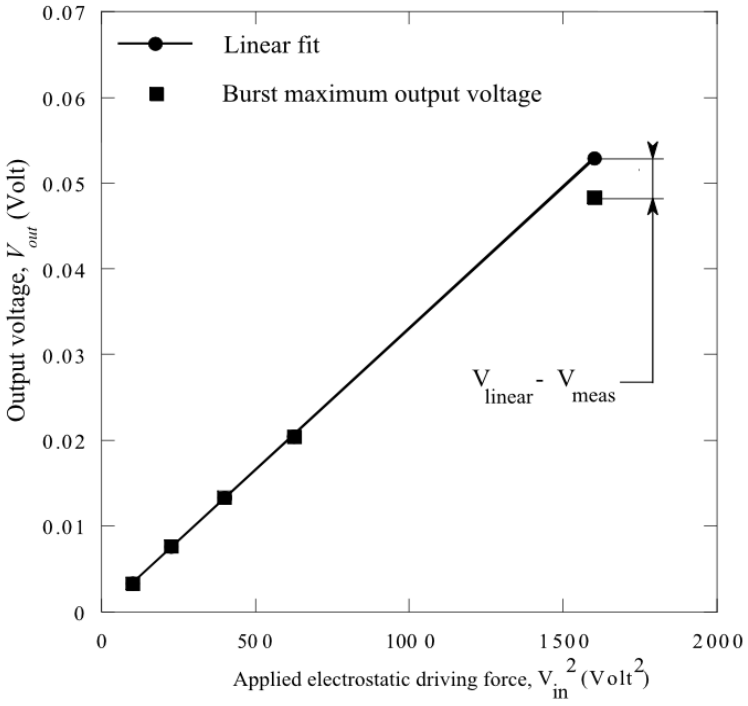

Figure 25: Electrical calibration using the dependence of the sensing circuit output voltage with the applied electrostatic driving force. The last point of the calibration is usually calculated from the measured slope at non-damaging stresses.

The dynamic testing system includes two different parts: a hardware platform and a software platform. The hardware platform consists of a computer, external GPIB instruments and custom-made driving and sensing circuits. The environmental chamber as well as the waveform generator and the lock-in amplifier are controlled through GPIB or RS-232 bus. The software platform consists of a fatigue testing module controlled by LabVIEW® software that performs control of parameters, acquisition, transformation and publication of data. The amplitude of the response and the number of cycles effectively applied are also recorded. The fatigue tests are implemented in a mild environment (30±0.1ºC, 50±1%RH) or in harsher ones (80±0.1ºC, 30±1%RH / 80±0.1ºC, 90±1%RH). Moreover the optical calibration setup being too voluminous for the environmental chamber this important step of the stress calibration is done in laboratory air.

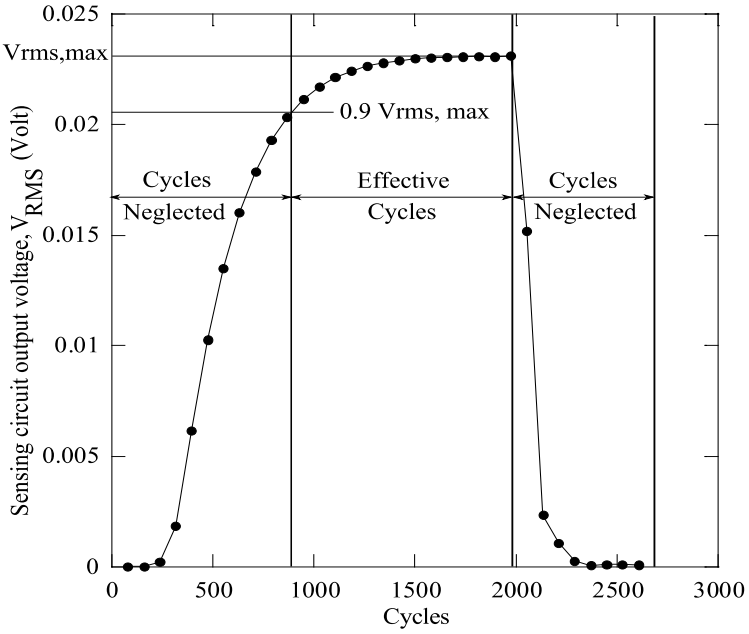

Figure 26: Sensing circuit output voltage as a function of the cycles applied during a high stress burst. The start of the burst and its transient state are observed. The effective cycles correspond to: $V_{RMS}>0.9\times V_{RMS,\,max}$.

2.4.2. Testing Protocol – LCF Testing

Low-cycle fatigue tests as well as very high-cycle fatigue tests were achieved. The following concerns mainly the designed LCF technique. It consists of applying successive bursts of small numbers of cycles (as low as ~500 cycles) at high stresses and measuring the resonant frequency in between each burst. The resonant frequency is evaluated periodically by sweeping over a frequency range. These sweeps are done at low stress values at the notch (low driving voltage) in order to avoid any additional fatigue damage. Up to five successive sweeps can be used to quantify the reproducibility of the results. For each sweep, the maximal amplitude of output voltage is found by fitting a 2^{nd}-order polynomial to the acquired data. The driving frequency is adjusted accordingly.

During each burst, the output voltage (proportional to amplitude of rotation) is measured at a rate of 512 Hz, which allows accurate determination of the effective number of cycles applied during the burst (see Figure 26). An automated testing station is designed to implement a loop of this method. As a result, small changes in f_0 associated with low-cycle fatigue can be experimentally measured, allowing quantification of the damage accumulation rates. Damage accumulation, beginning after the first burst, can be observed based on the decrease in resonant frequency of the fatigue testing structure. Nevertheless, a weak nonlinear dynamic behavior is observed, as illustrated in Figure 24 showing the influence of applied voltage on the measured f_0. Theoretically, a linear behavior should correspond to a constant f_0. The slight increase observed may result from a stiffness hardening behavior (Duffing-type behavior). This effect is taken into account for accurate measurement of the stress amplitudes during LCF testing:

$$\sigma = \sigma_{linear} \times \frac{V_{meas}}{V_{linear}} \tag{23}$$

with V_{linear} is the predicted output voltage (in the case of a perfectly linear resonator) while V_{meas} is the measured output voltage during the burst.

An electrical calibration at low voltages is therefore performed to compare the predicted amplitude of rotation / output voltage (in the case of a linear resonator) with the measured value (that accounts for the slight nonlinear behavior). Figure 25 represents an electrical calibration verifying the linearity between the output voltage and applied force. It gives an example of the difference of motion amplitude caused by the non-linear behavior. Therefore the recording of the output voltage during the burst is needed to accurately calculate the applied stress.

2.5. *Failure Analysis*

The fracture surfaces of representative specimens can provide further information on the initiation and failure mechanism. Fractographic analysis was conducted on failed devices using scanning electron microscopy (SEM). The LEO 1530 Thermally-Assisted Field Emission (TFE) Scanning Electron Microscope was used for imaging at 5 kV and 10 kV accelerating voltages. A micromanipulator was used to pick up the failed resonators, by means of the inherent micron-scale adhesive forces. The resonators were then fixed on a low profile 45/90° SEM mount pin using conductive epoxy (cured for 5 min at 115°C) or conductive adhesive tape. No conductive coating was necessary for the imaging of the specimens.

CHAPTER 3

EXPERIMENTAL AND NUMERICAL RESULTS

3.1. *Influence of Environment on Adsorbed Water Layer Thickness*

The testing method previously described was adapted to measure resonant frequency (f_0) and quality factor (Q) over a wide range of temperature (T) and relative humidity (RH). The temperature ranged between 20 and 80°C while the relative humidity varied from 30 and 90%RH, with respective steps of 10±0.1°C in temperature and 10±1%RH in relative humidity. The typical standard deviation of the f_0 measurement is 0.02 Hz while the standard deviation for Q is 5. Three tests on different resonator types were implemented. Figure 27 and Figure 28 represent the f_0 results obtained for a 25-µm thick resonator (Type 3, 2.5°-finger overlap), as a function of RH and T, respectively. We observe a slight decrease in f_0 for increasing RH values. Assuming that k_θ remains constant (the additional stiffness due to water adsorption is negligible), this effect results from the increase in J_θ due to some additional adsorbed water layers. The linear fits in Figure 28 allow a quantification of the influence of T on the elastic properties. A 3-D model of the fatigue structure has been designed to quantify the decrease in f_0 with increasing T. It contains a temperature dependent compliance matrix with data acquired by Hall [14]:

$$\frac{1}{C_{11}}.\frac{dC_{11}}{dT} = -9.4\times10^{-5}\ K^{-1}, \frac{1}{C_{12}}.\frac{dC_{12}}{dT} = -9.8\times10^{-5}\ K^{-1} \quad \text{and} \quad \frac{1}{C_{44}}.\frac{dC_{44}}{dT} = -8.3\times10^{-5}\ K^{-1}.$$

The temperature dependence of f_0 is compared between the experimental data and the

simulation based on Hall's data. The measured values lie in the same range as the FE model, though quite lower.

Using Eq. (19) in section 2.3.4 the variation in adsorbed water layer thickness, Δf_{adsorp}, is derived for each resonator with respect to 50%RH (reference environment) as a function of RH for each *T*. Figure 29 represents the study of a 10-µm thick resonator (Type 2, 5°-finger overlap). Figure 30 corresponds to the results of the 10-µm thick resonator (Type 3, 2.5°-finger overlap) and Figure 31 to the results of the 25-µm thick resonator (Type 3, 2.5°-finger overlap). A Type-II shape isotherm, as presented by Brunauer *et al.* [79, 80], can be fitted to the present curves with a slight inflexion around 50-60%RH. The maximal decrease in calculated adsorbed water thickness is systematically observed at 80°C, 30%RH. The calculated values are respectively -1.77, -1.97 and -2.40 nm. The maximal increase is noticed systematically at 20°C, 90%RH. The calculated values are respectively 1.14, 2.78 and 3.14 nm.

Table 2: Temperature dependence of resonators' resonant frequency.

Resonator characteristics			Test	Mean slope f_0 = f(T) (Hz.K^{-1})	f_0 at 30°C, 50%RH (Hz)
Type	Thickness	Finger overlap			
2	10 µm	5º	Experiment	- 0.99786	39805.85
3	10 µm	2.5°	Experiment	- 0.92392	38459.64
3	25 µm	2.5°	Experiment	- 1.20198	36189.87
2	10 µm	5°	3-D FEM	- 1.7446	38104.72

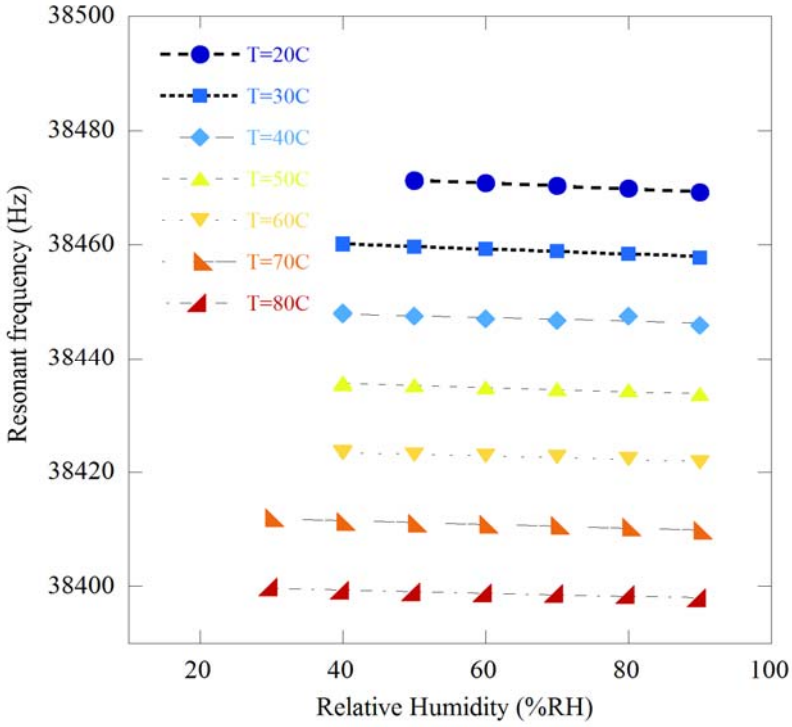

Figure 27: Influence of relative humidity (RH) on f_0.

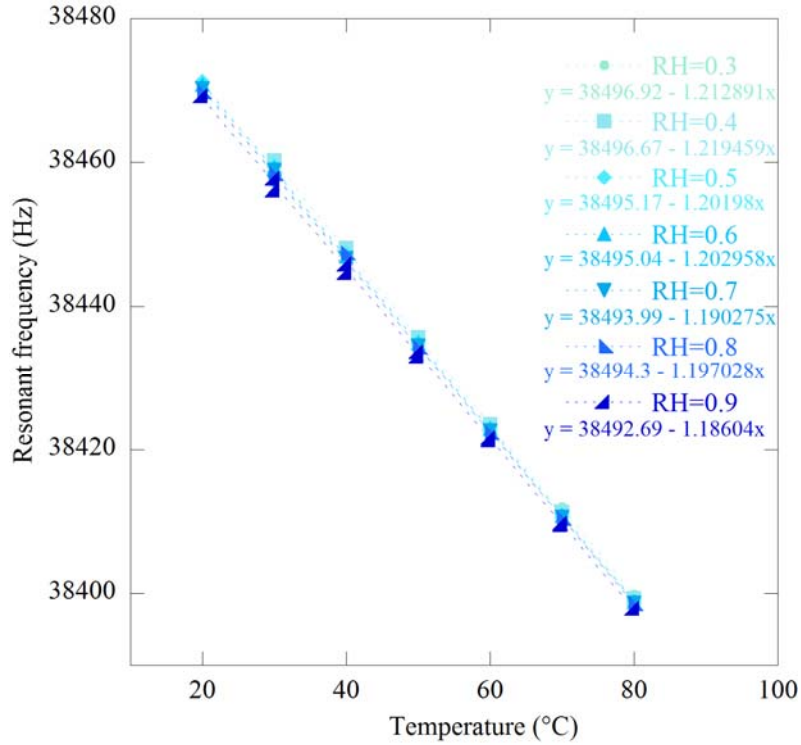

Figure 28: Influence of temperature (T) on f_0.

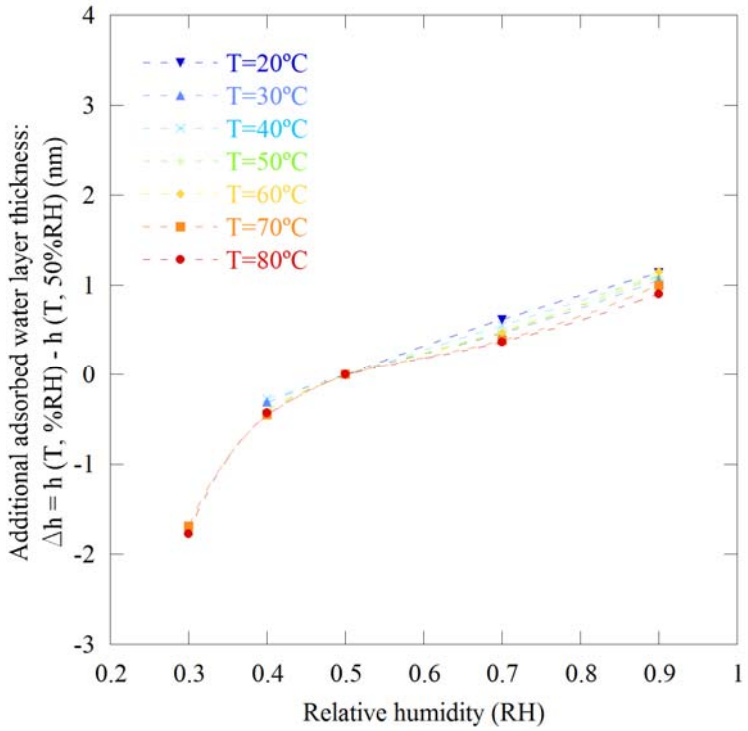

Figure 29: Calculated additional water layer thickness with respect to 50%RH as a function of RH for a 10-µm thick resonator (Type 2, 5°-finger overlap).

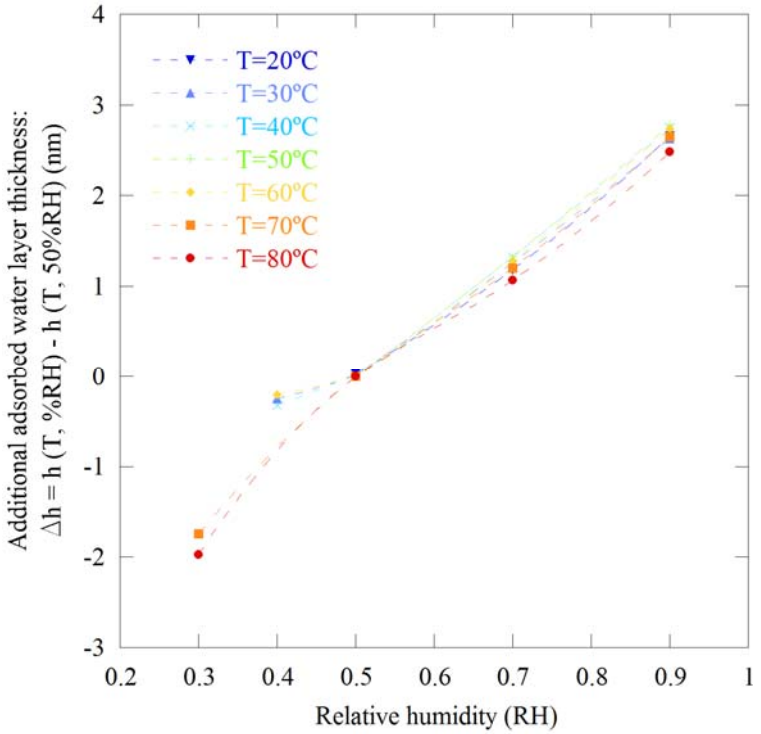

Figure 30: Calculated additional water layer thickness with respect to 50%RH as a function of RH for a 10-µm thick resonator (Type 3, 2.5°-finger overlap).

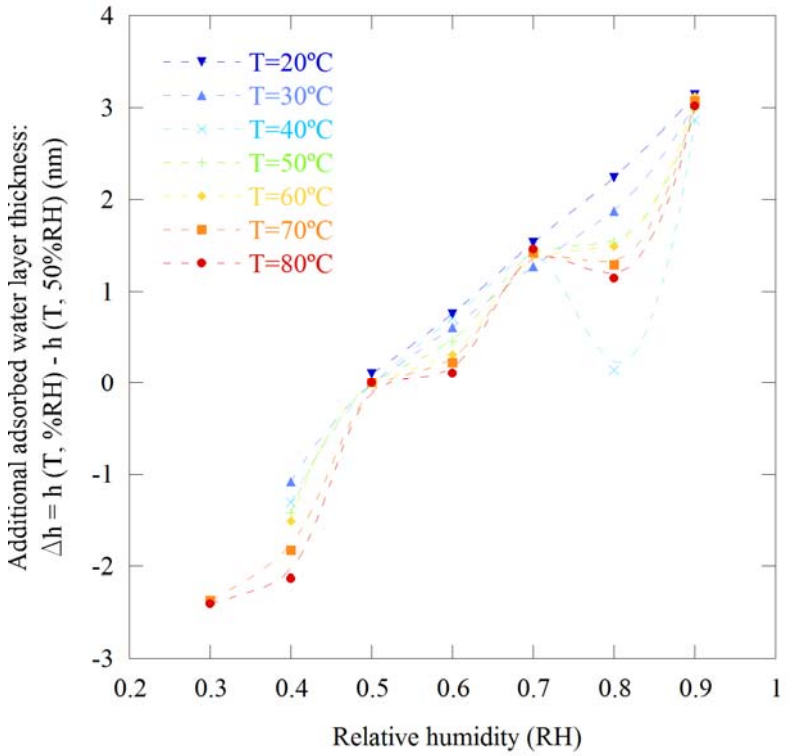

Figure 31: Calculated additional water layer thickness with respect to 50%RH as a function of RH for a 25-µm thick resonator (Type 3, 2.5°-finger overlap).

3.2. *Fatigue Testing*

3.2.1. Stress Measurements

3.2.1.1. FEM Results / Optical Calibration

The relation between stress at the notch root and angle of rotation is found according to Section 2.3.5. Assuming small displacement the linear relationship between the maximum first principal stress at the notch σ_{max} and the angle of rotation of the structure Θ is:

$$\sigma_{\max}(GPa) = 97.2 \times \Theta(rad) \tag{24}$$

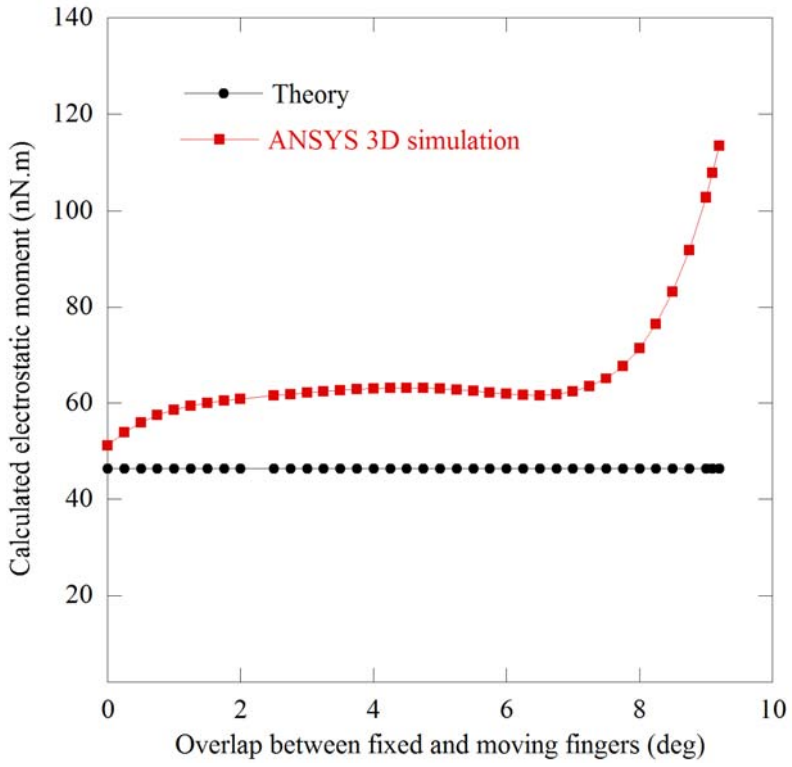

Figure 32: Calculated applied moment M_0 as a function of overlap between the fixed (stator) and moving (rotor) fingers (the overlap is 5° at equilibrium).

Figure 32 displays the results of the 3-D finite element electrostatic study. It suggests that the electrostatic moment M_0 is not affected by the angle of rotation as long as the amplitude of rotation does not exceed 2.75° for a 5°-finger overlap specimen and 2° for a 2.5°-finger overlap. This corresponds respectively to stress amplitudes of 4.66 and 3.4 GPa at the notch. Therefore, assuming a linear dynamic behavior appears to be very reasonable. Moreover this ANSYS model predicts an increase in induced moment amplitude of 34.6%. This is consistent with the relative increases from theoretical calculation to experimental calibration reported in Table 3 (+34.3±0.8% for Type 1 for instance).

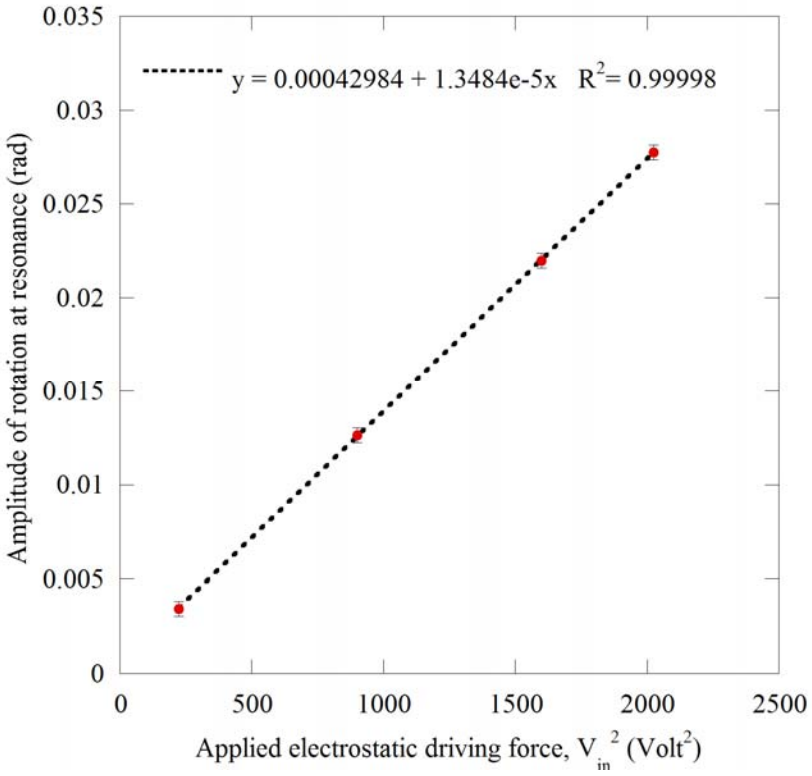

Figure 33: Amplitude of rotation at resonance (optically measured) as a function of the applied electrostatic driving force.

Figure 33 represents a typical optical calibration according to Section 2.3.5. A profile path is chosen to gather the amplitude of rotation at 292.5 (Type 1-3) or 892.5 μm (Type 4) from the axis of rotation. The precision of the rotational amplitude is of ±1 pixel. The precision of the calibration is therefore as low as ±0.0182° (Type 1-3) or ±0.0059° (Type 4) with the 50x magnification lens. The amplitude of rotation is found to be proportional to the square of the input voltage amplitude (see Figure 33). Table 3 gives the mean and standard deviation of the measured slopes for type 1, 2, 3 and 4.

Table 3: Ratio $\frac{\Theta_{res}}{V_{in}^{2}}$ (rad.V^{-2}), comparison between FEM simulations and experiments (optical calibration).

	Eq. (6)	Theory + fringing fields	Experiments	Standard deviation
Type 1	9.752×10^{-6}	1.313×10^{-5}	1.309×10^{-5}	7.762×10^{-7}
Type 2	9.930×10^{-6}	1.337×10^{-5}	1.309×10^{-5}	8.888×10^{-7}
Type 3	1.006×10^{-5}	1.355×10^{-5}	1.398×10^{-5}	3.202×10^{-7}
Type 4	2.246×10^{-5}	3.024×10^{-5}	3.066×10^{-5}	3.287×10^{-6}

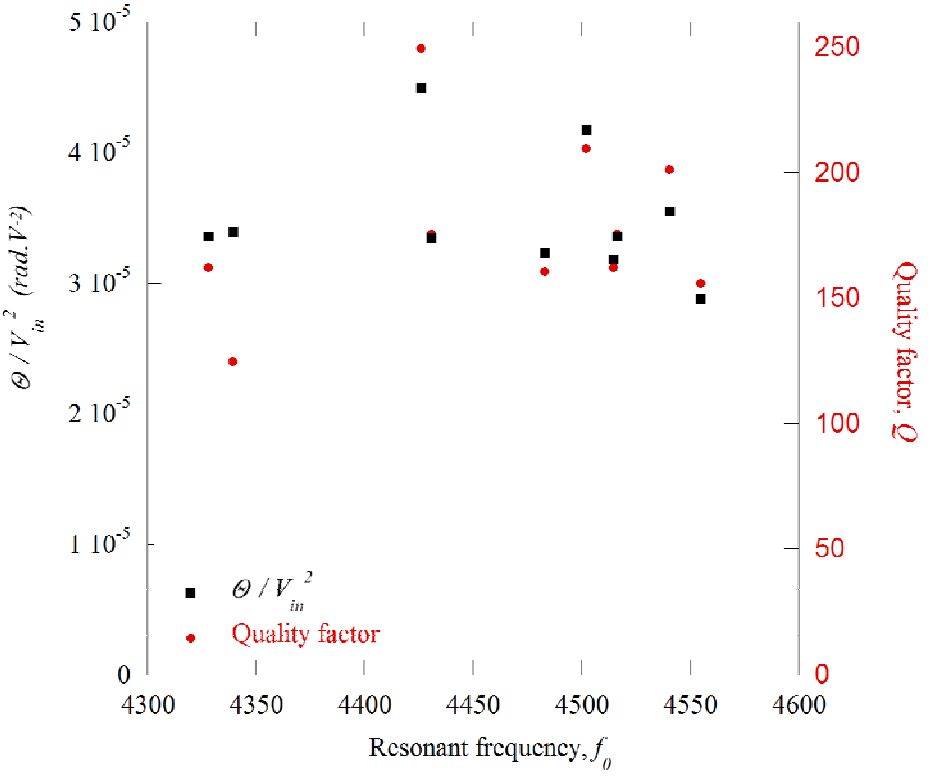

Figure 34: Comparison between the ratios (Amplitude of rotation at resonance Θ / V_{in}^{2}) and quality factors, measured respectively by optical calibration and electrical response for Type 4 resonators.

Table 4: Summary of measured quality factors at 30°C, 50%RH.

Type / Thickness	5º-finger overlap		2.5º-finger overlap	
	Q	Standard deviation	Q	Standard deviation
1 / 10 μm	723.5	13.5	822.5	28
2 / 10 μm	747	12.5		
3 / 10 μm	718.5	3.5	780.5	9.5
4 / 10 μm	169	9.5	212	25
1 / 25 μm	958.5	19.5	1114.5	22
2 / 25 μm	1039	22		

3.2.1.2. Influence of Geometrical Properties and Environment on Quality Factor

As seen with Eq. (6) the ratio Θ / V_{in}^2 is linearly related to Q. Figure 34 shows experimental data for the 4-kHz resonators that support largely this assumption. We observe a very good match between optical calibration results and quality factor values measured with electrical responses. This can be an additional verification for the calibration. The next section presents a summary of the influence of different environments on Q.

Table 4 presents the measured values of Q and the standard deviation among the various resonator types at 30°C, 50%RH. Q is sensitively larger for 2.5°-finger overlap resonator, as it is also the case for thicker specimens, and it drops dramatically for Type 4 resonators. Table 4 shows the calculated Q values from shear damping and the deduced values for squeeze damping. Based on the as drawn dimensions, Eq. (13) and (14) (see

2.3.3) provide theoretical values for the plate shear damping, $Q_{s\infty}$, and the fingers shear damping, Q_{sf}. The squeeze-film damping, Q_{sq}, can therefore be deduced from Eq. (9) and the experimental values of Q. The range of values expressed for Q_{sq} comes from the standard deviation from the experimental quality factor data. $Q_{s\infty}$ and Q_{sf} evolves as $\frac{k_\theta^{\frac{1}{4}}.J_\theta^{\frac{3}{4}}}{A}$, which means that $Q_{s\infty}$ is proportional to the resonator's thickness, while Q_{sf} remains constant. A is the respective damping area described in 2.3.3. The squeeze-film damping Q_{sq} is logically quite comparable between these two types of 5°-finger overlap resonators when applying Eq. (9) and the measured quality factors. These observations account consequently very well for the decreased damping for 25-µm thick resonators.

Moreover Q_{sf} increases as the finger overlap is reduced to 2.5°. In fact Q_{sf} contains two parts: the shear damping between fingers separated by 3 µm of air, $Q_{sf\text{-}3}$, and the shear damping between fingers separated by 9 µm of air, $Q_{sf\text{-}9}$. As a quite reliable approximation $Q_{sf\text{-}3}$ is considered being divided by 2 for a 2.5°-finger overlap, while $Q_{sf\text{-}9}$ would be multiplied by 1.5. However $Q_{sf\text{-}9}$ is almost three times smaller than $Q_{sf\text{-}3}$. As a consequence an effective increase of 32.8 and 32.0% is observed for Q_{sf}. However this augmentation would not account for the substantial decrease of total damping. Additionally the calculation of Q_{sq} reveals that the squeeze-film damping value decreases from 16 to 20.5% as the finger overlap is reduced from 5° to 2.5°. It is explained by the distance increased between the finger tips and the proof mass sides (7.5° vs. 5°). The squeeze-film damping is also logically observed quite comparable between these two types of 2.5°-finger overlap resonators. To summarize these observations account very well for the decreased total damping of 13.6 to 16.2%.

We calculated values for the different components of the quality factor at 30°C, 50%RH. From section 2.3.2 we also know the dependence of $Q_{s\infty}$ and Q_{sf} with T and RH. However, as seen previously, Q_{sq} is far from linearly dependent with any variables. The following study attempts to characterize the behavior of the total damping as a function of environmental conditions. A weighting of the various damping components dependence with T and RH is implemented. Theoretical values for Q are obtained, assuming the squeeze-film damping, Q_{sq}, is constant or assuming the environmental effect on Q_{sq} is a function of $[\mu\rho]^{-1/2}$.

Relative changes in quality factor Q with respect to 30°C, 50%RH, are plotted in Figure 35 as a function of T and RH for a 10-μm thick resonator (Type 1, 5º-finger overlap) with Q_{sq} constant. Theoretical as well as experimental values are represented. A similar graph (see Figure 36) shows the same experimental values, but compared to theoretical values assuming the environmental effect on Q_{sq} is a function of $[\mu\rho]^{-1/2}$. The next two graphs (see Figure 37 and Figure 38) assume the same hypothesis and provide the data acquired for a 10-μm thick resonator (Type 1, 2.5º-finger overlap) and a 25-μm thick resonator (Type 1, 2.5º-finger overlap). The same trend is observed, and summarized as follows: higher temperatures, and, with a superior influence, higher relative humidity cause higher quality factors (mainly reliable above 50°C). This trend is quite consistent with the experiments, but quantitatively needs a more accurate equation for the squeeze-film damping. In fact we notice with Figure 35 to Figure 38 that neither of the hypotheses can predict all three experiments.

Table 5: Comparison between experimental and predicted quality factors

	Q_{exp}	$Q_{s\infty}$	Q_{sf}	$\left[\frac{1}{Q_{s\infty}}+\frac{1}{Q_{sf}}\right]^{-1}$	Q_{sq} based on Eq. (9)
5º-finger overlap / 10 µm-thick	723.5 ± 13.5	1834	3228	1169.5	$1898.5^{1993.5}_{1809}$
5º-finger overlap / 25 µm-thick	958.5 ± 19.5	4585.5	3228	1894.5	1940.5^{2022}_{1863}
2.5º-finger overlap / 10 µm-thick	822.5 ± 28	1834	4263.5	1282.5	2293.5^{2527}_{2087}
2.5º-finger overlap / 25 µm-thick	1114.5 ± 22	4585.5	4263.5	2209.0	$2248.5^{2340}_{2160.5}$

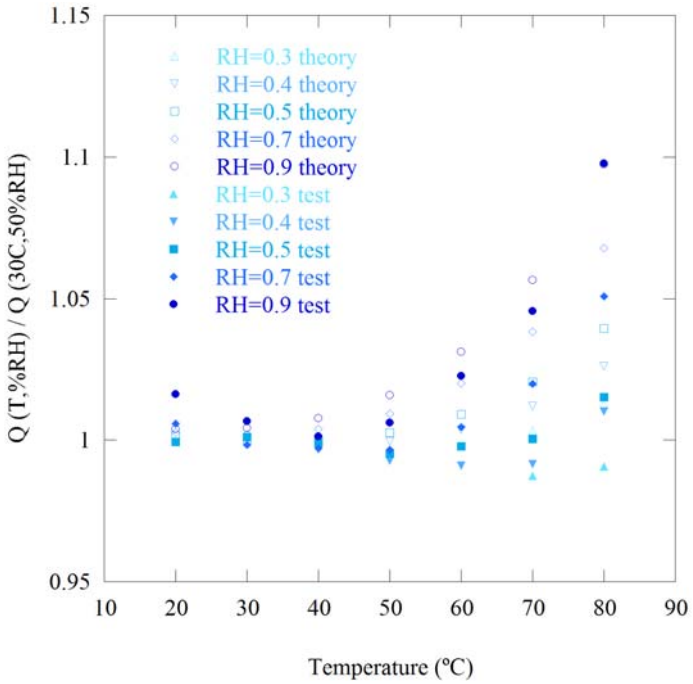

Figure 35: Relative change in quality factor Q with respect to 30°C, 50%RH, as a function of T and RH for a 10-µm thick resonator (Type 1, 5º-finger overlap). Empty symbolss indicate theoretical values for Q, assuming the squeeze-film damping, Q_{sq}, is constant.

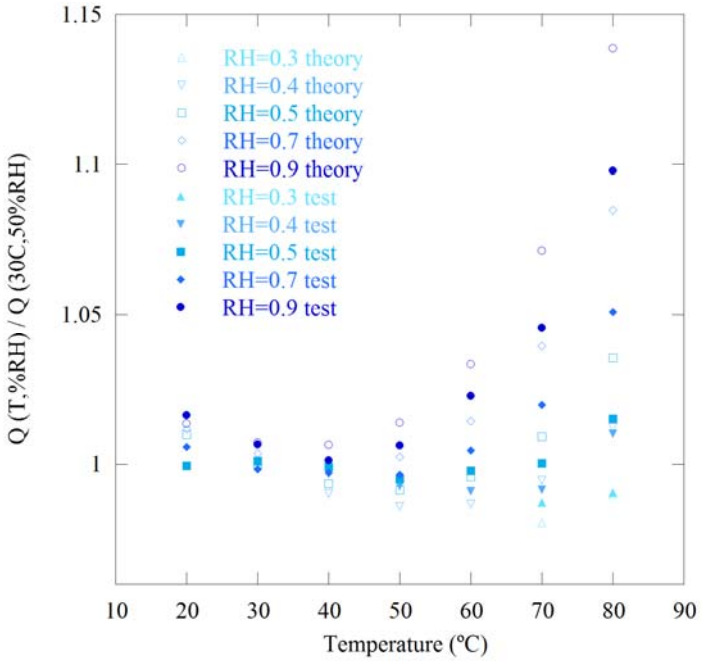

Figure 36: Relative change in quality factor Q with respect to 30°C, 50%RH, as a function of T and RH for a 10-μm thick resonator (Type 1, 5º-finger overlap). Empty symbols indicate theoretical values for Q, assuming the environmental effect on Q_{sq} is a function of $[\mu\rho]^{-1/2}$.

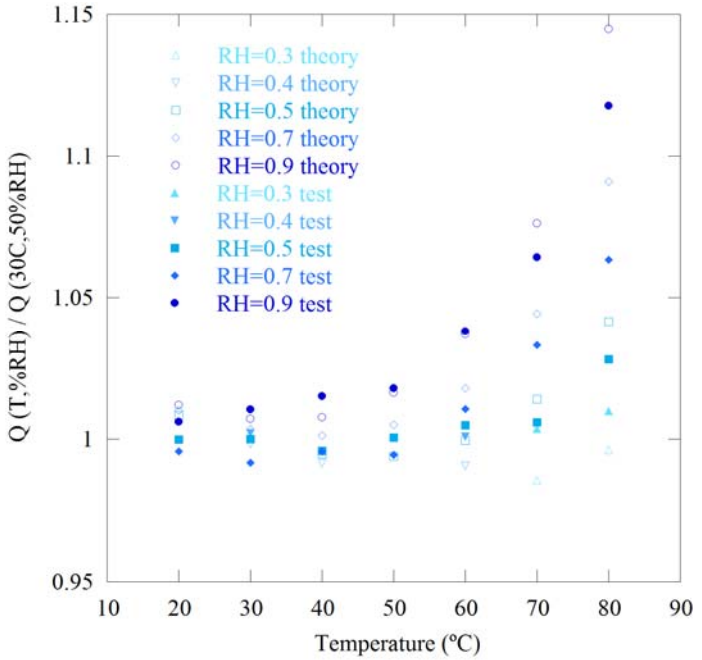

Figure 37: Relative change in quality factor Q with respect to 30°C, 50%RH, as a function of T and RH for a 10-μm thick resonator (Type 1, 2.5º-finger overlap). Empty symbols indicate theoretical values for Q, assuming the environmental effect on Q_{sq} is a function of $[\mu\rho]^{-1/2}$.

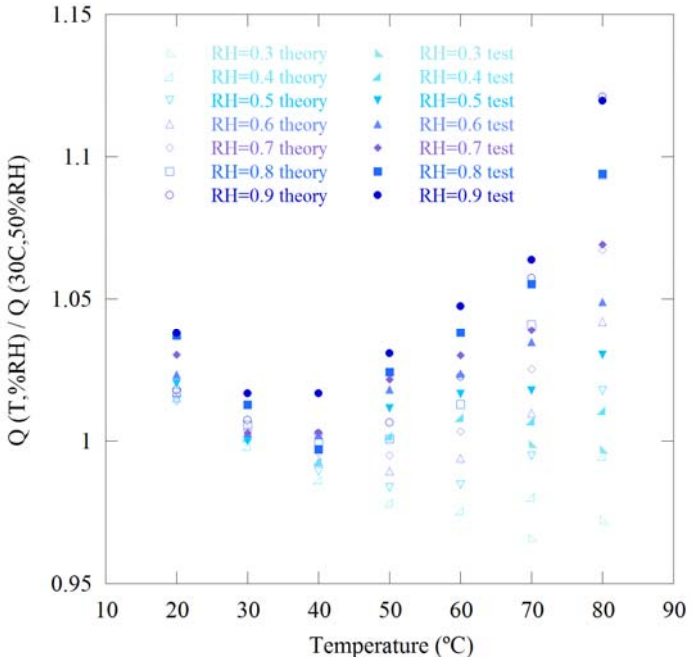

Figure 38: Relative change in quality factor Q with respect to 30°C, 50%RH, as a function of T and RH for a 25-µm thick resonator (Type 1, 2.5º-finger overlap). Empty symbols indicate theoretical values for Q, assuming the environmental effect on Q_{sq} is a function of $[\mu\rho]^{-1/2}$.

3.2.1.3. Equations for Stress Calculations

To summarize the general equation used to calculate the stress amplitude is as follows:

$$\sigma_{\max}(GPa) = 97.2 \times \left(\frac{\Theta}{V_{in}^{\,2}}\right)\Bigg|_{linear} \times V_{in}^{\,2} \times \frac{V_{meas}}{V_{linear}} \times \frac{Q(T,\%RH)}{Q(30^{o}C,50\%RH)} \quad (25)$$

This expression takes into account the FE stress calibration, the optical calibration, the electrical calibration ($\frac{V_{meas}}{V_{linear}}=1$ for HCF testing and $\frac{V_{meas}}{V_{linear}}<1$ for LCF testing since the low-voltage resonant frequency does not match the high-voltage one). The optical calibration being time-consuming, some of the resonators were not calibrated. However,

the value $\left(\frac{\Theta}{V_{in}^{2}}\right)\Big|_{linear}$ is theoretically identical for each resonator of the same type. The average value of the optical calibration for this type of resonator is therefore used for the non-calibrated resonators. Nevertheless the standard deviation of this value adds up on the standard deviation of the total stress calibration, which decreases the precision of the measure. Finally the influence of the environment on Q (which influences the amplitude of rotation) is added. The applied methodology of this testing technique allows estimating the applied stresses with a precision contained between ±0.06 and ±0.10 GPa for the calibrated resonators, between ±0.12 and ±0.18 GPa for the non-calibrated ones.

3.2.2. Fatigue Results

The fatigue tests described in section 2.4.2 were performed on 20 "40-kHz" specimens in controlled atmosphere 30±0.1ºC, 50±1%RH. In addition, the effects of environment and natural frequency on the fatigue behavior were characterized by testing 18 "40-kHz" specimens at 80±0.1ºC, 90±1%RH, 12 "40-kHz" at 80±0.1ºC, 30±1%RH and 9 "4-kHz" at 30±0.1ºC, 50±1%RH. The electrical performance and stability of the fatigue characterization structures' resonant frequency was systemically verified prior the effective damage accumulation by testing the specimens at low stress amplitudes in the atmosphere of interest. Virtually no damage was observed during long periods of time (typically ~ one hour) under sweeps and bursts at 1.2 GPa at 30ºC, 50%RH (Type 1-3) or 0.5 GPa at 30ºC, 50%RH (Type 4) and other environments (Type 1-3). For LCF tests a precision of ±250 cycles for fatigue life was achieved in the "40-kHz" range. This life resolution is even as low as ±28 cycles for resonator in the "4-kHz" range, although

noisier and more damped. For HCF tests the precision is lowered to $\pm 6\times10^5$ cycles for fatigue life was achieved in the "40-kHz" range. In addition, the HCF sweeping times for which the stress amplitude is lower than 90% of the maximum value are subtracted from the total fatigue life. This life resolution is $\pm 6.7\times10^4$ cycles for resonator in the "4-kHz" range. Resolutions up to 0.01 and 0.05 Hz in terms of resonant frequency were observed respectively in the"40-kHz" and "4-kHz" range.

3.2.2.1. S-N Curves

The stress-life data obtained for 10-μm thick SCSi fatigue structures are shown in Figure 39. The specimens experienced fatigue failure under fully-reversed, cyclic stresses. Certain of the represented specimens were interrupted prior to fatigue failure on purpose, usually after $\sim10^{10}$ cycles ("run-out" tests, represented with arrows in Figure 39). The fatigue life of "40-kHz" specimens, N_f, in 30ºC, 50%RH was increased from 6.0×10^2 to 6.2×10^9 cycles as the applied stress amplitude was reduced from 3.2 to 2.3 GPa. These results are qualitatively consistent with other stress-life fatigue curves for microscale SCSi obtained by Pierron in 30ºC, 50%RH [34], Muhlstein in room temperature air at 50±2%RH [32], Sundarajan [42] and Namazu [33, 41] in room temperature (see 1.2.2). As observed, delayed failure due to cyclic loading occurred for stress amplitude as low as 65% of the Si thin films low-cycle fatigue strength. From a low-cycle fatigue point of view ($N_f < 5\times10^6$), the applied stresses ranged between 3.3 and 2.8 GPa resulting in fatigue lives between 6.0×10^2 to 2.8×10^6 cycles. However, the interpretation of one isolated stress-life curve is made quite difficult because of a large scatter in fatigue life. This significant life variability at a given stress is inherent to brittle material such as SCSi, and its scattered initial population of defects.

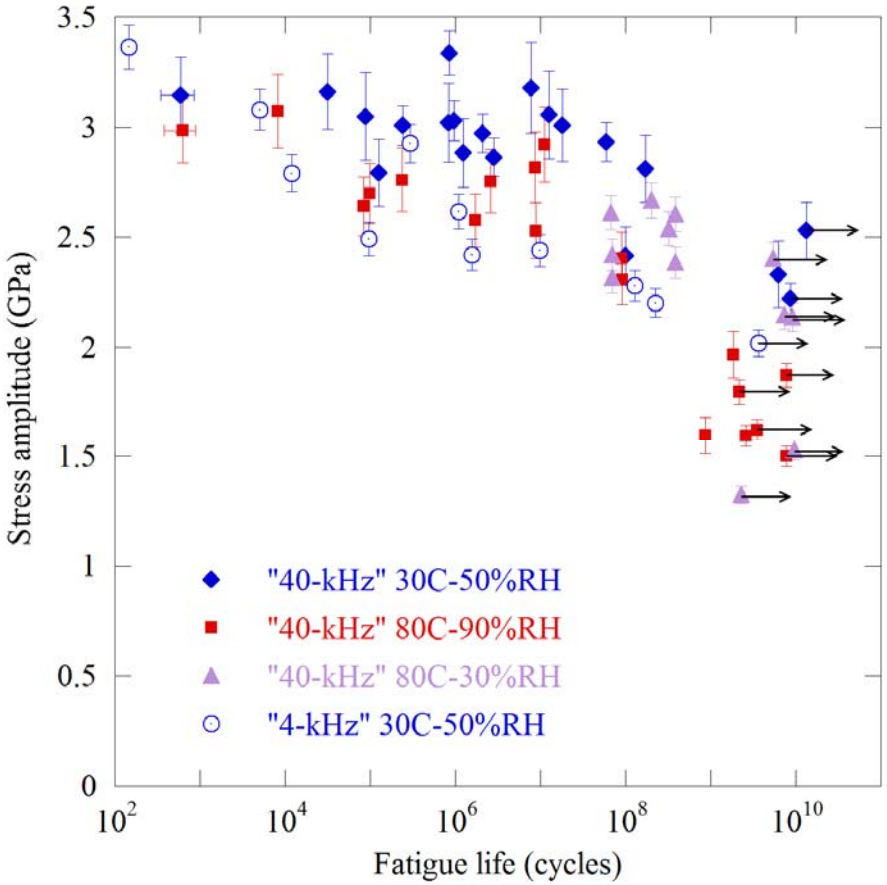

Figure 39: Stress-life (S-N) curve of 4-kHz and 40-kHz resonators in various environments. The arrows indicate run out tests.

Comparison of the S-N curves generated at 30ºC, 50%RH, 80ºC, 30%RH, and 80ºC, 90%RH with the "40-kHz" devices revealed a significant influence of the environment on the fatigue properties. Fatigue lives are shorter in harsh environments for identical stresses. At 80ºC, 90%RH, N_f was increased from 6.3×10^2 to 3.2×10^9 cycles as the applied stress amplitude was reduced from 3.0 to 1.6 GPa. In the low-cycle fatigue range the applied stresses ranged between 3.1 and 2.6 GPa resulting in low-cycle fatigue lives between 6.3×10^2 to 2.6×10^6 cycles. At 80ºC, 30%RH, N_f was increased from 8.4×10^7 to 1.1×10^{11} cycles as the applied stress amplitude was reduced from 2.6 to 2.1 GPa. The observed detrimental effect of the environment, although less important, was similar to the result of exposure at 80ºC, 90%RH.

Concerning the resonant frequency study, the "4-kHz" specimens were tested at 30ºC, 50%RH. As opposed to previous studies from Namazu *et al.* [33, 41] frequency effect is here observed as an increase in fatigue life with increasing testing frequency. The fatigue life was increased from 1.2×10^4 to 2.2×10^8 cycles as the applied stress amplitude was reduced from 2.8 to 2.2 GPa. However fatigue failure in the low-cycle range occurred for stresses as low as 2.5 GPa for "4-kHz" range specimens. For such a stress fatigue lives spanned from 9.7×10^4 to 9.8×10^6 cycles. In contrast, fatigue lives ranging from 8.8×10^4 and 5.9×10^7 cycles were observed for a stress of amplitude as high as 3.0 GPa for the "40-kHz" range specimens.

3.2.2.2. Resonant Frequency Evolution

The significant influence of environment and frequency is also revealed with the monitoring of the resonant frequency evolution for each fatigue test. As described in 2.4.2, f_0 is measured by sweeping over a frequency range. Figure 40 shows a representative sweep curve used to determine f_0. The curve is fitted with a second-order polynomial and the abscissa at the fit maximum deliver the measured f_0 (see Figure 40). The experimental setup allows very precise determination of f_0 for the fatigue devices. A typical standard deviation for the determination of f_0 is ~0.01 Hz, representing 0.25 ppm of the initial value.

Figure 41 and Figure 42 show two typical curves for the resonant frequency evolution, representing two extreme cases: LCF in a mild environment (Figure 41) and VHCF in harsh environment (Figure 42). As seen in Figure 41 the stability of f_0 was first verified during at least half an hour under low stress value. Initially, the specimen is driven at low stress to check the device stability (~1.4 GPa for this example at 30ºC,

50%RH). Upon application of large stress bursts (~3 GPa for the example), f_0 is observed to decrease monotonically. Thus any detected change in f_0 can be associated with a change in stiffness caused by fatigue damage accumulation. Interestingly enough, f_0 decreases after the very first burst of cycles at high stress, suggesting that surface cracks may already be present and grow in a subcritical manner under large cyclic stress. Figure 42 represents only the f_0 evolution of a very high-cycle fatigue test, without the stability check that appears in Figure 41. This testing structure was fatigued at 80ºC, 90%RH under 1.9 GPa. We observe also a decrease in f_0 from the first cycles at high stress. This example features also a monotonic resonant frequency decrease, although different behaviors were observed for other HCF/VHCF tests. Accelerating or decelerating decrease rates have indeed been observed in the different environments.

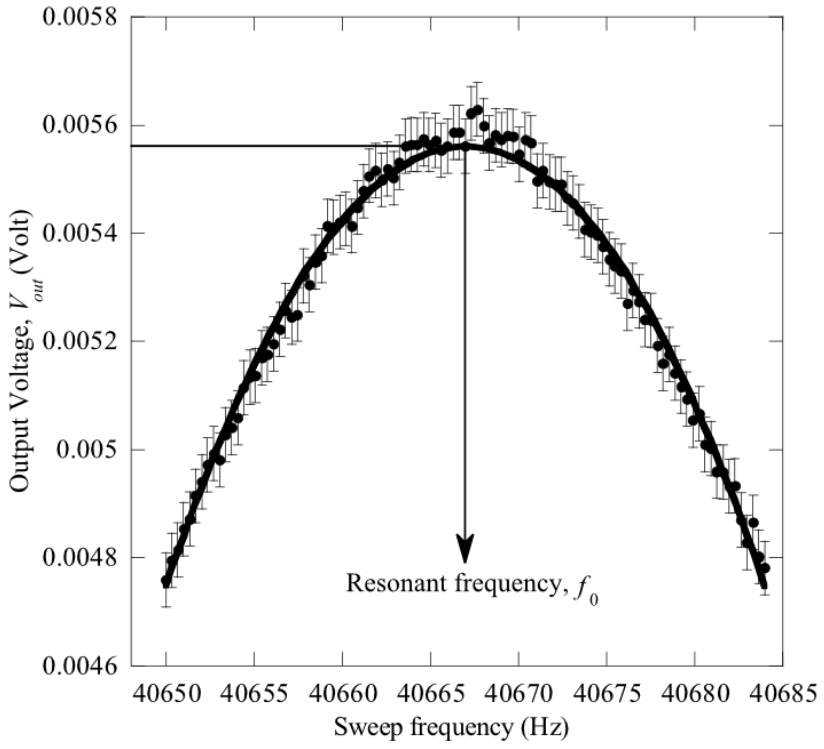

Figure 40: Sweep curve (sensing circuit output voltage, V_{out}, as a function of the applied frequency) used to determine the resonant frequency (f_0) of the fatigue structure.

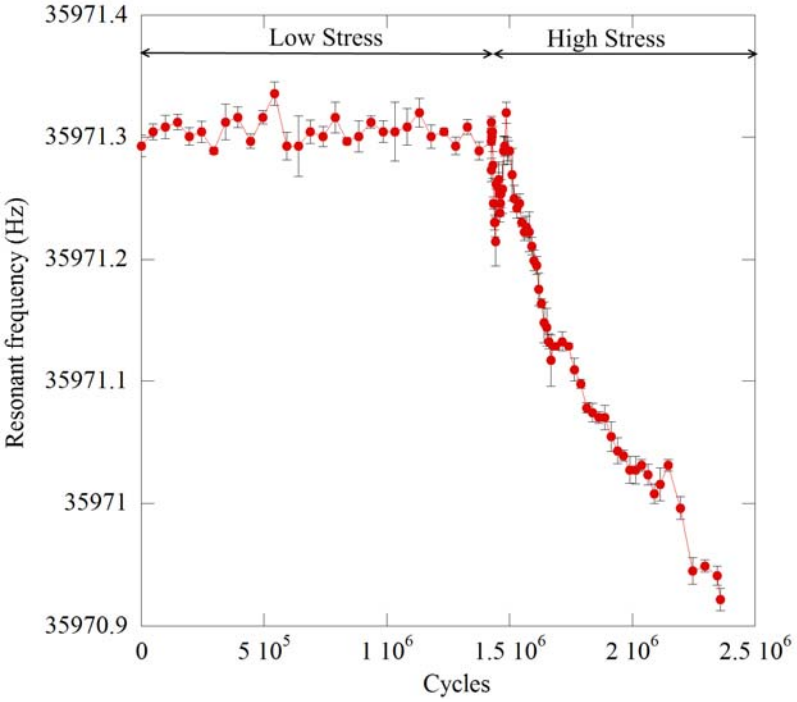

Figure 41: Resonant frequency evolution during a LCF test at 30°C, 50%RH and 3.0 GPa. The first part is carried out at low stress for ~1 hour to verify the device stability. The second part represents the low-cycle fatigue test at high stress.

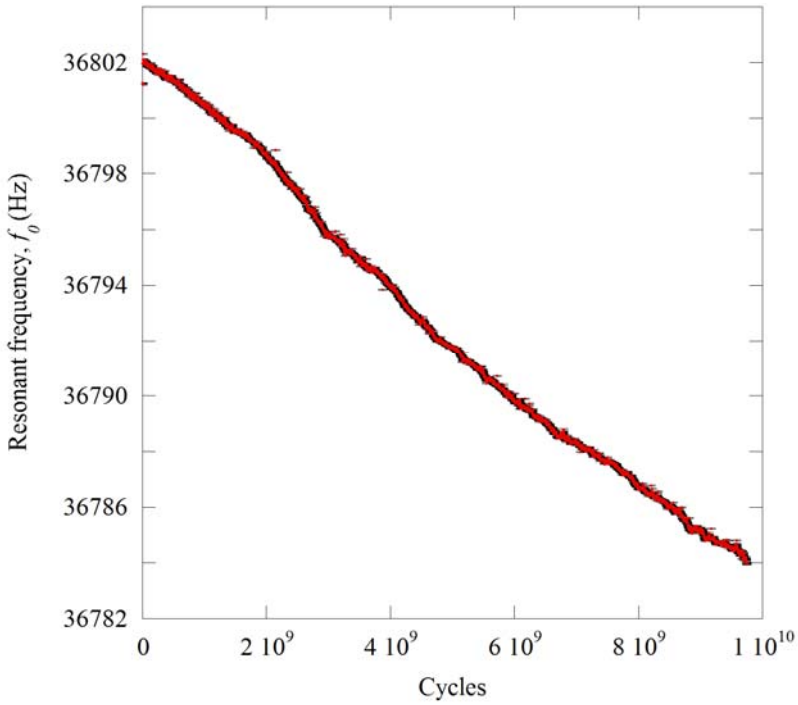

Figure 42: Evolution of f_0 during a VHCF test at 80°C, 90%RH and 1.5 GPa.

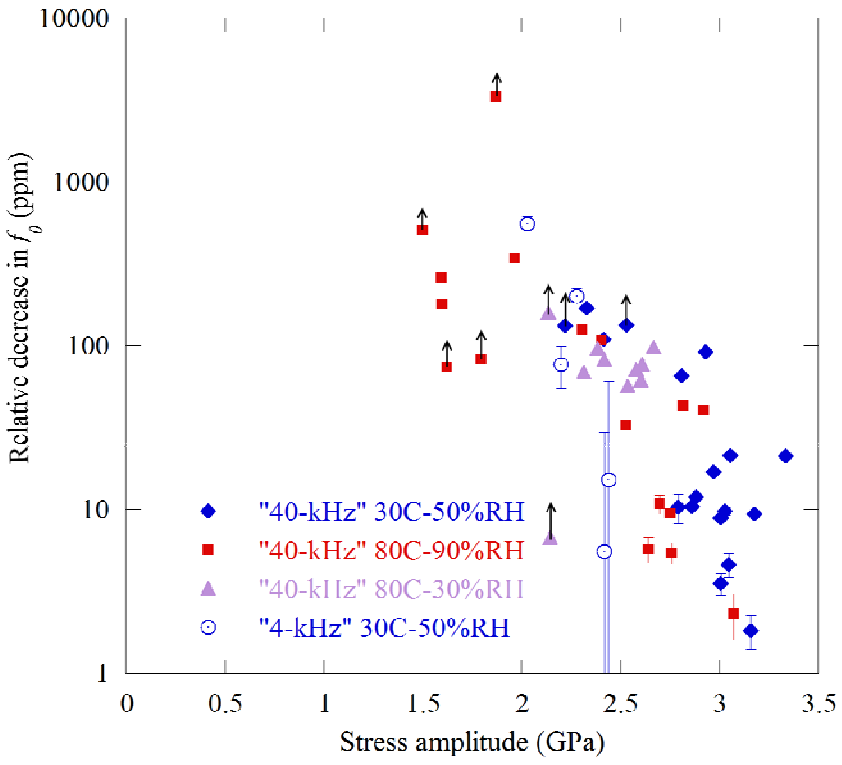

Figure 43: Relative decrease in f_0 as a function of the stress amplitude.

The results of the f_0 evolution for all the fatigue tests are summarized in Figure 43 and Figure 44. Figure 43 describes the total decrease in resonant frequency normalized by the initial value, as a function of applied stress. The relative decreases are used to directly compare the data from the 4-kHz and 40-kHz devices (both types of devices have the same stiffness but different mass), as shown with the following equation (J_θ is constant for a fixed environment):

$$\frac{\Delta f_0}{f_0} = \frac{1}{2}.\frac{\Delta k_\theta}{k_\theta} \tag{26}$$

Figure 43 clearly shows that lower stresses are associated with larger decreases in f_0. This is qualitatively consistent with larger critical crack sizes at lower stresses (~20 nm at 3.2 GPa, and ~90 nm at 1.5 GPa). Therefore, more fatigue damage is needed before failure.

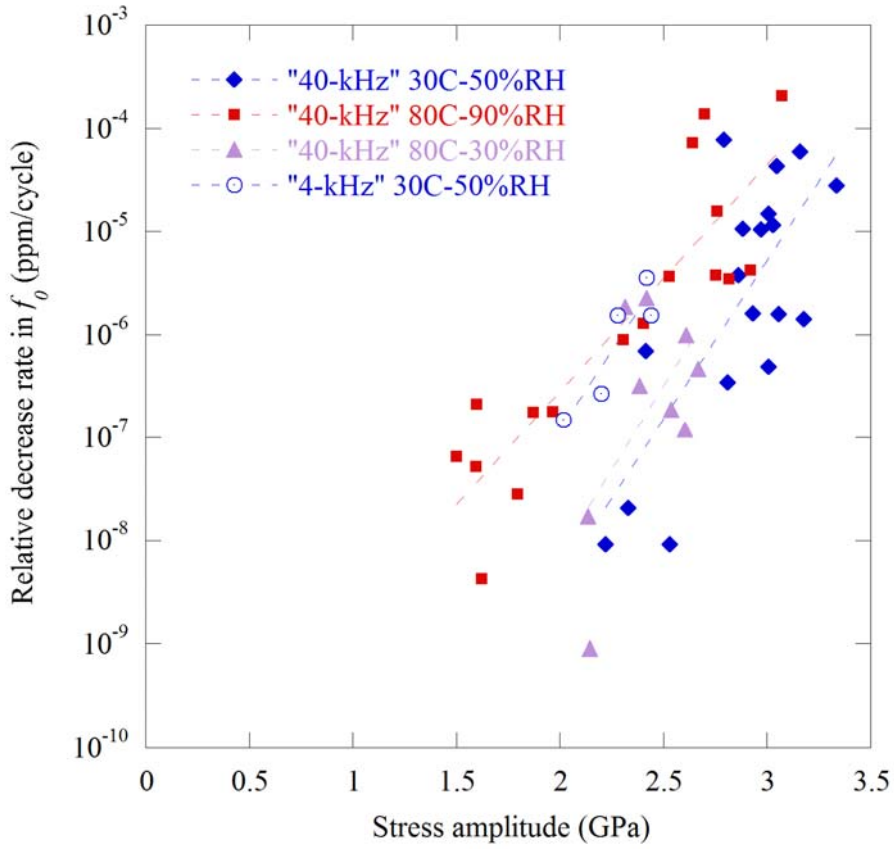

Figure 44: Relative decrease rate in f_0 as a function of the stress amplitude.

Nevertheless an increase of 2 orders in magnitude in damage is observed between 3.2 and 1.5 GPa, which is not consistent with a_c multiplied by ~4. It suggests that the relative decrease in f_0 is related to the amount of crack extension occurring at the surface flaws. Assuming a strength of 3.33 GPa, the amount of crack extension increases by ~2 orders of magnitude, from ~1.5 nm to ~70 nm, when the applied stress decreases from 3.2 to 1.5 GPa. Moreover, in spite of the inherent scatter in initial flaw population for brittle materials, Figure 43 shows also that the total damage accumulation is not significantly affected by environment. The same total damages are observed for mild and harsh environments but Figure 44 shows that the damage accumulation rates are much faster for harsh environments for similar stress amplitude. Last but not least, even though the

"4-kHz" resonators are noisier (thus the larger error bars) the results underline a similar trend: the total decrease in f_0 does not appear to be significantly affected by the resonant frequency. This is consistent with the fact that the same total crack extension has to be experienced to drive the specimen to fatigue failure.

Figure 44 characterizes the damage accumulation rates represented by the relative decrease rates in resonant frequency, $df/dN.1/f_0$, for the different conditions, as a function of the applied stress amplitude. The decrease rate of f_0 can be used as a metric for the fatigue degradation rate. It is calculated using a linear fit for the evolution of f_0 with respect to cycles (see Figure 41 and Figure 42). Figure 44 highlights the critical influence of stress in the fatigue damage accumulation rate, with over 4 orders of magnitude difference between 2.2 and 3.2 GPa (from 5.9×10^{-9} to 6.0×10^{-5} ppm/cycle). It is also apparent that relative decrease rates are significantly higher in harsher environments for HCF and even more for VHCF data. At 2.2-2.3 GPa, the relative decrease rates in f_0 are more than one order of magnitude higher in 80ºC, 90%RH air (8.9×10^{-7} ppm/cycle at 2.3 GPa) than in 30ºC, 50%RH air (2.1×10^{-8} ppm/cycle at 2.3 GPa).

However, the relative decrease rates in f_0 are only slightly higher in 80ºC, 30%RH air (1.1×10^{-8} ppm/cycle at 2.1 GPa) than in 30ºC, 50%RH air (5.9×10^{-9} ppm/cycle at 2.2 GPa), suggesting that the humidity has a more pronounced role than temperature in the fatigue degradation behavior in the HCF/VHCF regime. In contrast, resonant frequency decrease rates were observed to be only slightly higher in harsher environments in the LCF regime. For instance relative decrease rates in f_0 of 1.4×10^{-4} ppm/cycle at 2.7 GPa were observed in 80ºC, 90%RH air while being measured at 7.8×10^{-8} ppm/cycle in 30ºC, 50%RH air at 2.8 GPa.

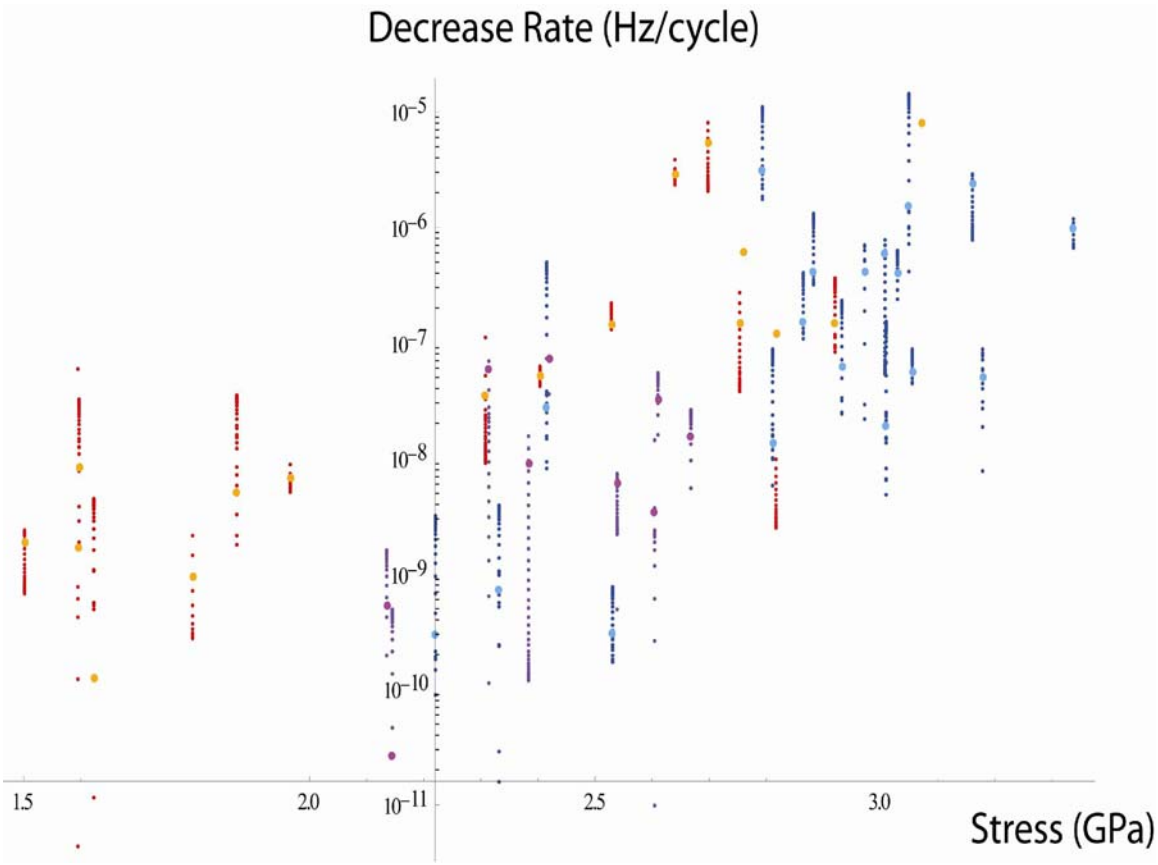

Figure 45: Decrease rate in f_0 as a function of the stress amplitude. This study represents the rates calculated with linear fits as well as the value of these decrease rates sampled logarithmically. Red and orange data corresponds to 80ºC, 90%RH. Blue colored indicators represents 30ºC, 50%RH data and purple colored ones stand for 80ºC, 30%RH.

It is also observed that lower applied frequency results in significantly higher relative decrease rates for similar stresses. The "4-kHz" specimens under 30ºC, 50%RH experienced relative decrease rates between 8.1×10^{-8} to 3.6×10^{-6} ppm/cycle as stresses increased from 2.0 to 2.4 GPa which is one to two order higher than "40-kHz" specimens.

In the low-cycle fatigue range ($N_f < 5.10^6$ cycles), f_0 was observed to decrease monotonically during the test, suggesting progressive damage accumulation. Regarding the shape of the curve f_0–N, every LCF test revealed a constant resonant frequency decrease rate throughout the fatigue life, regardless of the environmental conditions.

Therefore higher temperature and relative humidity did not seem to affect the evolution of the damage accumulation for such short lives. Moreover, no real trend for the shape of the f_0–N evolution has been detected in VHCF, for any testing conditions. Indeed, constant, decelerating or accelerating decrease rates have all been observed so far.

Since the evolution of f_0 was observed to be mostly linear in LCF, the decrease rates were calculated by fitting linearly the resonant frequency evolution through the fatigue test. The fitting coefficient was superior to 0.9 for most of the curves which reveals a good approximation of decrease in f_0 over the LCF life. On the other hand some high-cycle fatigue tests revealed variations of decrease rates while fatigued. The resulting errors in decrease rate were estimated inferior to 50% for lives superior to tens of millions cycles. Figure 45 shows that this is a rather good approximation. The decrease rates were calculated by fitting the frequency evolution with a polynomial function (between 1^{st} and 6^{th} orders). The differential is derived from the fit. The decrease rates were sampled every $10^{0.5\times i}$ (i=4,..,22) and appear as red, violet and dark blue bands that encompass the linear fit data (orange, purple an light blue dots). Figure 44 gives nonetheless reliable and more readable representations of the relative decrease rates in every tested condition.

3.3. *Fractography*

Scanning electron microscopy (SEM) imaging of failed specimens was performed using a LEO 1530. Representative fracture surfaces of different fatigued specimens were analyzed, with the intent to locate the failure origin and the extent of localization through the thickness. The microscopy fracture surfaces of relatively short-life specimens are presented in Figure 46 to Figure 48. Despite the apparent melted parts of two of the

fracture surface due to electrical arcing occurring after failure, unique features associated with fatigue damage accumulation are accounted for. Figure 46 and Figure 47 show respectively the fracture surface of a "40-kHz"-range specimen failed at 3.0±0.1 GPa after 2.07×10^6 effective cycles in a 30°C, 50%RH environment and one at 2.5±0.1 GPa after 8.78×10^6 effective cycles in a 80°C, 90%RH. Figure 48 shows the fracture surface of a "4-kHz"-range specimen failed at 2.5±0.1 GPa after 1.55×10^6 cycles in 30°C, 50%RH. The scalloping and curtaining previously mentioned (see Section 2.2.2) can be seen and marks the sidewalls of the notch surface.

Muhlstein [32] as well as Pierron [34] reported that a localized fracture origin at the notch was present for very high-cycle fatigue (expressed by a smooth mirror-like region). Here we report the observation of smooth, semi-elliptical mirror-like region with similar dimensions for each of the testing conditions. The approximate depth of this region is about 350 nm for the three conditions although the applied stresses were not identical (Pierron reported approximately 1 μm for 1.56×10^9 cycles at 2.55 GPa). On the first micrograph Walner lines and steps appear clearly, indicated by the red arrow in Figure 46. They characterize unstable crack propagation in the area surrounding the mirror region. These fracture surfaces reveal a highly localized fatigue damage accumulation in the SCSi thin films, suggesting an active fatigue mechanism different from quasi-static failure. For instance Pierron reported an overloaded specimen fracture surface that does not present a mirror region and is characterized by unstable crack propagation [34].

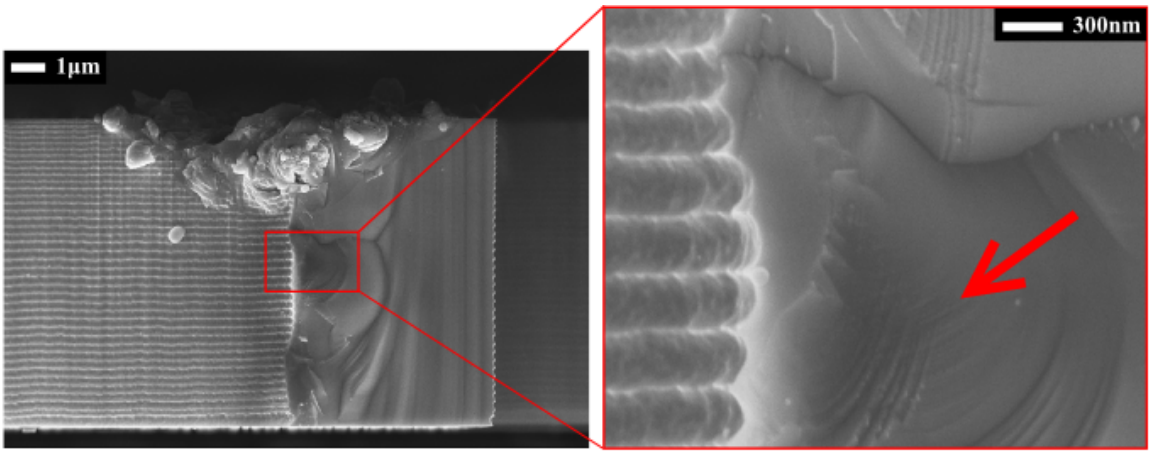

Figure 46: Field emission scanning electron micrograph of a 40-kHz specimen failed at 2.97±0.08 GPa after 2.07×10^6 effective cycles in a 30°C, 50%RH environment.

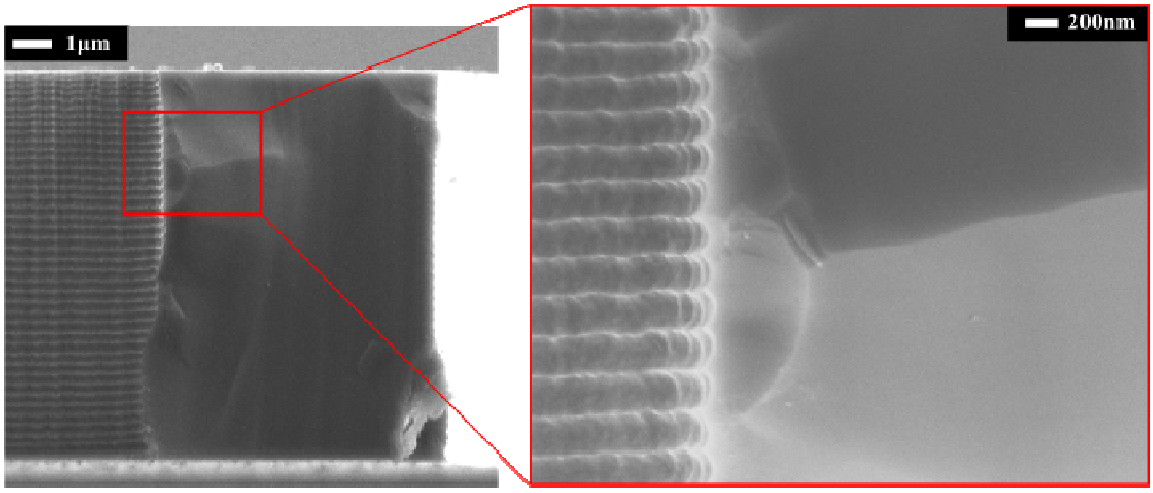

Figure 47: Field emission scanning electron micrograph of a 40-kHz specimen failed at 2.53±0.12 GPa after 8.78×10^6 effective cycles in a 80°C, 90%RH environment.

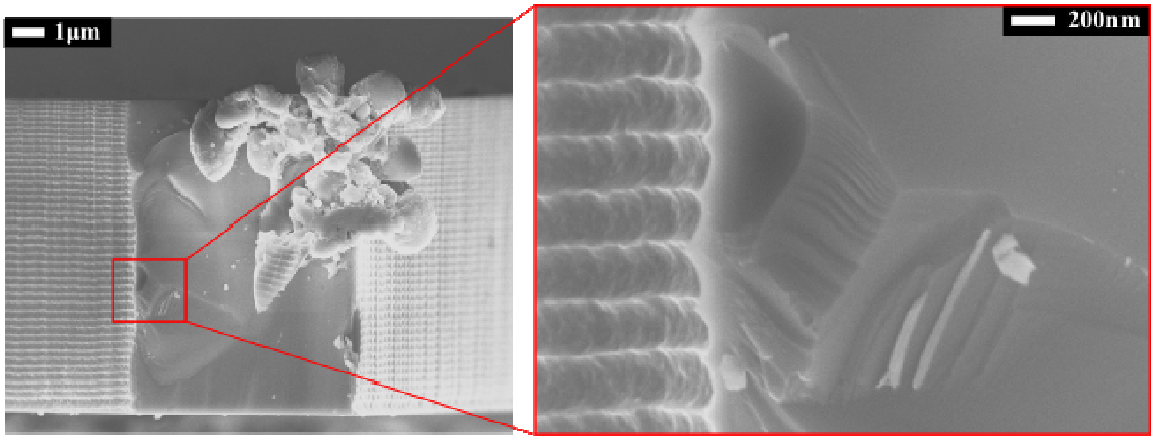

Figure 48: Field emission scanning electron micrograph of a "4-kHz"-range specimen failed at 2.45±0.07 GPa after 1.55×10^6 effective cycles in a 30°C, 50%RH environment.

CHAPTER 4

ANALYSIS OF RESULTS

4.1. *Influence of Environment on Adsorbed Water Layer Thickness*

As seen in section 3.1, the change in adsorbed water layer thickness was calculated as a function of relative humidity (RH) for different temperatures ranging from 20°C to 80°C. The precision of the technique is very good (a 0.01Hz standard deviation causes an error of ±0.013 nm in adsorbed water thickness), however it does not provide absolute values for adsorbed water layer thicknesses. It is therefore useful to compare our data with other quantitative techniques, in light of the multilayer adsorption theory (see section 2.3.3). In the context of fatigue of Si thin films, it is necessary to know the initial surface state, especially adsorbed water layer thickness, for different testing conditions. We compared our data with total reflection-infrared spectroscopy measurements [82] and optical ellipsometry [81]. For reference, Asay *et al.* observed the water adsorption on a hydrophilic silicon oxide surface (SCSi covered with a native oxide) at 20.8 ± 0.5°C. The samples were prepared prior testing by washing with dichloromethane, rinsing with Millipore water, drying with argon and exposing it to UV/0_3 for 30 min. This results in a native oxide surface free of organic contaminant. A thickness decrease of 0.455 nm was reported between 50 and 20%RH as well as an increase of 0.755 nm between 50 and 90%RH [82], assuming one monolayer of adsorbed water is 0.28 nm-thick. Moreover Picard *et al.* observed at 20 ± 0.2ºC a decrease of 0.22 nm between 50 and 10%RH as well as an increase of 0.37 nm between 50 and 75%RH [81]. Their SCSi artifacts were

also cleaned beforehand by rubbing strongly the surfaces by using a special lint-free cloth moistened with a mixture of 50% diethylether and 50% ethanol. This is used to remove hydrocarbon contamination.

Figure 49 compares the average values gathered at 20°C with the data from Picard and Asay. The changes in adsorbed water thickness observed on the fatigue characterization structures are substantially superior to the ones measured by Picard and Asay. It is also worth mentioning that there are some discrepancies between Asay and Picard's results, especially in the low and high humidity regions. It should also be noticed that neither the preparation nor the method of measurement is similar for each of those data, which is the disadvantage of the limited literature on this subject. The initial surface roughness of the artifacts as well possible contaminations of the surfaces could sensitively bias the results.

Although the shape of our curves (see Figure 29 to Figure 31) is qualitatively consistent with the shape of a Type II isotherm, it was not possible to fit them with the BET Eq. (16) (the fit yields $c_B<0$, whereas c_B must be positive; see Eq. (17)). Moreover, the results show effectively an increase of the adsorbed water thickness with increasing RH, but they also express a weak but noticeable influence of the T (see Figure 50). According to Eq. (16) the adsorbed water layer thickness is a function of RH, but also a function of c_B, which depends on T.

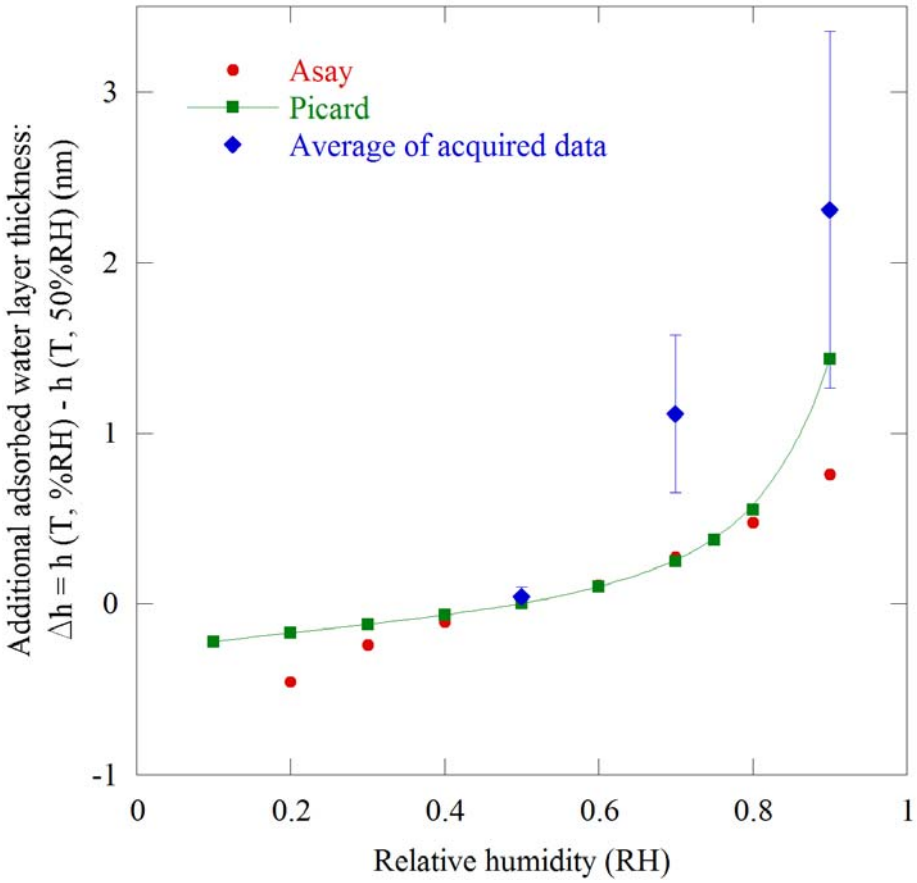

Figure 49: Calculated additional water layer thickness with respect to 50%RH as a function of relative humidity: comparison between Asay' data [82], the BET fit for Picard's data [81] and the average value of the acquired data.

Furthermore, Asay's data could not be fitted by a BET curve for the same reason (c_B<0). Nevertheless, the curve acquired by Picard could be fitted by a Type-II shape isotherm with c_B~5 using:

$$\frac{RH}{h.(1-RH)} = \frac{1}{h_m c_B} + \frac{c_B - 1}{h_m c_B}.RH \qquad (27)$$

However, the derived thickness of one layer of water was 0.178 nm, knowing that the theoretical thickness of a monolayer is 0.28 nm.

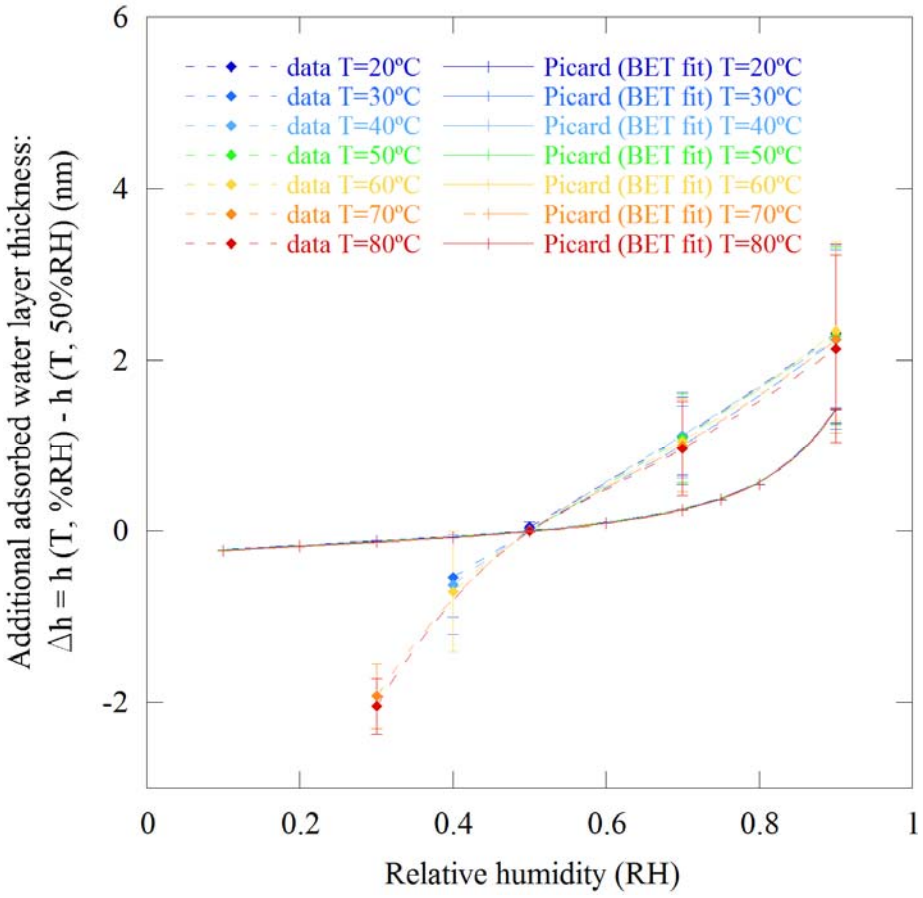

Figure 50: Calculated additional water layer thickness with respect to 50%RH as a function of RH and *T*: comparison of the temperature dependencies of the BET fit of Picard's data [81] and the average value of the acquired data.

Figure 50 reveals a quantification of the influence of *T* on water adsorption on SCSi surfaces (native oxide surface containing varying quantities of contaminants). Using the theoretical BET fit issued from Picard's data (c_B~5), the variation in thickness of adsorbed water was calculated for any *T* and RH humidity state. The activation energy was assumed temperature independent (Brunauer *et al.* [79, 80] underlined that the dependence of c_B on *T* is exponential while the activation energy changes only slightly with *T*). The theoretical variation is expected to be lower than 0.013 nm for different *T* but same RH. In our case, the amplitude of variation (0.18 nm) is lower than the standard

deviation of the measurement. Consequently we can consider that the adsorbed water layer thickness is mainly dependent on the RH and varies very little with *T*. For example, even though the partial pressure of water is equivalent between 60°C, 75%RH and 80°C, 30%RH, the amount of adsorbed water is expected to be significantly lower in the second environmental condition. These results can be used to separate the effect of *T* and RH on the fatigue behavior.

4.2. *Fatigue Mechanisms*

The underlying fatigue mechanism(s) responsible for the observed fatigue behavior of the SCSi thin films are now discussed, based on the observed influence (or lack thereof) of frequency, temperature, and humidity in the LCF ($N_f < 2\times10^6$ cycles) and HCF/VHCF regime. First it is important to emphasize that the interpretation of one isolated stress-life curve should not be overestimated in the case of deep reactive-ion etched (DRIE) SCSi thin films. The "low-cycle" stress-life curve observed in 3.2.2.1 reveals a very slight decrease trend that is overshadowed by the brittleness of SCSi. Various testing conditions overlap (due to the standard deviation of the stress measurement) and the scatter in the intrinsic flaw population of the DRIE process causes a large fatigue life scatter. A significant life variability at a given stress amplitude is a direct consequence of a scattered initial population of defects. Nevertheless, clear trends in the fatigue properties were observed as a function of stress, frequency and environment.

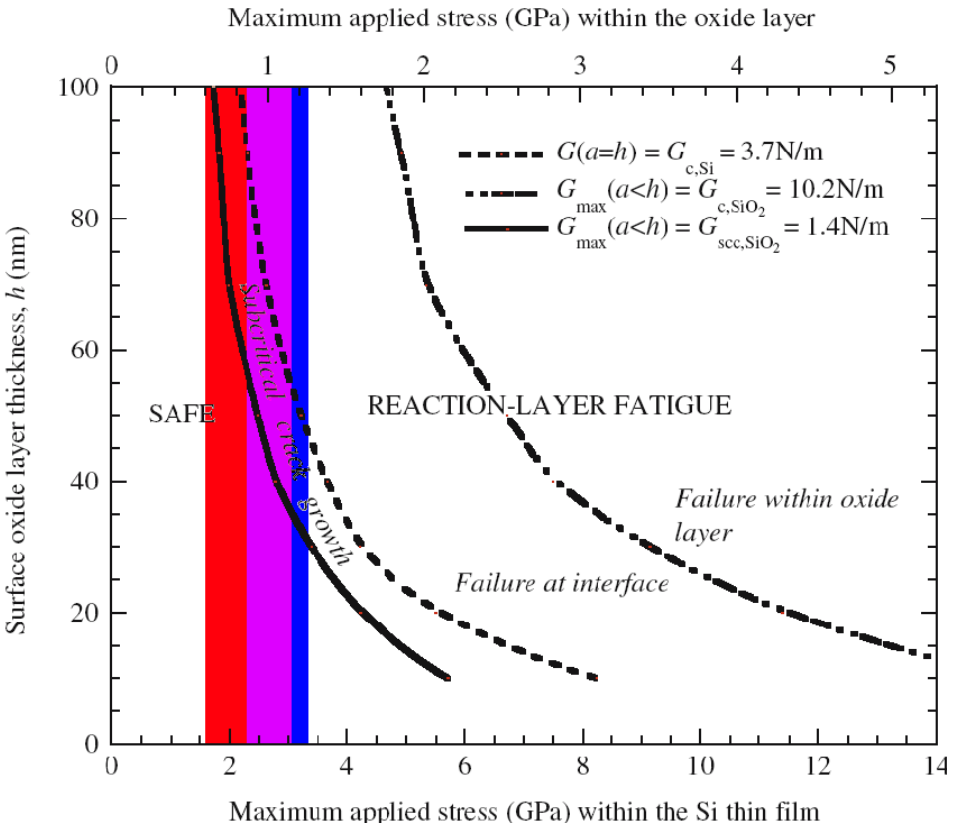

Figure 51: Failure map for a Si thin film with oxide surface layer of thickness h [70].

4.2.1. Influence of Environment

The fatigue damage accumulation was dramatically accelerated in harsh environments in the HCF/VHCF regime. Increased damage accumulation rates were unambiguously observed at 80°C, 90%RH compared to 30°C, 50%RH. Additionally, significantly increased damage accumulation rates were observed at 80°C, 90%RH compared to 80°C, 30%RH. Therefore it seems that the humidity plays a stronger role than temperature in the fatigue process. In contrast, damage accumulation rates were only slightly increased at 80°C, 90%RH compared to 30°C, 50%RH in the LCF range, indicating that a different mechanism may be activated in the presence of applied stresses approaching the material's strength.

The dependence of the damage accumulation rate with the environment (especially humidity) is a strong piece of evidence supporting the reaction-layer mechanism postulated by Muhlstein *et al.* [56]. Along with the presence of thickened oxides after cycling observed by Muhlstein [56] and Budnitzki [62] accelerated fatigue damage accumulation with increased humidity levels is more consistent with a surface degradation mechanism rather than with a truly mechanical process. Consequently the reaction-layer mechanism agrees well with these observations in the HCF/VHCF range. Indeed a more humid environment may enhance the kinetics of stress assisted oxidation by increasing the adsorbed water layer thickness. Muhlstein *et al.* [83] and Pierron *et al.* [70] developed a failure map seen in Figure 51 showing the stress and oxide thickness conditions necessary for activating the reaction-layer mechanism. In the stress range where fatigue failure was observed at 30°C, 50%RH (represented by blue and purple bands), surface oxide layer thicknesses of 30 to 55 nm are needed to activate the reaction-layer fatigue mechanism. Thicknesses between 35 and 100 nm would be necessary in the stress range corresponding to the 80°C, 90%RH observations (red and purple bands).

In another study on polysilicon thin films, oxide thickening was observed up to 20 nm overall and up to 50 nm in localized areas. These thicknesses were observed after tens of hours of cyclic loading [62]. It is therefore questionable whether significant oxide thickening can occur within less than one minute, corresponding to fatigue lives in the LCF regime (2.10^6 cycles are reached in 50 s at 40 kHz). Figure 51 shows that SiO_2 layers thicker than 30-35 nm are necessary to activate the mechanism for stresses corresponding to the LCF regime. However, the typical native oxide thickness for SCSi is only 2-3 nm. Thicker native oxides have been observed with the PolyMUMPs process

(polysilicon), a result attributed to galvanic effects between adjacent gold and Si layers during the sacrificial release in hydrofluoric acid (HF) [84]. However, no galvanic effect is expected to occur for the SOIMUMPs devices. It seems therefore unlikely that such an oxide thickness can develop in the LCF range associated with short time to failure. Another mechanistic approach will be treated in section 4.3.

4.2.2. Influence of Frequency

Contrary to previous studies, we report observations of a frequency-dependence on the number of cycles to failure in the HCF/VHCF regime. However the poor precision in resonant frequency measurement of the "4-kHz" resonators due to lower Q values and the large scatter in fatigue life prevent any conclusive comparison in the LCF regime. The observed frequency dependence is confirmed with two independent experimental results: the influence of frequency on fatigue life, N_f, and on and the degradation rates. For comparison, other studies only relied on N_f. They were based on externally actuated devices, which can cause alignment issues. Finally they were only looking at small frequency range (10 to 450 Hz for Namazu *et al.* [33, 41]). The frequency effects (smaller fatigue life and faster degradation rate with increasing frequency from 4 to 40 kHz) clearly show that the mechanism acting in the HCF/VHCF is not purely mechanical (in which case no frequency effect would be observed). They also appear to be consistent with the reaction-layer fatigue mechanism. It should be noted that stress corrosion cracking (SCC) would also present such frequency effects, however many experimental and atomistic studies deny its existence for Si in air or water [15, 22, 50].

4.3. *Fracture Mechanics Analysis: Investigation of Time-dependent Subcritical Cracking for the LCF Regime*

As mentioned in the introduction Kenny, Dauskardt and coworkers [15, 22] used static crack growth tests to develop crack velocity vs. applied stress intensity factor (K_I) curves. The results suggested that subcritical cracking occurs for $0.9\ K_{Ic} < K_I < 0.98\ K_{Ic}$, with a crack-growth rate exponent, n, higher than 100. That study concluded that stress corrosion cracking in Si does not occur in air; nevertheless, time-dependent crack growth under static loading was observed for large K_I values (>90% of fracture toughness). Although the underlying mechanism is obscure, it is interesting to study whether such subcritical crack growth in SCSi can account for the present results (*S-N* curves, resonant frequency decrease and decrease rates) in the LCF regime.

For mechanisms such as subcritical crack growth, the crack velocity during crack propagation depends primarily in the stress intensity factor, K_I. The dependence relation is frequently expressed as follows:

$$\frac{da}{dt} = A.K_I^{\ n} \tag{28}$$

where A and n are system constants environmentally dependent. A can be calculated using the fracture toughness, K_{IC}, and the initial flaw size, a_i.

This analysis is based on several additional assumptions. We assume that only one subcritical crack is responsible for the observed resonant frequency decrease. This simulation accounts for the influence of a semi-elliptical crack (localized along the thickness). A through thickness crack (2-D case) is also considered as an upper limit. Additionally the crack growth rate expected under cyclic loading is evaluated, assuming it is solely dependent on the static slow crack growth parameters. The fracture toughness

of SCSi along (100) is taken equal to 0.85 MPa.m$^{-1/2}$ (see 1.1.2). The resonant frequency is fixed to 40 kHz. As a general property, the stress intensity factor is expressed by:

$$K_I = Y\sigma\sqrt{a} \tag{29}$$

where σ is the applied stress, a is the crack size and Y is a geometrical factor such as:

$$Y = 1.12\sqrt{\frac{\pi}{Q}} \tag{30}$$

with $Q = 1 + 1.464\left(\frac{a}{c}\right)^{1.65}$ in 3-D and $Q = 1$ in 2-D. The shape factor, usually known as c/a, designates the ratio of the semi-major axis over the semi-minor axis.

The first step of the study is to define the relations between stress and fatigue life at 30°C, 50%RH and 80°C, 90%RH. As the study is focused on the LCF case, the following equations reflect only the values gathered under 2×10^6 cycles:

$$\sigma_{30°C,50\%RH} = -2.359\times10^{-2}.\log(N_f) + 3.342 \tag{31}$$

$$\sigma_{80°C,90\%RH} = -4.706\times10^{-2}.\log(N_f) + 3.320 \tag{32}$$

We assume that an initial flaw already exists at the surface. As a consequence the fatigue life accounts only for the propagation of the crack. Knowing that the initial crack size, a_i, has to be equal to the critical crack size, a_c, when K_{Ii}=K_{IC} and if the fracture strength, σ_f, is assumed equal to 3.33 GPa (see Eq. (31) and (32)), a_i can be derived from:

$$a_i = \left(\frac{K_{Ii}}{Y\sigma}\right)^2 \tag{33}$$

Its dimension was therefore estimated at 18.2 nm for c/a=5, and 16.5 nm for the 2D case. Then, using this value and the linear fits of the stress-life data, we can derive n and A which gives a constant a_i as a function of N_f as described by Evans and Fuller [85]:

$$K_{Ii} = \left[t_s\frac{(n-2)}{2}.AY^2\sigma^2\right]^{\frac{1}{2-n}} \tag{34}$$

where the static time to failure, t_s, is equal to $t_s=N_f.g/f$ and the g-factor for a tension/compression sinusoidal stress wave with zero average stress is as follows:

$$g = \left[\sqrt{2\pi n}.\left(1 + \frac{1}{4n} + \frac{1}{32n^2} - \frac{139}{1920n^3} - \frac{5711}{30720n^4} \right) \right]^{-1} \tag{35}$$

Practically, the exponent n is determined such that the initial crack size a_i is independent on the fatigue life (which makes the study logical), and A is derived by the previously determined value of a_i. 128 and 56.5 were the n values calculated at 30°C, 50%RH and 80°C, 90%RH respectively. For comparison, Kenny, Dauskardt and coworkers measured n values ~ 110 for a ramped loading and displacement rate condition and ~ 600 for constant loading. 1.26×10^5 and 1.18×10^5 (for c/a=5), 1.37 and 1.25 (in the 2-D case) were the calculated values for A at 30°C, 50%RH and 80°C, 90%RH respectively.

The second part of the analysis focuses on solving the equation giving the fatigue life N_f when the crack size reaches its critical value for varying stresses [85]:

$$a_c = \left[a_i^{\left(1-\frac{n}{2}\right)} + \frac{Y^n A \sigma^n}{f}.N_f.\left(1-\frac{n}{2}\right) \right]^{\frac{1}{\left(1-\frac{n}{2}\right)}} \tag{36}$$

As a consequence, the fatigue life, the crack extension (a_c-a_i), the ratio K_{Ii}/K_{IC} and the static time to failure are deduced for both cases as a function of the stress amplitude. Figure 52 represents the fatigue lives as a function of the ratio K_{Ii}/K_{IC}. Both 3-D (c/a=5) and 2-D case are represented, even though the shape factor did not have a significant influence. Simulated and measured values match up to 10^7 cycles both for 30°C, 50%RH and 80°C, 90%RH. Above 10^7 cycles, the present analysis significantly overestimates the fatigue life, meaning another fatigue mechanism may take place in the HCF/VHCF regime (such as reaction-layer fatigue). A considerable influence of a_i is nonetheless observed, reducing N_f by 2 to 3 orders of magnitude when increased by only 1.7 nm.

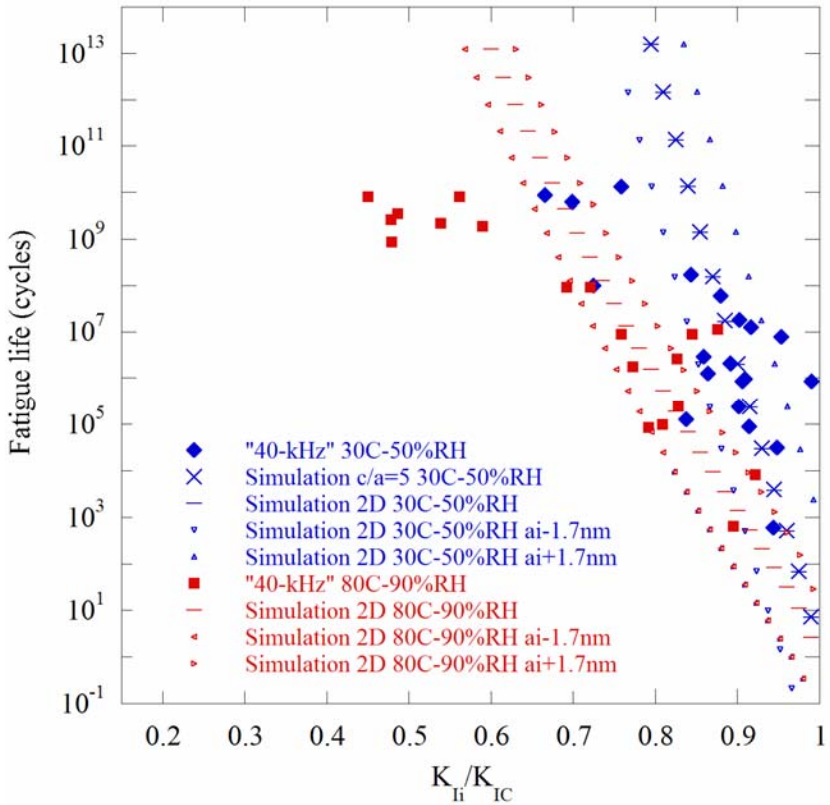

Figure 52: Fatigue lives as a function of the ratio K_{Ii}/K_{IC}. Minuses and crosses represent respectively the extreme 2-D case (through-thickness cracking) and the 3-D case (c/a=5).

In order to compare experimental data and calculated results, a 2-D as well as a 3-D finite element model has been developed by Budnitzki [62]. These resonant frequency modal analyses implement semi-elliptical surface cracks and extract values with the PCG Lanczos method. The chosen material was linear-isotropic polysilicon (E=163 GPa and ν=0.23). The model was meshed with 20-node brick elements (SOLID186). The error provoked by the use of an isotropic model is assumed acceptable. Change in resonant frequency calculations were carried out for shape factors ranging between 1 and 5. The simpler 2-D model was implemented as a limiting case representing a through thickness crack. Figure 53 represents the absolute value of the change in resonant frequency of a "40-kHz" structure as a function of the crack size for various shape factors.

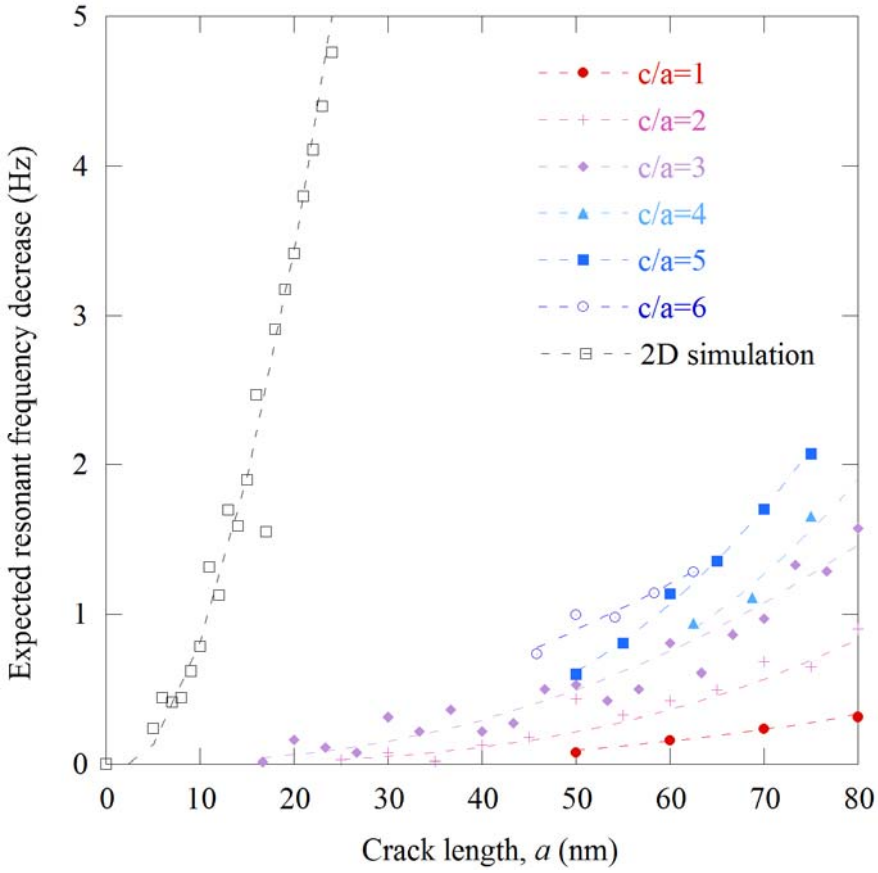

Figure 53: Absolute value of the calculated change in resonant frequency due to semi-elliptical and through-thickness cracks at the notch root of a "40-kHz" structure.

Knowing the crack extension (a_c-a_i) for each stress, an expected change in resonant frequency can be calculated. The results for a shape factor equal to 5 and a through thickness crack are represented in Figure 54. The 2-D simulation being too extreme, the results do not fit both LCF and HCF range data. This result excludes the possibility of a subcritical crack growing through the entire thickness. In addition, the 3-D simulation f_0 decreases account for slightly lower values gathered experimentally, the LCF data standing much closer than the HCF results. To summarize, the principal result is that the slope of simulated and measured curve is very different. The simulation may be able to fit the LCF regime with a more realistic crack density but not the HCF/VHCF

regime. Other fatigue mechanism may be active in the latter regime, such as reaction-layer fatigue.

Resonant frequency decrease rates are calculated by dividing the change in frequency by the fatigue life (this agrees with the linear fits used experimentally). The results for a shape factor equal to 5 and a through thickness crack are represented in Figure 55. The 2-D simulation being too extreme, the results do not fit both LCF and HCF range data. The 3-D results lie close to the observations in the LCF range, but do not fit the HCF data. However, f_0 decrease rates are at least half an order higher than the values calculated with the subcritical crack growth simulation. The same conclusions as in the previous paragraph apply.

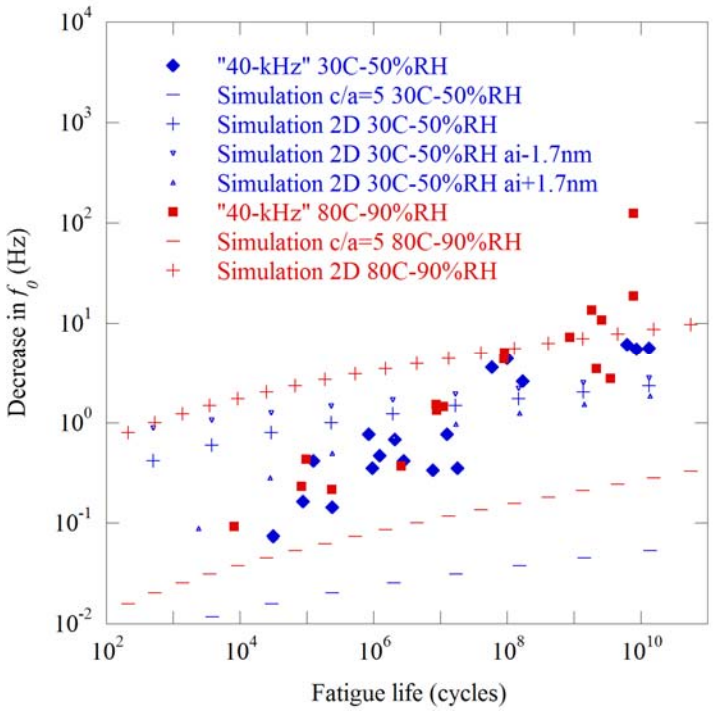

Figure 54: Measured and simulated resonant frequency decrease at 30°C, 50%RH and 80°C, 90%RH as a function of the fatigue life. The pluses represent the extreme case of through thickness crack and the straight marks indicates a more realistic case (c/a=5).

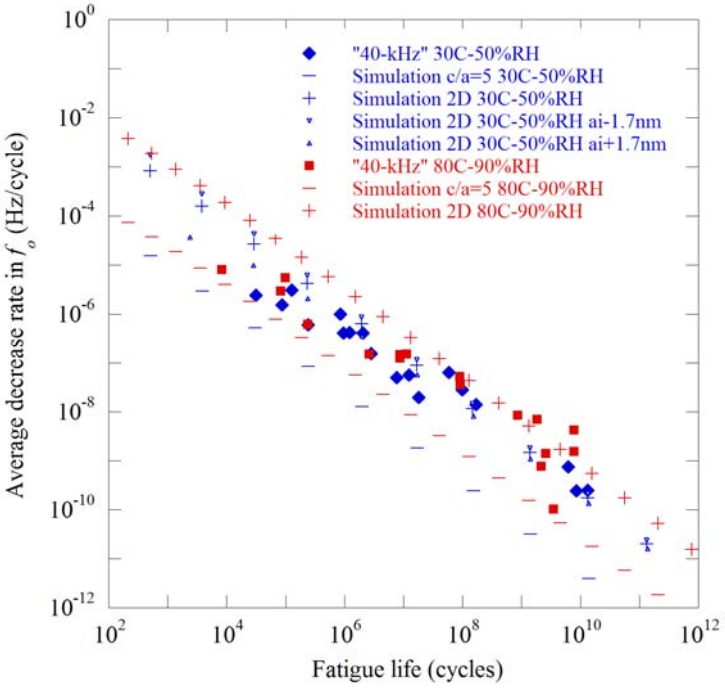

Figure 55: Measured and simulated resonant frequency decrease rate at 30°C, 50%RH and 80°C, 90%RH as a function of the fatigue life.

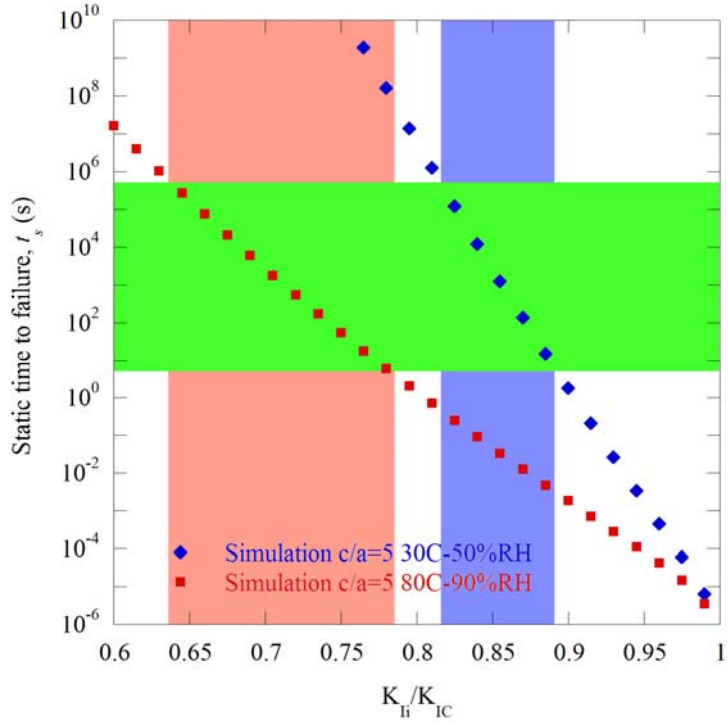

Figure 56: Static time to failure as a function of the ratio K_{Ii}/K_{IC}. The static times to failure that can be experimentally measured are represented in green. The corresponding stress intensity ratio ranges are expressed in blue for 30°C, 50%RH and red for 80°C, 90%RH.

It is important to know whether delayed failure can be experimentally measured under static loading as a result of the subcritical cracking for large K_I/K_{IC} ratios. Such a test could support or rule out this fatigue mechanism. As supported by Figure 56, the analysis reveals that delayed failure under static loading should be observable if subcritical crack growth is in action in the LCF range (static time to failure between 10 seconds and a week). Contradictory observations are reported in the literature. As already mentioned, Kenny, Dauskardt and coworkers suggested subcritical cracking occurs in SCSi for $0.9\ K_{Ic} < K_I < 0.98\ K_{Ic}$. Detailed studies by Kahn *et al.* [50] did not report any observations of such a phenomenon while testing polysilicon thin films under ambient temperature and 90%RH. In contrast, unpublished data by Bagdahn and Sharpe studied polysilicon under static fatigue in ambient air (~25°C, 20-50%RH). They observed static failure in air for K_{Ii}/K_{IC} contained between 0.75 and 0.85. Static time to failure ranged between 10^3 s and two weeks. In water static failure was observed for K_{Ii}/K_{IC} contained between 0.75 and 0.8 with static times to failure ranging between 50 s and three days.

Moreover numerous experimental studies negated the possibility of stress corrosion cracking in SCSi thin films [15, 22, 50]. Based on first principles molecular dynamics simulations, Ciacchi *et al.* [68] have nevertheless proven that tensile strain can enhance the driving force for the dissociative adsorption of water. This suggests that similar reactions could be responsible for environmentally-driven subcritical crack propagation in SCSi. The premature failure under fatigue loading in humid environments could therefore be based on sequential steps of oxide formation and stress-driven corrosion cracking of the oxide layer at the tip of the stable crack. Concordant results

have been published by Belkada *et al.* [67] using a hybrid quantum-mechanical/molecular dynamics simulation code.

To summarize, the results of the fracture mechanics analysis are not conclusive. There is not a very good match with the experimental data and static failure should be observed. Therefore there is no decisive evidence that can reject either a purely mechanical mechanism (described by Kahn *et al.* [29], see 1.2.3) or subcritical crack growth in SCSi itself.

CHAPTER 5

CONCLUSIONS AND DIRECTIONS FOR FUTURE WORK

5.1. *Conclusions*

The present study aimed at further understanding the fatigue mechanisms for micron-scale Si. This study investigated the fatigue behavior of 10-micron-thick SCSi films in different environments (30°C, 50%RH, 80°C, 30%RH and 80°C, 90%RH air) and at different frequencies (4 kHz vs. 40 kHz). The fatigue testing structures were loaded under fully reversed sinusoidal stress with amplitudes ranging between 1.5 and 3.4 GPa, resulting in fatigue lives between 10^2 and 10^{10} cycles. The structure's natural frequency was periodically monitored during the test as a measure of fatigue damage accumulation. The principal results of this experimental study are as follows:

1. Influence of temperature and relative humidity: in the HCF/VHCF regime ($N_f > 2\times10^6$ cycles), the environment, especially the relative humidity, strongly affected the fatigue properties. The fatigue lives were much shorter in harsh environments, and the detrimental effect was superior at 80ºC, 90%RH than at 80ºC, 30%RH. For instance, for a stress amplitude of ~2.4 GPa, the principal trend showed fatigue lives of ~6×10^9 cycles at 30°C, 50%RH, ~4×10^8 cycles at 80°C, 30%RH and ~9×10^7 cycles at 80°C, 90%RH. Similarly, increased damage accumulation rates were unambiguously observed at 80°C, 90%RH compared to 30°C, 50%RH (one to more than two orders of magnitude higher). However, the relative decrease rates in f_0 were only slightly higher in 80ºC, 30%RH air than in 30ºC, 50%RH air suggesting that the humidity

(affecting the adsorbed water layer thickness) has a more pronounced role than temperature in the fatigue degradation. In the LCF regime ($N_f < 2\times10^6$ cycles), the detrimental effect of the harsh environment, although present, was weaker. For instance, at ~2.6-2.7 GPa, relative decrease rates in f_0 were observed less than one order of magnitude higher in 80ºC, 90%RH air than in 30ºC, 50%RH air.

2. Influence of frequency: a strong influence of frequency is noticed, especially in the HCF/VHCF regime. Fatigue lives were much shorter at 4 kHz than at 40 kHz. At 2.5 GPa fatigue lives spanned from 9.7×10^4 to 9.8×10^6 cycles for "4-kHz" specimens. In contrast, fatigue lives ranging from 8.8×10^4 and 5.9×10^7 cycles were observed for a stress of amplitude as high as 3.0 GPa for "40-kHz" specimens. Damage accumulation rates were also observed to be ~one order of magnitude higher at lower frequency.
3. Influence of stress: a very large influence of stress on damage accumulation rates was observed. When dividing the stress by two, the resonant frequency decrease rates were lowered by 4 to 5 orders of magnitude. Lower stresses were also associated with larger decreases in f_0. Moreover the total damage accumulation was not significantly affected by either environment or frequency, which is consistent with the fact that a similar amount of fatigue damage accumulation is necessary to drive to failure.
4. Fracture surface analysis: fracture surfaces of relatively short-life specimens were also studied under scanning electron microscopy (SEM). This analysis revealed highly localized, smooth and semi-elliptical mirror-like regions.

To summarize, detrimental effects of harsh environment and lower frequency strongly suggest an environmental degradation mechanism in the HCF/VHCF range, such as the reaction-layer fatigue (RLF) mechanism. In contrast, the governing fatigue mechanism in the LCF regime is unclear. For the applied stresses investigated in this study, surface oxides must be at least 30-35nm thick to activate the RLF mechanism. Such required oxide thickening is unlikely to occur within the shorter lifetimes (<1min) involved in LCF. Instead, time-dependent subcritical cracking for the LCF regime (large stress intensity factors) was investigated based on a fracture mechanics analysis. The analysis suggests that, while the LCF experimental data may be accounted for with time-dependent subcritical cracking, static fatigue should also be observable for a large range of applied stresses.

5.2. *Directions for Future Work*

Even though the partial pressure of water is equivalent between 60°C, 75%RH and 80°C, 30%RH, the amount of adsorbed water is significantly lower in the second environmental condition, based on the last assumption. However the partial pressure of water is almost identical between these. Thus this fact can be used to separate the effect of temperature and relative humidity on the fatigue behavior. Further studies at 60°C, 75%RH would allow keeping the same partial pressure in water as 80°C, 30%RH and studying precisely the effect of increasing adsorbed water thickness on the fatigue behavior of SCSi thin films.

Furthermore, contradictory observations concerning subcritical crack growth in SCSi are reported in the literature. In this study, the subcritical crack growth simulation

could not match entirely the experimental data. If it is unlikely that this mechanism can account for the HCF/VHCF behavior, the underlying hypotheses in the simulation can strongly influence the LCF results. However, it stands that static fatigue could be observed over wide ranges of stress intensity. Such static tests could therefore support or rule out this fatigue mechanism.

Finally, although reaction-layer fatigue seems the most viable mechanism taking place in the HCF/VHCF range for SCSi thin films, physical explanations and direct observations of this process is required. Future works should therefore focus on observing oxide thickening and crack evolution at the nanometer scale, using for instance in-situ environmental TEM.

REFERENCES

1. Dugger, M.T., P.J. McWhorter, and A.D. Romig Jr, *Materials issues in microelectromechanical devices: Science, engineering, manufacturability and reliability.* Acta Materialia, 2003. **51**(19): p. 5837-5866.

2. Stauffer, J.-M. *Standard MEMS capacitive accelerometers for harsh environment*. 2006. Toulouse, France: American Society of Mechanical Engineers, New York, NY 10016-5990, United States.

3. Brown, T.G. *Harsh Military Environments and Microelectromechanical (MEMS) Devices*. 2003. Toronto, Ont., Canada: Institute of Electrical and Electronics Engineers Inc.

4. Kolari, K., A. Hokkanen, and I. Stuns. *Self-feeding microfluidic structures on silicon and glass*. 2005. Bellingham WA, WA 98227-0010, United States: International Society for Optical Engineering.

5. Cook, R.F., *Strength and sharp contact fracture of silicon.* Journal Of Materials Science, 2006. **41**(3): p. 841-872.

6. Allameh, S.M., *An introduction to mechanical-properties-related issues in MEMS structures.* Journal Of Materials Science, 2003. **38**(20): p. 4115-23.

7. Senturia, S.D. and V.T. Srikar, *The reliability of microelectromechanical systems (MEMS) in shock environments.* Journal of Microelectromechanical Systems, 2002. **11**(3): p. 206-214.

8. Alper, S.E., K. Azgin, and T. Akin, *A high-performance silicon-on-insulator MEMS gyroscope operating at atmospheric pressure.* Sensors and Actuators, A: Physical, 2007. **135**(1): p. 34-42.

9. Anon, *Smart Sensing Technology Revolutionizing the Appliance Industry.* Appliance, 2002. **59**(11): p. 38.

10. Minoshima, K., T. Terada, and K. Komai, *Influence of nanometre-sized notch and water on the fracture behaviour of single crystal silicon microelements.* Fatigue & Fracture of Engineering Materials & Structures, 2000. **23**(12): p. 1033-40.

11. Leipold, M.H. and C.P. Chen. *FRACTURE BEHAVIOR IN SILICON*. 1984. Dordrecht, Neth: D. Reidel Publ Co.

12. Ando, T., et al. *Effect of crystal orientation on fracture strength and fracture toughness of single crystal silicon*. 2004. Piscataway, United States: Institute of Electrical and Electronics Engineers Inc.

13. Yi, T. and C.-J. Kim, *Measurement of mechanical properties for MEMS materials.* Measurement Science and Technology, 1999. **10**(8): p. 706-716.

14. George, A., *Properties of Crystalline Silicon*. ROBERT HULL ed. Elastic constants and moduli of diamond cubic Si, ed. E.d.s.N. 20. July 1997: INSPEC publication.

15. Fitzgerald, A.M., et al., *Subcritical crack growth in single-crystal silicon using micromachined specimens.* Journal Of Materials Research, 2002. **17**(3): p. 683-692.

16. Fitzgerald, A.M., et al. *Fracture and sub-critical crack growth behavior of micromachined single crystal silicon structures*. 1998. Fairfield, NJ, USA: ASME.

17. Son, D.I., J.J. Kim, and D.I. Kwon, *Fracture behavior of single- and polycrystalline silicon films for MEMS applications.* Key Engineering Materials, 2005. **297-300 I**: p. 551-556.

18. Koyama, S., K. Takashima, and Y. Higo, *Fracture toughness measurement of a micro-sized single crystal silicon.* Key Engineering Materials, 2005. **297-300 I**: p. 292-295.

19. Ando, T., et al., *Fracture toughness measurement of thin-film silicon.* Fatigue and Fracture of Engineering Materials and Structures, 2005. **28**(8): p. 687-694.

20. Ritchie, R.O., *Mechanisms of fatigue-crack propagation in ductile and brittle solids.* International Journal Of Fracture, 1999. **100**(0376-9429).

21. Chen, T.J. and W.J. Knapp, *The fracture of single-crystal silicon under several liquid environments.* J. Am. Ceram. Soc. (USA), 1980. **63**(0002-7820).

22. Renuart, E.D., et al., *Fatigue crack growth in micro-machined single-crystal silicon.* Journal Of Materials Research, 2004. **19**(0884-2914).

23. Bhowmick, S., J.J. Melendez-Martinez, and B.R. Lawn, *Bulk silicon is susceptible to fatigue.* Appl. Phys. Lett. (USA), 2007. **91**(0003-6951).

24. Bhowmick, S., J.J. Melendez-Martinez, and B.R. Lawn, *Contact fatigue of silicon.* Journal of Materials Research, 2008. **23**(0884-2914).

25. Bhowmick, S., et al., *Fatigue and debris generation at indentation-induced cracks in silicon.* Acta Materialia, 2009. **57**(2): p. 582-589.

26. Zarudi, I., L.C. Zhang, and M.V. Swain, *Microstructure evolution in monocrystalline silicon in cyclic microindentations.* Journal of Materials Research, 2003. **18**(0884-2914).

27. Zarudi, I., L.C. Zhang, and M.V. Swain, *Cyclic microindentations on monocrystalline silicon in air and in water.* Proc. Inst. Mech. Eng. C, J. Mech. Eng. Sci. (UK), 2004. **218**(0954-4062).

28. Alsem, D.H., et al., *Mechanisms for fatigue of micron-scale silicon structural films.* Advanced Engineering Materials, 2007. **9**(1438-1656).

29. Kahn, H., R. Ballarini, and A.H. Heuer, *Dynamic fatigue of silicon.* Current Opinion In Solid State \& Materials Science, 2004. **8**(1359-0286).

30. Komai, K., K. Minoshima, and S. Inoue, *Fracture and fatigue behavior of single crystal silicon microelements and nanoscopic AFM damage evaluation.* Microsystem Technologies, 1998. **5**(1): p. 30-7.

31. Koskenvuori, M., et al., *Long-term stability of single-crystal silicon microresonators.* Sensors and Actuators A (Physical), 2004. **A115**(1): p. 23-7.

32. Muhlstein, C.L., S.B. Brown, and R.O. Ritchie, *High-cycle fatigue of single-crystal silicon thin films.* Journal of Microelectromechanical Systems, 2001. **10**(1057-7157).

33. Namazu, T. and Y. Isono. *High-cycle fatigue test of nanoscale Si and SiO2 wires based on AFM technique*. 2003: Institute of Electrical and Electronics Engineers Inc.

34. Pierron, O.N. and C.L. Muhlstein, *The critical role of environment in fatigue damage accumulation in deep-reactive ion-etched single-crystal silicon structural films.* Journal of Microelectromechanical Systems, 2006. **15**(1057-7157).

35. T. Namazu, S.I., *Characterization of single crystal silicon and electroplated nickel films by uniaxial tensile test with in situ X-ray diffraction measurement.* Fatigue & Fracture of Engineering Materials & Structures, 2007. **30**(1): p. 13-20.

36. Tabib-Azar, M., K. Wong, and K. Wen, *Aging phenomena in heavily doped (p+) micromachined silicon cantilever beams.* Sensors and Actuators A (Physical), 1992. **A33**(3): p. 199-206.

37. Van Arsdell, W.W. and S.B. Brown, *Subcritical crack growth in silicon MEMS.* Journal of Microelectromechanical Systems, 1999. **8**(1057-7157).

38. Burns, D.J. and H.F. Helbig, *A system for automatic electrical and optical characterization of microelectromechanical devices.* Journal of Microelectromechanical Systems 1999. **8**(4): p. 473-82.

39. Burns, D.J. and H.F. Helbig, *System for automatic electrical and optical characterization of microelectromechanical devices.* Journal of Microelectromechanical Systems, 1999. **8**(1057-7157).

40. Muhlstein, C.L., O.N. Pierron, and C.C. Abnet, *Methodology for low- and high-cycle fatigue characterization with kHz-frequency resonators.* Sensors and Actuators A (Physical) 2006. **128**(1): p. 140-50.

41. Namazu, T. and Y. Isono. *High-cycle fatigue damage evaluation for micro-nanoscale single crystal silicon under bending and tensile stressing*. 2004. Piscataway, United States: Institute of Electrical and Electronics Engineers Inc.

42. Sundararajan, S. and B. Bhushan, *Development of AFM-based techniques to measure mechanical properties of nanoscale structures.* Sensors and Actuators, A: Physical, 2002. **101**(3): p. 338-351.

43. Muhlstein, C.L., R.T. Howe, and R.O. Ritchie, *Fatigue of polycrystalline silicon for microelectromechanical system applications: crack growth and stability under resonant loading conditions.* Mechanics of Materials, 2004. **36**(0167-6636).

44. Pierron, O.N. and C.L. Muhlstein, *The critical role of environment in fatigue damage accumulation in deep-reactive ion-etched single-crystal silicon structural films.* Journal of Microelectromechanical Systems, 2006. **15**(1): p. 111-119.

45. Tsuchiya, T., *Reliability characterization of MEMS materials.* Transactions of the Institute of Electrical Engineers of Japan, Part E, 2005. **125-E**(7): p. 289-93.

46. Ando, T., M. Shikida, and K. Sato, *Tensile-mode fatigue testing of silicon films as structural materials for MEMS.* Sensors and Actuators, A: Physical, 2001. **93**(1): p. 70-75.

47. Buchaillot, L., *Feedback of MEMS reliability study on the design stage: a step toward Reliability Aided Design (RAD).* Microelectronics Reliability, 2003. **43**(0026-2714).

48. Millet, O., D. Collard, and L. Buchaillot, *Reliability of polysilicon microstructures: in situ test benches.* Microelectronics Reliability, 2002. **42**(0026-2714).

49. Connally, J.A. and S.B. Brown, *Slow crack growth in single-crystal silicon.* Science (USA), 1992. **256**(0036-8075).

50. Kahn, H., et al., *Fatigue failure in polysilicon not due to simple stress corrosion cracking.* SCIENCE, 2002. **298**(0036-8075).

51. Muhlstein, C.L., S.B. Brown, and R.O. Ritchie, *High-cycle fatigue and durability of polycrystalline silicon thin films in ambient air.* Sensors And Actuators A-Physical, 2001. **94**(0924-4247).

52. Espinosa, H.D., Y. Zhu, and N. Moldovan, *Design and operation of a MEMS-based material testing system for nanomechanical characterization.* Journal of Microelectromechanical Systems, 2007. **16**(5): p. 1219-1231.

53. Zhu, Y., A. Corigliano, and H.D. Espinosa, *A thermal actuator for nanoscale in situ microscopy testing: Design and characterization.* Journal of Micromechanics and Microengineering, 2006. **16**(2): p. 242-253.

54. Isono, Y. *Micro/nano materials testing for reliable design of MEMS/NEMS*. 2004. New York, NY 10016-5997, United States: Institute of Electrical and Electronics Engineers Inc.

55. Xiaodong, L. and B. Bhushan, *Fatigue studies of nanoscale structures for MEMS/NEMS applications using nanoindentation techniques.* Surface & Coatings Technology, 2003. **163-164**: p. 521-6.

56. Muhlstein, C.L., E.A. Stach, and R.O. Ritchie, *A reaction-layer mechanism for the delayed failure of micron-scale polycrystalline silicon structural films subjected to high-cycle fatigue loading.* Acta Materialia, 2002. **50**(1359-6454).

57. Bagdahn, J. and W.N. Sharpe, *Fatigue of polycrystalline silicon under long-term cyclic loading.* Sensors And Actuators A-Physical, 2003. **103**(0924-4247).

58. Muhlstein, C.L., E.A. Stach, and R.O. Ritchie, *Mechanism of fatigue in micron-scale films of polycrystalline silicon for microelectromechanical systems.* Applied Physics Letters, 2002. **80**(0003-6951).

59. Alsem, D.H., et al., *Very high-cycle fatigue failure in micron-scale polycrystalline silicon films: effects of environment and surface oxide thickness.* J. Appl. Phys. (USA), 2007. **101**(0021-8979).

60. Allameh, S.M., et al., *Surface topography evolution and fatigue fracture in polysilicon MEMS structures.* J. Microelectromech. Syst. (USA), 2003. **12**(1057-7157).

61. Shrotriya, P., S.M. Allameh, and W.O. Soboyejo, *On the evolution of surface morphology of polysilicon MEMS structures during fatigue.* Mechanics of Materials, 2004. **36**(1-2): p. 35-44.

62. Budnitzki, M., *Influence if the environment and alumina coatings on the fatigue degradation of polycristalline silicon films*. 2008, Georgia Institute of Technology.

63. Muhlstein, C.L., E.A. Stach, and R.O. Ritchie, *Mechanism of fatigue in micron-scale films of polycrystalline silicon for microelectromechanical systems.* Appl. Phys. Lett. (USA), 2002. **80**(0003-6951).

64. Pierron, O.N. and C.L. Muhlstein, *The role of debris-induced cantilever effects in cyclic fatigue of micron-scale silicon films.* Fatigue and Fracture of Engineering Materials and Structures, 2007. **30**(8756-758X).

65. Kahn, H., et al., *Mechanical fatigue of polysilicon: Effects of mean stress and stress amplitude.* Acta Mater. (UK), 2006. **54**(1359-6454).

66. Alsem, D.H., et al., *Further considerations on the high-cycle fatigue of micron-scale polycrystalline silicon.* Viewpoint set no. 44 "The materials for MEMS", 2008. **59**(9).

67. Belkada, R., et al. *Mechanisms of stress corrosion cracking in Si: A hybrid quantum-mechanical/molecular-dynamics simulation*. 2002: Materials Research Society.

68. Ciacchi, L.C., et al., *Stress-driven oxidation chemistry of wet silicon surfaces.* Journal of Physical Chemistry C, 2008. **112**(32): p. 12077-12080.

69. Ogata, S., et al., *Environmental effects of H2O on fracture initiation in silicon: A hybrid electronic-density-functional/molecular-dynamics study.* Journal of Applied Physics, 2004. **95**(10): p. 5316-5323.

70. Pierron, O.N. and C.L. Muhlstein, *The extended range of reaction-layer fatigue susceptibility of polycrystalline silicon thin films.* International Journal of Fracture, 2005. **135**(0376-9429).

71. Kahn, H., et al., *Anodic oxidation during MEMS processing of silicon and polysilicon: Native oxides can be thicker than you think.* Journal of Microelectromechanical Systems, 2005. **14**(1057-7157).

72. Kahn, H., et al., *Growth stresses and viscosity of thermal oxides on silicon and polysilicon.* Journal Of Materials Research, 2006. **21**(0884-2914).

73. Miller, D.C., et al., *Characteristics of a commercially available silicon-on-insulator MEMS material.* Sensors and Actuators, A: Physical, 2007. **138**(1): p. 130-144.

74. Li, G. and H. Hughes. *Review of viscous damping in micro-machined structures*. 2000. Santa Clara, CA, USA: Society of Photo-Optical Instrumentation Engineers, Bellingham, WA, USA.

75. Cho, Y.-H., A.P. Pisano, and R.T. Howe, *Viscous damping model laterally oscillating microstructures.* Journal of Microelectromechanical Systems 1994. **3**(2): p. 81-87.

76. Tsilingiris, P.T., *Thermophysical and transport properties of humid air at temperature range between 0 and 100°C.* Energy Conversion and Management 2008. **49**(5): p. 1098-110.

77. Wilke, C.R., *A viscosity equation for gas mixtures.* Journal of Chemical Physics 1950. **18**: p. 517-519.

78. Reid RC, P.J., Poling BE ed. *The properties of gases and liquids*. Chemical Engineering Series. 1988, McGraw Hill Int. Editions.

79. Brunauer, S., et al., *Theory of the van der Waals adsorption of gases.* Journal of the American Chemical Society, 1940. **62**: p. 1723-1732.

80. Brunauer, S., P.H. Emmett, and E. Teller, *Adsorption of gases in multimolecular layers.* Journal of the American Chemical Society, 1938. **60**: p. 309-319.

81. Picard, A. and H. Fang, *Methods to determine water vapour sorption on mass standards.* Metrologia, 2004. **41**(4): p. 333-339.

82. Asay, D.B. and S.H. Kim, *Evolution of the adsorbed water layer structure on silicon oxide at room temperature.* Journal of Physical Chemistry B, 2005. **109**(35): p. 16760-16763.

83. Muhlstein, C.L. and R.O. Ritchie, *High-cycle fatigue of micron-scale polycrystalline silicon films: fracture mechanics analyses of the role of the silica/silicon interface.* International Journal Of Fracture, 2003. **119**(0376-9429).

84. Pierron, O.N., D.D. MacDonald, and C.L. Muhlstein, *Galvanic effects in Si-based microelectromechanical systems: Thick oxide formation and its implications for fatigue reliability.* Applied Physics Letters, 2005. **86**(0003-6951).

85. Evans, A.G. and E.R. Fuller, *CRACK PROPAGATION IN CERAMIC MATERIALS UNDER CYCLIC LOADING CONDITIONS.* Metallurgical Transactions, 1974. **5**(1): p. 27-33.